Advanced analysis of complex seismic waveforms to characterize the subsurface Earth structure

Tianxia Jia

Submitted in partial fulfillment of the

requirements for the degree of

Doctor of Philosophy

in the Graduate School of Arts and Sciences

COLUMBIA UNIVERSITY

2011

ABSTRACT

Advanced analysis of complex seismic waveforms to characterize the subsurface Earth structure

Tianxia Jia

This thesis includes three major parts, (1) Body wave analysis of mantle structure under the Calabria slab, (2) Spatial Average Coherency (SPAC) analysis of microtremor to characterize the subsurface structure in urban areas, and (3) Surface wave dispersion inversion for shear wave velocity structure. Although these three projects apply different techniques and investigate different parts of the Earth, their aims are the same, which is to better understand and characterize the subsurface Earth structure by analyzing complex seismic waveforms that are recorded on the Earth surface.

My first project is body wave analysis of mantle structure under the Calabria slab. Its aim is to better understand the subduction structure of the Calabria slab by analyzing seismograms generated by natural earthquakes. The rollback and subduction of the Calabrian Arc beneath the southern Tyrrhenian Sea is a case study of slab morphology and slab-mantle interactions at short spatial scale. I analyzed the seismograms traversing the Calabrian slab and upper mantle wedge under the southern Tyrrhenian Sea through body wave dispersion, scattering and attenuation, which are recorded during the PASSCAL CAT/SCAN experiment. Compressional body waves exhibit dispersion correlating with slab paths, which is high-frequency components arrivals being delayed

relative to low-frequency components. Body wave scattering and attenuation are also spatially correlated with slab paths. I used this correlation to estimate the positions of slab boundaries, and further suggested that the observed spatial variation in near-slab attenuation could be ascribed to mantle flow patterns around the slab.

My second project is Spatial Average Coherency (SPAC) analysis of microtremors for subsurface structure characterization. Shear-wave velocity (Vs) information in soil and rock has been recognized as a critical parameter for site-specific ground motion prediction study, which is highly necessary for urban areas located in seismic active zones. SPAC analysis of microtremors provides an efficient way to estimate Vs structure. Compared with other Vs estimating methods, SPAC is noninvasive and does not require any active sources, and therefore, it is especially useful in big cities. I applied SPAC method in two urban areas. The first is the historic city, Charleston, South Carolina, where high levels of seismic hazard lead to great public concern. Accurate Vs information, therefore, is critical for seismic site classification and site response studies. The second SPAC study is in Manhattan, New York City, where depths of high velocity contrast and soil-to-bedrock are different along the island. The two experiments show that Vs structure could be estimated with good accuracy using SPAC method compared with borehole and other techniques. SPAC is proved to be an effective technique for Vs estimation in urban areas.

One important issue in seismology is the inversion of subsurface structures from surface recordings of seismograms. My third project focuses on solving this complex geophysical inverse problems, specifically, surface wave phase velocity dispersion curve inversion for shear wave velocity. In addition to standard linear inversion, I developed advanced

inversion techniques including joint inversion using borehole data as constrains, nonlinear inversion using Monte Carlo, and Simulated Annealing algorithms. One innovative way of solving the inverse problem is to make inference from the ensemble of all acceptable models. The statistical features of the ensemble provide a better way to characterize the Earth model.

TABLE OF CONTENTS

List of Figures

Acknowledgement

I would like to express my special thank to my major academic advisor, Dr. Arthur Lerner-Lam. Without his constant guidance, encouragement and supervision, as well as his financial support, I could not possiblely finish my five years of doctoral study or finish this thesis at Columbia University. Dr. Arthur Lerner-Lam brought me into the fascinating field of seismology. During my five years Ph.D. study under the supervision of Dr. Arthur Lerner-Lam, I have not only learnt thorough knowledge of seismology from him, but also learnt how to become a responsible scientist.

I also would like to thank my committee members, Dr. Won-Young Kim and Dr. Douglas Martinson for their insightful knowledge, helpful discussion and earnest guidance on my thesis. Dr. Won-Yung Kim provided enormous help for seismogram analysis and for SPAC experiments. Dr. Douglas Martinson's suggestion and advice on time series analysis, quantitative methods are extremely helpful for my thesis as well.

Also I would like to express my sincere appreciation for Dr. Steve Jaume at College of Charleston, for his kind support for the collection of microtremor data at Charleston in the spring of 2010 by providing seismometers and his help with the field experiment, as well as his kindness of providing data of Charleston. Without the great help from Dr. Steve Jaume, I could not finish the field experiment in Charleston so successfully.

I also want to thank Dr. William Stephenson and Dr. Stephen Hartzell from USGS for providing the dataset of microtremor study in Manhattan.

In addition, I would like to thank the professors and scientists from Seismology, Geology and Tectonophysics division of Lamont-Doherty Earth Observatory, Columbia

University. They are Dr. Spahr Webb, Dr. Göran Ekström, Dr. William Menke, Dr, James Gaherty, Dr. Geoff Abers, Dr. Meredith Nettles, Dr, Michael Steckler, Dr. Nano Seeber, Mr. Mitchell Gold, Mr. John Armbruster. They all offered great suggestion and help for my research during the past five years.

I appreciate the help of Ms. Mia Leo, Ms. Missy Pinckert, Ms. Dana Miller and Ms. Bonnie Bonkowski at Lamont-Doherty Earth Observatory on all kinds of logistics which make my life much easier at Lamont.

I also want to thank my good friends of former and current graduate student at Lamont-Doherty Earth Observatory. They are Jian Zhang, Ran Qin, Wei Du, Ge Jin, Yang Zha, Yvtian Wu, Byrdie Renik, Rafael Almeida, John Templeton, Pritwiraj Moulik, Ashley Shuler, Danielle Sumy etc..

I would also like to thank my best friends at Columbia University. They are Jie Xu, Chao Sun, Chunmei Qiu, Zheyuan Chen, Sai Zhang, etc. They make my five years life at Columbia happier than ever.

My special thank to my beloved fiancé, Danwei Wang for her love, encouragement and support along the way.

Most of all, I want to thank my deeply loved parents, Qiang Jia and Lixuan Zhang. Without their love and support throughout my life, I could not make it to where I am today. What I achieved today belongs to my family.

Chapter 1. Introduction

The main aim of my thesis is to use advanced analysis techniques to analyze complex seismic waveforms recorded at the Earth surface to better understand and characterize the subsurface Earth structure. To achieve this goal, I apply different techniques to investigate different parts of the Earth by analyzing various data sets. Through the whole thesis, I answered a couple of interesting and important questions, including (1) What does the subduction structure under the Calabrian Slab of the southern Tyrrhenian Sea in Italy look like? (2) What kind of subsurface information could be inferred from ambient noises, or mircotremors recorded in cities? (3) What is the shallow structure of shear wave velocity in Charleston, South Carolina? (4) How deep is the bedrock in lower Manhattan, New York City? The data which I am looking at vary from seismograms recorded from natural earthquakes in Italy to microtremors data obtained in Charleston, South Carolina. The investigating ranges go as deep as hundreds of kilometers in the upper mantle to tens of meters within the shallow crust. The goals of all these analysis are the same with what seismologists do everyday, which is to better investigate the Earth structure by analyzing complicated wiggles, seismic waveforms.

In Chapter 2, I analyzed the body wave signals generated by natural earthquakes recorded at stations in the Italian peninsula to study the complex mantle and subduction structure under the Calabria slab in the southern Tyrrhenian Sea. The subducted Calabria slab is believed to be the main reason causing active seismicity and volcanic activities in

southern Italian peninsula. A better understanding of the mantle and subduction structure is necessary in order to assess seismicity and associated seismic hazards in southern Italy. To understand the subduction slab structure, I studied and analyzed the body waves, particularly P-waves, that traverse the mantle under the Tyrrhenian Sea recorded at stations in the southern Italian peninsula. I used the dispersion analysis, scattering analysis, and attenuation analysis to investigate the Calabrian Slab effect on seismic signals. The study shows that the subducted slab affects the seismic waves in a consistent way. The low velocity subducted slab forms a waveguide, causing the body wave to disperse. The heterogeneous structures of the subducted lithosphere lead to the scattering of waves traveling within it. The cold subducting slab is the reason why the waves that travel within it are less attenuated than those that travel through hotter mantle above. The results from body wave analysis, specifically, the dispersion, scattering and attenuation analysis, show that seismic waveforms could be grouped by two populations based on the spatial pattern. I, therefore, separated ray-paths according to whether they go through the slab or not. The separated lines indicate the location of the slab boundary in 2-D geometry. In this way, the combined analysis provides great insight on the slab effect on seismic signals, as well as the location of the slab boundary. Furthermore, a better 3-D knowledge of the subduction structure under the southern Tyrrhenian Sea is obtained through body wave analysis.

Having researched on the mantle structure by analyzing the seismic signals generated by earthquakes, I switched my focus on studying the shallow Earth structure by looking at “noise”, or microtremors data in Chapter 3. It is known that local geology plays an

important role during strong earthquakes since the site-specific geological and soil conditions have a major impact on the ground motion. Shear wave velocity (Vs) is critical information used by seismologists and earthquake engineers to predict ground motion amplification and the site response to seismic waves. Various techniques have been developed to estimate Vs structure. They can be classified basing on different criterion. Some techniques, such as borehole methods, are invasive because drilling in the ground is required for measurement. Some methods, for example, SASW (Spectral Analysis of Surface Waves) and MASW (Multichannel Analysis of Surface Waves) require active sources to generate signals. In Chapter 3, I used Spatial Average Coherency (SPAC) method pioneered by Aki in the 1950s to estimate the Vs structure. SPAC stands out because it is easy to carry out and does not require active sources. SPAC, using microtremors as sources, is particularly suitable for Vs estimation in urban areas, such as the historic city of Charleston, South Carolina, and New York City Metropolitan area, for seismic hazard assessment. There are three basic assumptions of SPAC, (1) The microtremors (cultural noise) recorded in urban areas are mainly caused by human activity (people walking, cars, etc.) and propagate as high-frequency surface waves (>1Hz); (2) The 2D wavefield being recorded by an array of stations is stochastic and stationary ambient vibration, both in space and time; and (3) The vertical components of the microtremors mainly consist of fundamental-mode Rayleigh waves. I applied the SPAC method to estimate the Vs structure by inverting the Rayleigh wave phase velocity dispersion curve obtained from the coherency of the microtremors by the triangular array. The estimated Vs models in Charleston are interpreted along with Vs from previous borehole measurements and Refraction Microtremor methods. In Manhattan, the SPAC

method is used for estimation of bedrock depth. The experiments in Charleston and Manhattan show that the SPAC method of analyzing microtermors provides an attractive way to characterize shallow subsurface shear wave velocity in urban areas.

In Chapter 4, I developed advanced inversion techniques of shear wave velocity inversion from phase velocity dispersion curve, which is one critical step in the SPAC method to estimate shallow subsurface structure. I used iterative linear inversion, constrained inversion with borehole data, Monte Carlo and Simulated Annealing algorithm to solve the Vs inversion problem. Different techniques have their unique advantages and disadvantages compared with other methods. For example, Monte Carlo type random search algorithms do not depend on the starting model or require the computation of partial derivatives. Thus, they are particularly suitable for addressing the nonlinear problems. Yet the computation amount is usually too large with Monte Carlo and Simulated Annealing methods. Therefore, I proposed an innovative way of solving the inverse problem, by making inference from the ensemble of all acceptable models. The statistical characteristics of the ensemble provide a better way to characterize the model structure.

Chapter 2. Body Wave Analysis of Mantle Structure under the Calabrian Slab

2.1 Introduction

The Tyrrhenian Sea, a back-arc basin in the northwestern Mediterranean Sea, has a complex evolution history. It is believed that its present-day position in the Ionian Sea is a result of the rollback of the Calabrian Arc. Slab rollback has occurred to the southeast, but there is disagreement over the current slab morphology and the persistence of lateral tears or gaps between subducted Ionian lithosphere and slab remnants beneath the Southern Apennines just to the north. The positions of several volcanoes in the Aeolian Arc (Lipari and Vulcano Islands), Sicily (Mt. Etna) and the Southern Apennines (Mt. Vulture) are also anomalous (Figure 2.1). To assess seismicity and associated hazards around Calabria requires a better understanding of the structure of this plate-boundary region.

Travel time tomography is inadequate to image structure variations of length of 5 km or less, or at depth greater than 100 km, where subducting plate properties changes occur (Helffrich, 1989). To resolve these small-scale structures within the subducted plate, frequency dependence of wave propagation, i.e. wave dispersion, scattering, and attenuation are analyzed in this chapter.

Several studies have found significant body wave dispersion occurred within the subduction slab. Bokelmann and Maufroy (Bokelmann & Maufroy, 2007) studied

waveforms of P-wave that traverse the Alboran Sea region of the African-Iberian plate boundary in the vicinity of Gibraltar. The dispersion of body wave confirms anomalous upper mantle structures under the Alboran Sea. Abers and Sarker (Abers & Sarker, 1996) also observed the phase delays of high frequencies in body waves that travel in the Alaskan slab. They considered that such dispersion suggests a low-velocity wave guide that possibly reflects the subduction of oceanic crust in some way. Modeling studies by Abers (Abers, 2005) have shown that the observed dispersion is consistent with the presence of a low-velocity layer at the top of the slab. Iidaka and Mizour (Iidaka & Mizour, 1991) also observed such dispersion in Central Honshu in Japan, where waves traveling up along the slab show high frequencies delayed up to 1s relatively with the first long-period arrival. Abers (2005) also studied these waveform effects from the intermediate-depth earthquakes of seven circum-Pacific subduction zones, where travel time of body waves that travel parallel to the slab are dependent on frequency.

Therefore, we proposed that the Calabrian Arc subduction slab structure may be understood by studying and analyzing body waves, particularly P-waves, that traverse the mantle under the Tyrrhenian Sea. I used the dispersion analysis, scattering analysis, and attenuation analysis to investigate the Calabrian Slab's effect on seismic signals, and more importantly, to investigate the slab structure in fine scale.

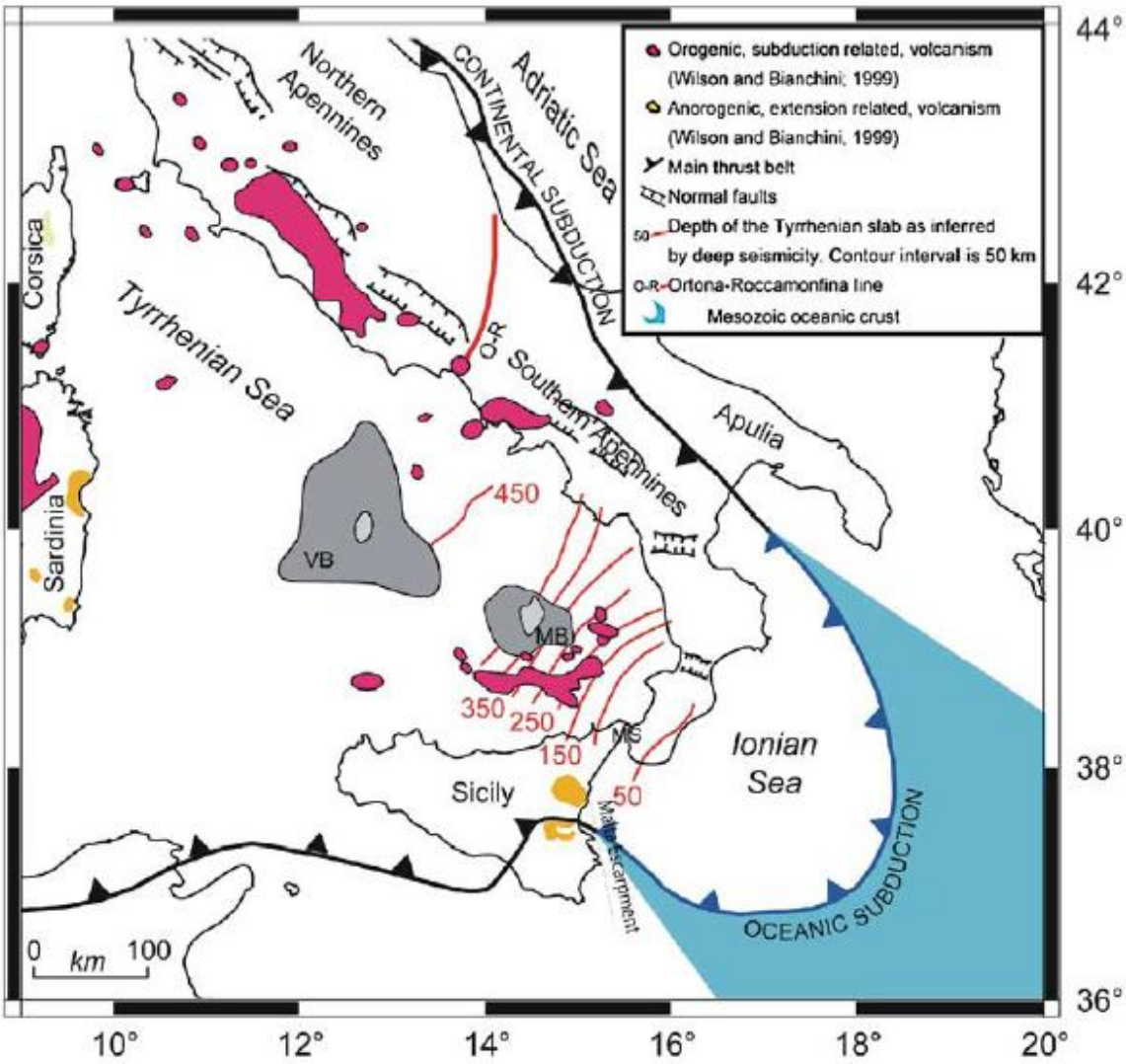

Figure 2.1: Tectonic map of the Calabrian Slab. (from Montuori et al. 2007).

2.2 Data

The data of this study are from CAT/SCAN (Calabrian-Apennine-Tyrrhenian / Subduction-Collision-Accretion Network) project, a joint experiment employed by researchers from Lamont-Doherty Earth Observatory of Columbia University (LDEO) and Italian institutions, of using seismic signals to study the Earth's crust and mantle beneath the Italian Peninsula. One of the major goals of this project is to determine the structure of the entire subduction/collision system, from the subducting plate across the trench to the volcanic arc, the subducting slab and the backarc spreading system. From December 2003 to April 2005, forty portable digital broadband seismic stations were set up throughout Southern Italy (Figure 2.2). I examined P waveforms for all earthquakes occurred in the southern Tyrrhenian Sea (Latitude N37-43, Longitude W13-16) with focal depth larger than 100 km and magnitude larger than 4, which were recorded by CAT/SCAN stations. Based on the criteria, between December 2003 and April 2005, seven earthquakes were selected.

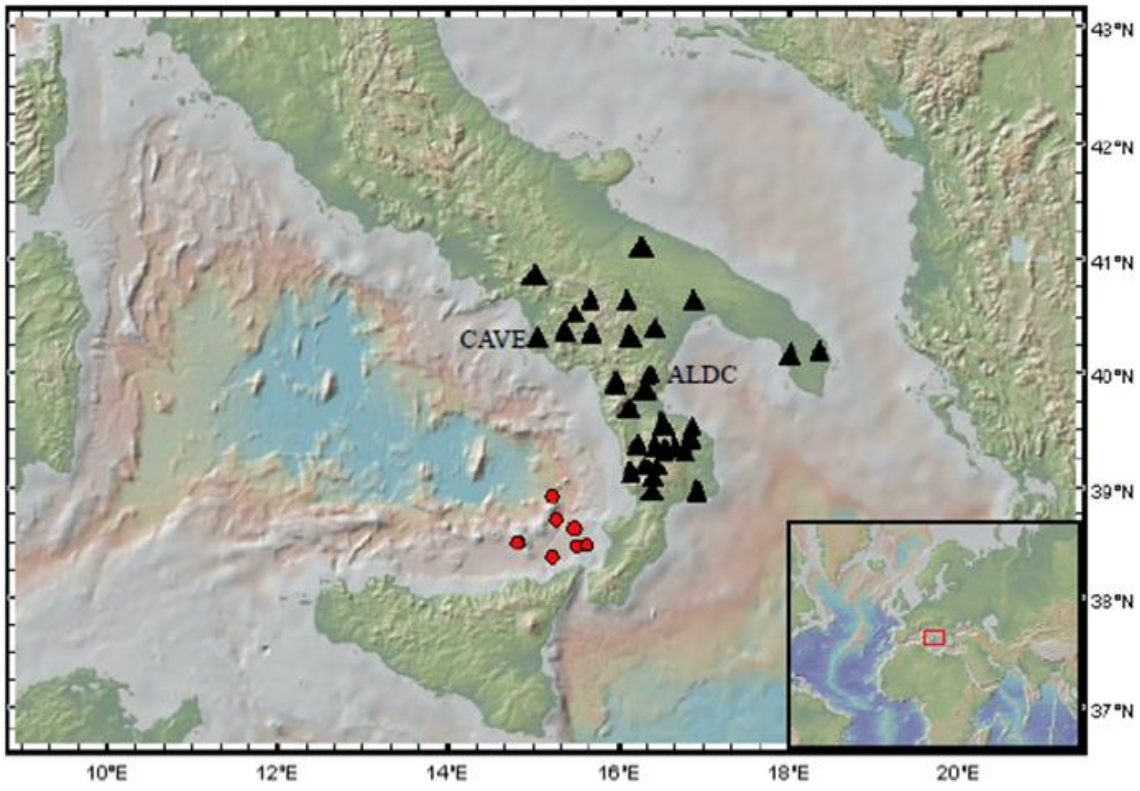

Figure 2.2: Map of Stations (black triangle) and Earthquakes (red circle)

2.3 Dispersion Analysis

I analyzed the seismograms to investigate the body wave, specifically the P-wave dispersion. Dispersion effects are evident with raw seismograms (Figure 2.3).

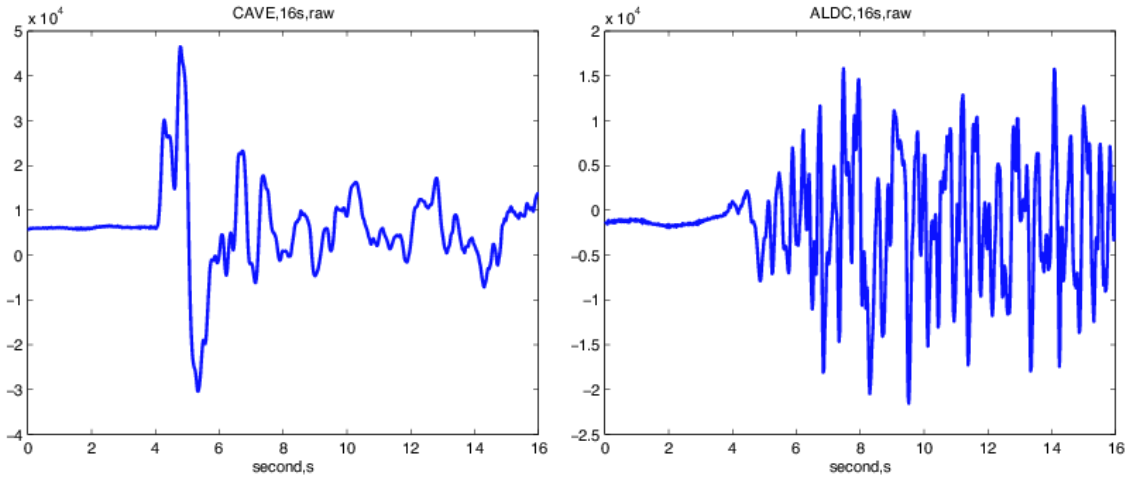

Figure 2.3: 16 seconds raw seismograms. Non-dispersion (CAVE) vs dispersion (ALDC)

In Figure 2.3, raw seismograms show that for the seismogram recorded in station CAVE, all frequency components seem to come in at the same time, while for the seismogram in ALDC station, high frequency components come later compared to low frequency parts. I measured the P wave dispersion by examining the dependence of group arrival time on frequency in a procedure similar to surface wave analysis (Dziewonski, et al. 1969). The procedure considers group arrival time as a set of band pass filtered wave packets, each around a given central frequency (Bokelmann 2007). I used the complex trace analysis to find the envelopes of filtered signals. The earliest arrival times of calculated envelopes are picked as the estimations of group arrival times.

The envelope of a given seismic signal is computed using complex trace analysis. Mathematically, given a real time signal x(t), the complex seismic trace, or analytical signal c(t) is given by (Taner et al. 1979),

$$c(t) = x(t) + iy(t).$$

Where i is the square root of -1, y(t) is the quadrature trace obtained by the Hilbert transform of the real trace x(t).

The analytical signal c(t) can be written as:

$$c(t) = a(t)e^{i\varphi(t)}.$$

And

$$x(t) = a(t)\cos(\varphi(t)).$$

$$y(t) = a(t)\sin(\varphi(t)).$$

Where $a(t)$ and $\varphi(t)$ are called instantaneous amplitude and instantaneous phase, respectively.

$a(t)$ and $\varphi(t)$ are given by

$$a(t) = [x(t) + y(t)]^{1/2}.$$

$$\varphi(t) = \arctan\left[\frac{y(t)}{x(t)}\right].$$

The envelope of the time signal x(t) is given by the instantaneous amplitude $a(t)$.

In my study, I chose the following six frequency bands as sequential band-pass filters, 0.5-1.5 Hz, 1.5-2.5 Hz, 2.5-3.5 Hz, 3.5-4.5 Hz, 4.5-5.5 Hz and 5.5-6.5 Hz, corresponding to central frequency of 1 Hz, 2 Hz, 3 Hz, 4 Hz, 5 Hz and 6Hz.

Dispersion analysis of two seismograms in Figure 2.3 is given in Figure 2.4 and Figure 2.5.

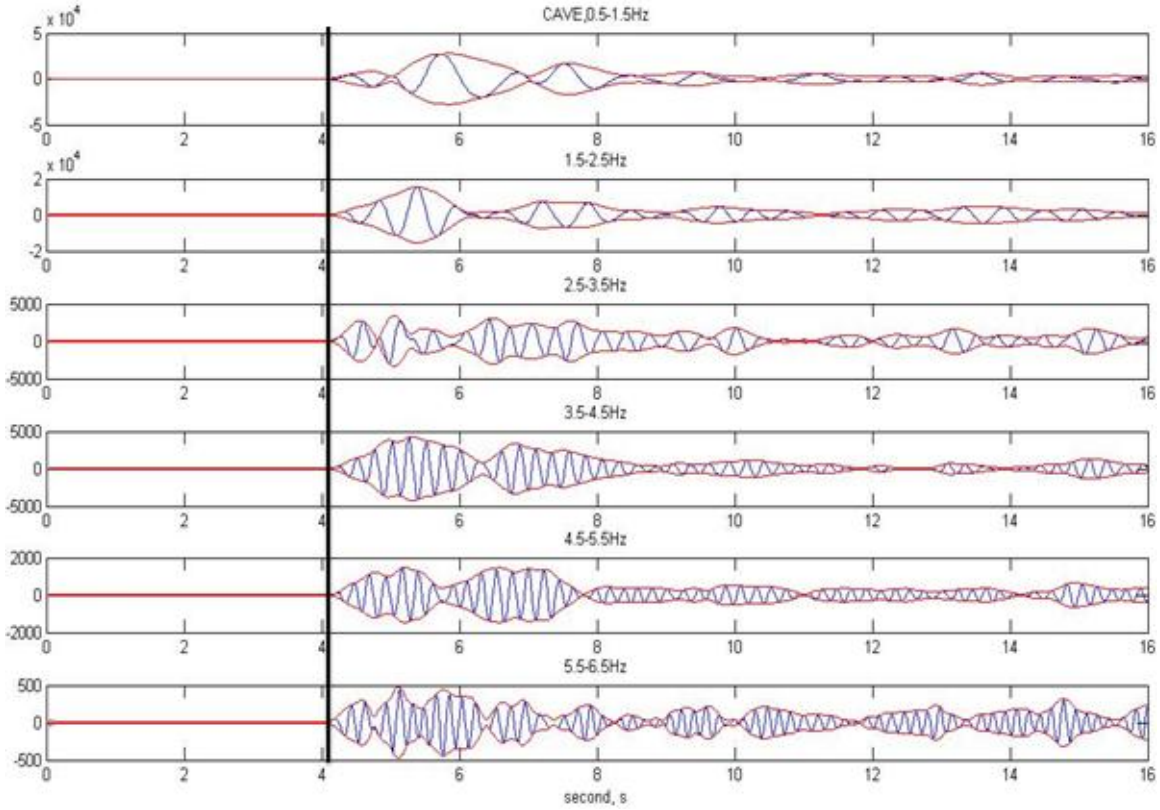

Figure 2.4: Example of dispersion analysis for seismic signal in CAVE. Raw signal is sequentially band-passed filtered to six frequency bands shown in blue lines in the six panels. The envelope of each filtered signal is computed using complex trace analysis plotted in red line in each panel. Dark black line indicates the first group arrival time for each frequency component.

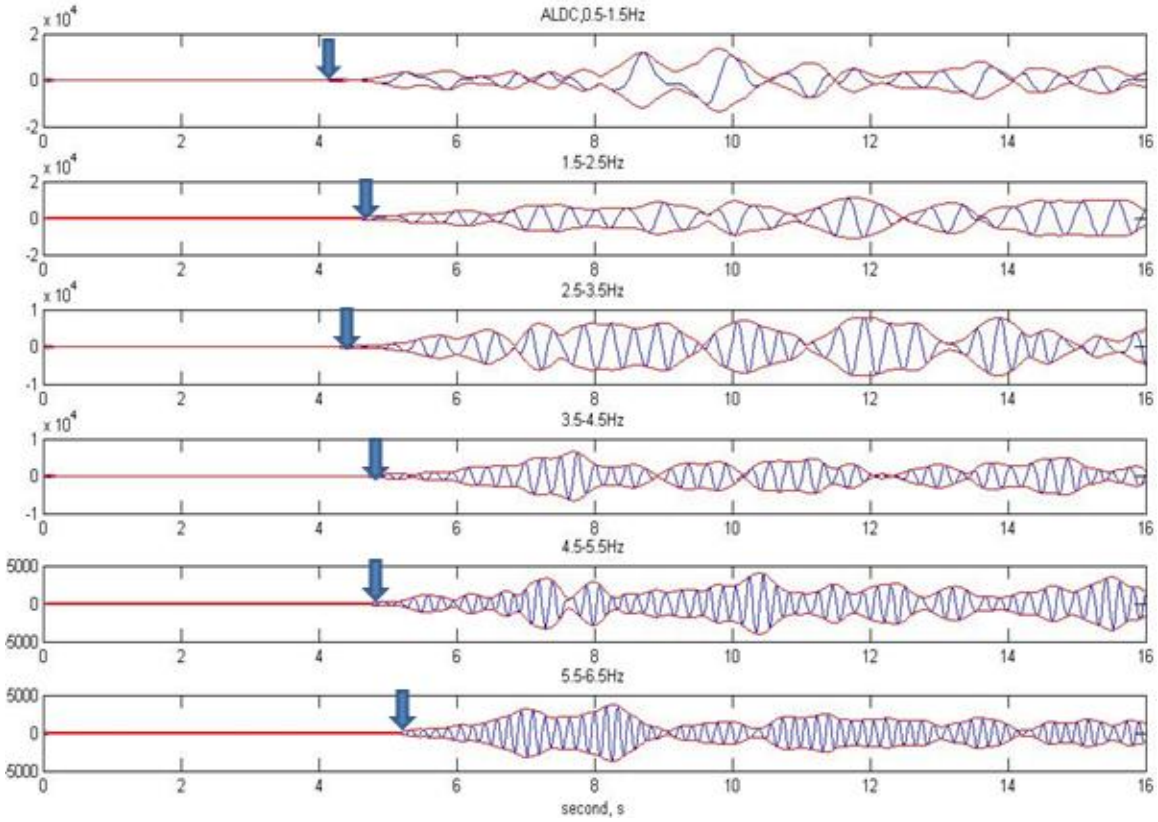

Figure 2.5: Example of dispersion analysis for seismic signal in ALDC. Raw signal is sequentially band-passed filtered to six frequency bands shown in blue lines in the six panels. The envelope of each filtered signal is computed using complex trace analysis plotted in red line in each panel. Dark blue arrows indicate the first group arrival time for each frequency component. .

Two distinctive patterns can be seen from this analysis. For certain signals (CAVE in Figure 2.4), group energies of all frequency bands come almost at the same time, i.e. no dispersion. While for other signals (ALDC in Figure 2.5), higher frequency signals (> 3Hz) arrive later than lower frequency signals (< 1Hz), i.e. the P wave is dispersive. I picked the first arrival of group energy and distinguish waveforms as “Dispersion” vs “Non-dispersion” according to the time interval between the arrival of high frequency and low frequency signals. If the group arrival time of high frequency (5-6 Hz) minus

low frequency (1-2 Hz) is larger than 0.5 seconds, I treated the signal as dispersion, otherwise as non-dispersion.

I plotted the ray paths on the 2D map based on whether they are dispersive or not in Figure 2.6.

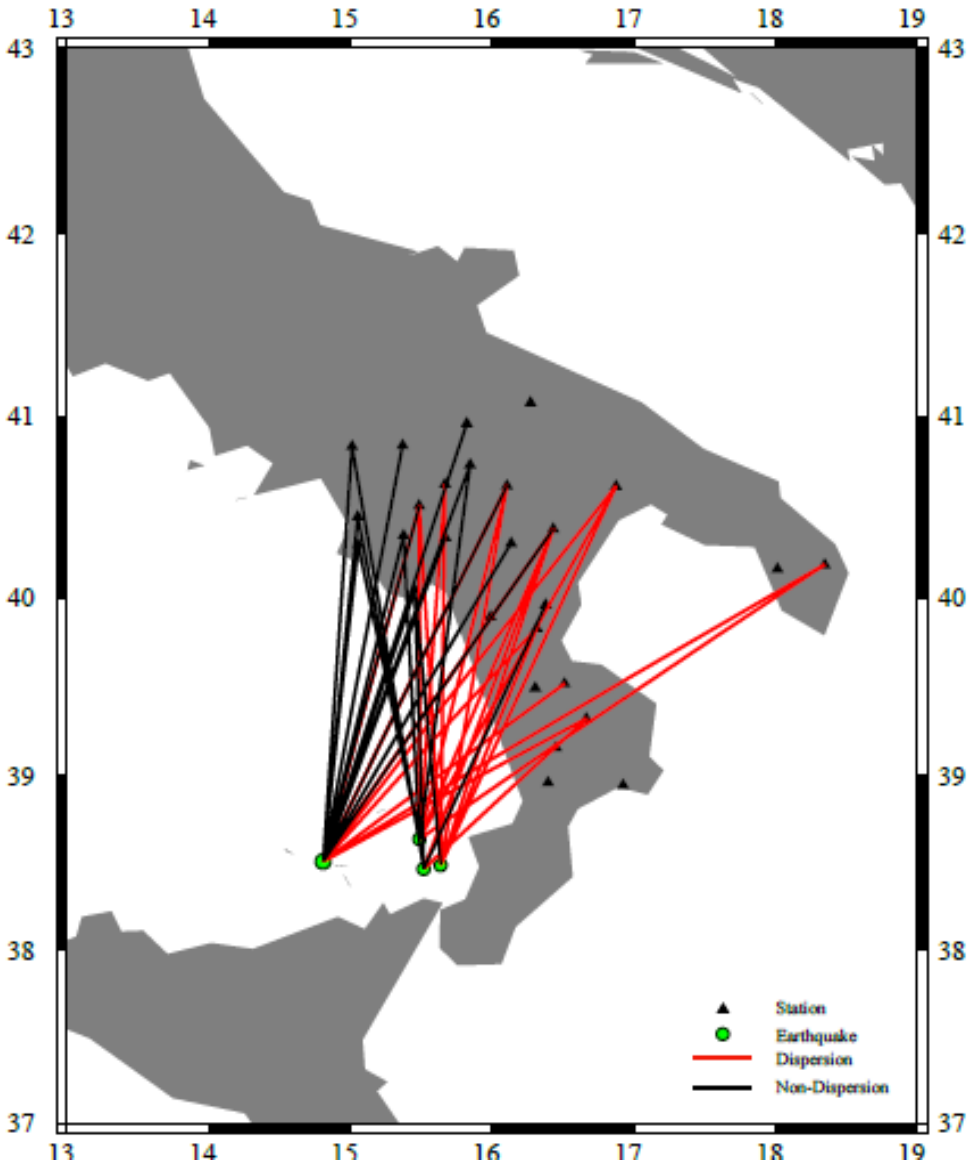

Figure 2.6: map of dispersion vs Non-dispersion. Red lines are ray paths that are dispersive, Black lines are ray paths that are not dispersive. Black triangles denote stations and green circles represent earthquakes.

Figure 2.6 shows that the ray-paths divide grossly into two spatial populations: dispersive and non-dispersive. The two populations are spatially separated that for one earthquake, seismic waves travel to southern stations are dispersive compared to waves travel to northern stations. This spatial separation correlates well with wave propagating either within the slab or within the mantle wedge.

2.4 Frequency-domain Analysis

2.4.1 Scatttering Analysis

I examined the energy distribution of seismic signals in frequency-domain using traditional Frequency-Time Analysis (FTAN) (Dziewonski et al. 1969). Each seismogram is transformed into frequency domain with Short-Time Fourier Transform (STFT) (Portnoff, 1980). The idea of STFT is to calculate the Fourier Transform for each time instant t. The Fourier Transform is applied to the signal multiplied by a time window. It can be considered as the result of passing the signal through a bank of band-pass filters with constant bandwidth, and then stacking individual band-pass filtered results together. The FTAN spectrogram is created by aligning each transformed signal as time on the horizontal axis, showing that the spectral density of the signal varies with time. Compared with traditional Fourier Transform, STFT has its advantage of representing signals as time evolution in spectral term. It provides information of both temporal and spectral simultaneously.

Two typical results of FTAN using STFT are shown in Figure 2.7 and Figure 2.8,

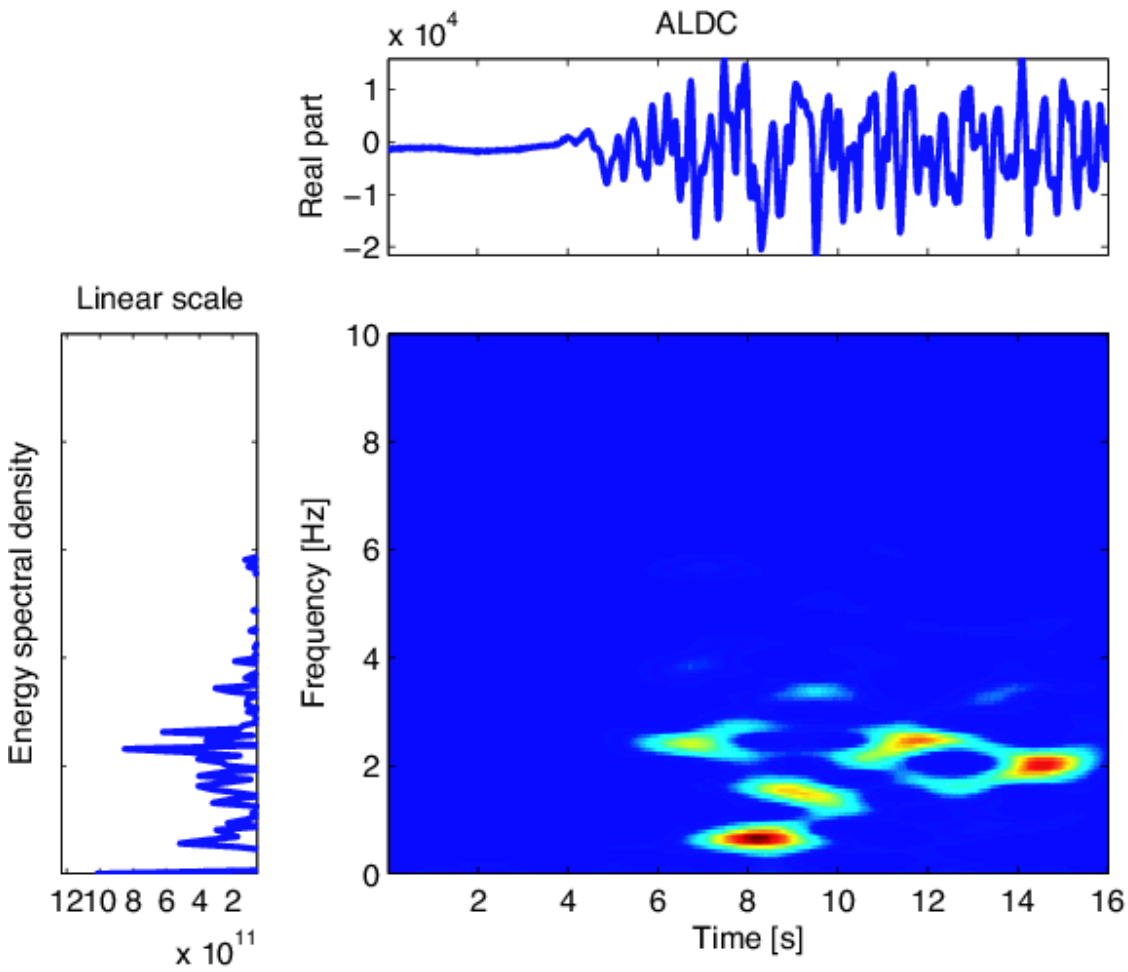

Figure 2.7: Example of scattering analysis for ALDC. Upper panel: 16 seconds raw seismic signal. Bottom left panel: power spectrum of the signal. Bottom right panel: FTAN spectrogram.

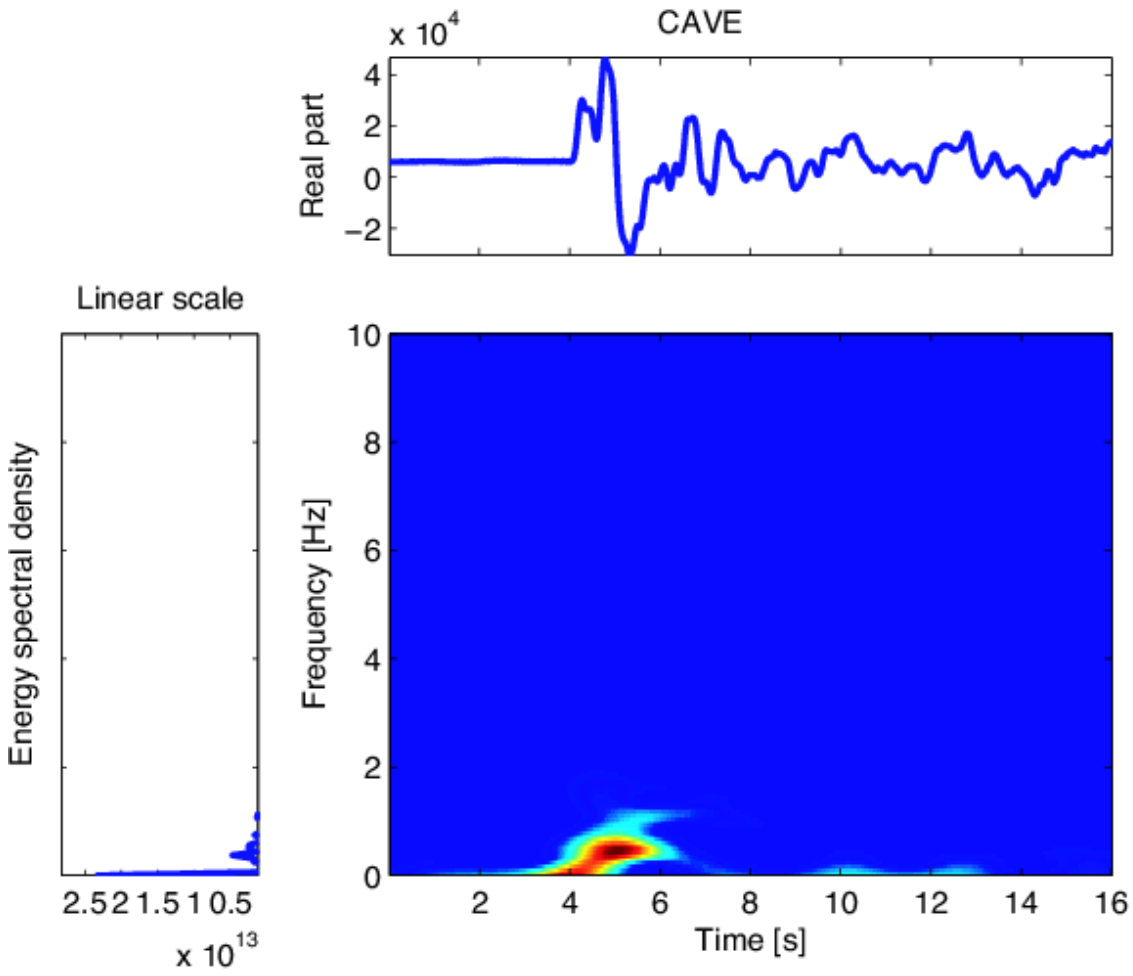

Figure 2.8: Example of scattering analysis for CAVE. Upper panel: 16 seconds raw seismic signal. Bottom left panel: power spectrum of the signal. Bottom right panel: FTAN spectrogram.

Similar to dispersion analysis, FTAN spectrograms also show two distinctive populations. Figure 2.7 (ALDC) is a typical spectrogram of one group, while Figure 2.8 (CAVE) is another group. For Figure 2.7 and 2.8, the upper panels are the raw seismograms, bottom left are the power spectrums, and bottom right are the FTAN spectrograms. The FTAN spectrogram of ALDC (Figure 2.7) shows that the frequency range of the signal spans from approximately 0Hz to 6Hz, and spans till 16 second in time domain, and the signal

is considered scattered. For CAVE (Figure 2.8), FTAN spectrogram shows that the frequency range spans only a narrow band (0-2 Hz), and less dominant in later time >8 sec, i.e. the energy is concentrated in a narrow time and frequency range. To quantify the scattering effects, I calculated the energy ratio as the total energy of 5-10Hz over total energy of 0-5Hz. Figure 2.9 is the plot of logarithm of the ratio against azimuth for the earthquake of Magnitude 5.5, depth 244km.

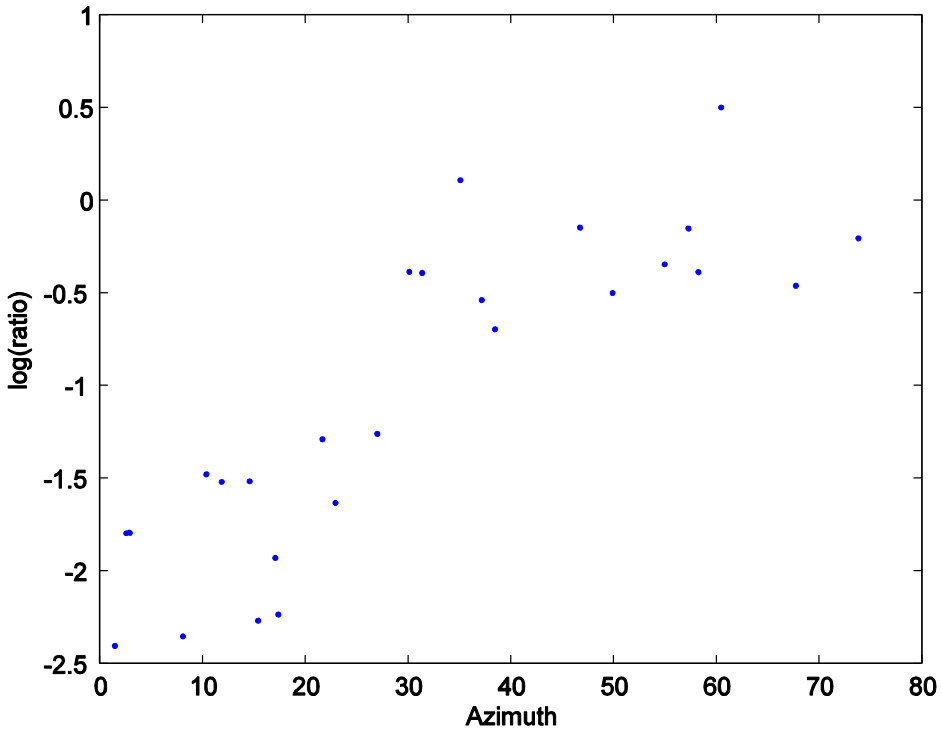

Figure 2.9: M=5.5 event spectral ratio vs azimuth.

The obvious trend found in Figure 2.9 is that the spectral ratio increases with azimuth. Figure 2.9 indicates stronger scattering for larger azimuth ray paths than smaller azimuth ray paths, because the larger spectral ratio represent stronger scattering.

I classifed the whole population into two classes using statistical discriminant analysis. Discriminant analysis, first proposed by Fisher (1936), is a statistical classification method used to discriminate data into groups. The analysis tries to maximize the ratio of the between-groups variance in the data over the within-group variance. It assumes that data from each group are sampled from multivariate normal distribution. The statistical formulation of discriminant analysis can be found from the original work by Fisher (1936) and most statistical pattern recognition books (Fukunaga 1990). The discriminant analysis has been successfully applied in seismology. Kim et al (Kim et al. 1993, 1997) used discriminant analysis to separate explosions from earthquakes based on spectral amplitude ratio. I applied the technique similar to the discriminate analysis utilized by Kim et al (1993, 1997) to classify the spectral ratio into two groups, strong scattering and weak scattering. In the two-group case, discriminant function analysis is analogous to multiple regression. If we denote the two groups in the analysis as 1 and 2, we can fit a linear equation of the type:

$$Group = a + b_1 x_1 + b_2 x_2 + \cdots + b_m x_m.$$

where a is a constant and b_1 through b_m are regression coefficients and x_1 to x_m are variables used to classify.

By selecting certain data as training set, in our cases, seismograms about which we are certain whether they are strong scattering or weak scattering, the analysis will separate the rest of the data into two groups by finding a discriminant function in linear form (equation above). Any new data could be classified into either one of the two classes by this function.

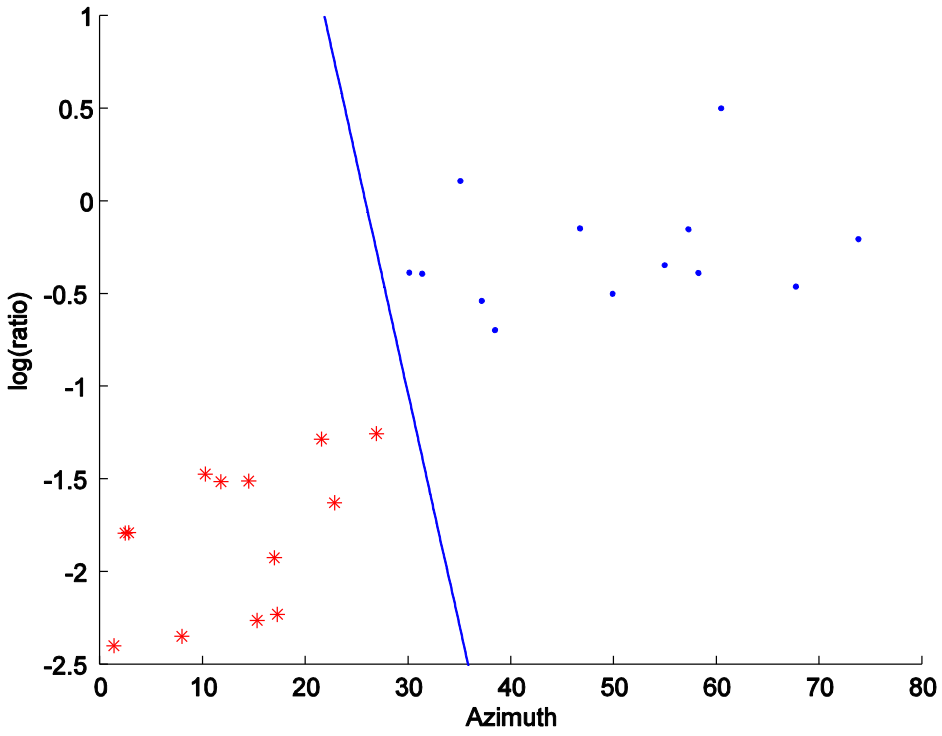

Figure 2.10: Discriminant analysis of the spectral ratio. Red star: statistical discriminant analysis result of one class, weak-scattering, Blue dot: statistical discriminant analysis result of the second class, strong-scattering. Blue line: discriminant function that separate two groups.

The line in the above figure representing the linear discriminating function obtained by discriminant analysis,

$$5387.4 - 2079.5x_1 - 8597.4x_2.$$

Where x_1 and x_2 are azimuth and log of the ratio respectively.

Using the above function, when the calculated value is larger than zero using a sample data [azimuth, log ratio], it is classified into the weak scattering group. The sample data falls into the strong scattering group if the calculated value is less than zero. The

classification boundary is around azimuth 30 degree. I calculated the spectral ratio of seismograms of all four earthquakes and plot it against azimuth (Figure 2.11).

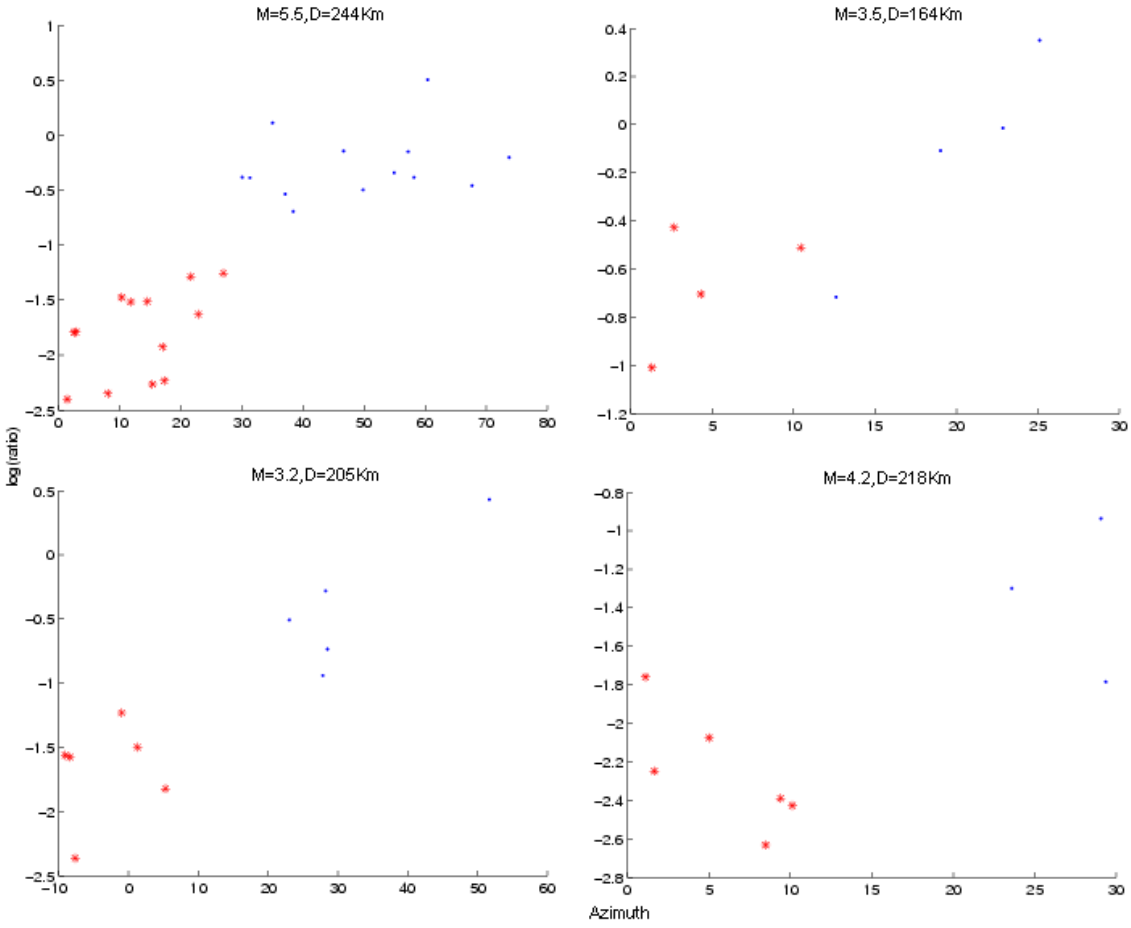

Figure 2.11: Spectral ratio of four events. M at the top of each panel indicates magnitude, and D indicates depth of each earthquake. Red star: statistical discriminant analysis results of one class, weak-scattering. Blue dot: statistical discriminant analysis results of second class, strong-scattering.

From figure 2.10 and 2.11, we found the spatial pattern emerged that, the small azimuth ray paths had lower ratio, i.e. weak scattering, while large azimuth paths had higher ratio, i.e. strong scattering. Based on the spectral ratios, statistical discriminant analysis

classifies the whole population into two classes. Data from all four earthquakes indicate the consistent classification boundaries that could separate the two classes are around azimuth 20-30 degree. Comparing with previous dispersion analysis, we confirm that two populations emerging from scattering analysis are consistent with the spatial separation of the dispersion analysis.

2.4.2 Attenuation

It has been known that anelastic processes causes attenuation of seismic wave, kinetic energy is lost by generating heat. When being attenuated, the amplitude of seismic waves is reduced and waveforms are modified due to high-frequency contents being absorbed. Attenuation is quantified by quality factor Q, which is the ratio between the energy stored and lost in each cycle due to inelasticity. Previous studies show that seismic waves attenuate more in hot materials than in cold materials. (Knopoff, 1964)

Body wave attenuation is characterized by t*,

$t^* = \frac{t}{\bar{Q}} = \int \frac{dt}{Q}.$

t* is estimated from log amplitude decay slope (Bowman, 1988):

$\bar{t^*} = -2\frac{d(\ln A)}{d\omega}$

The typical t* value for P wave is 1.

I calculated t* using above equations to characterize attenuation of seismic signals.

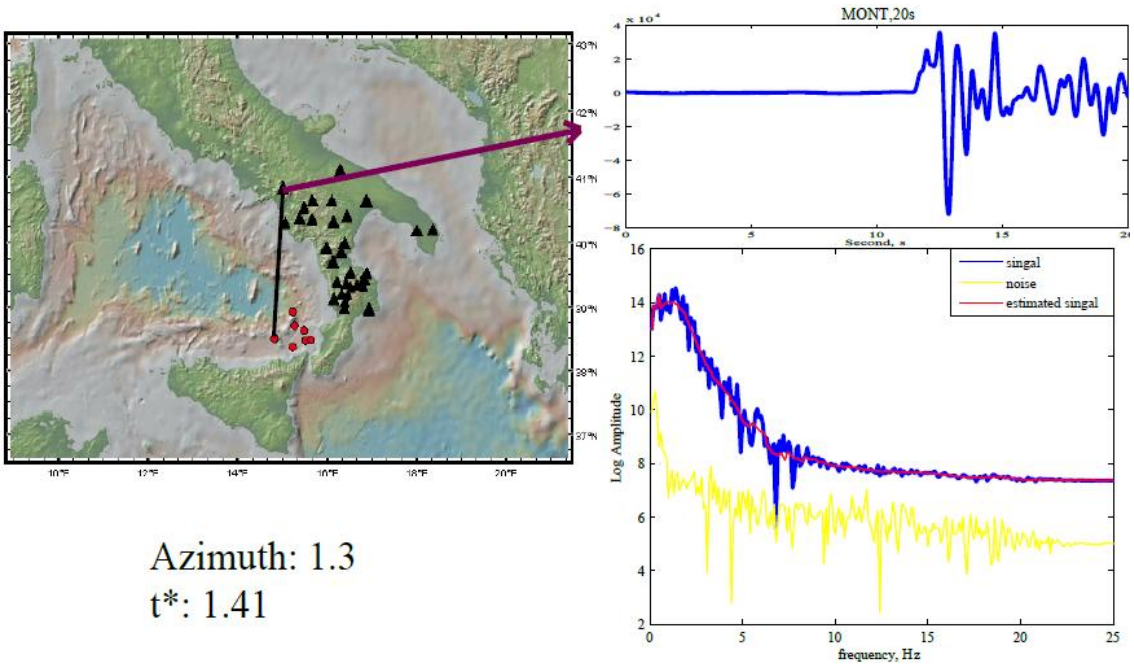

Figure 2.12: Example of Attenuation analysis. Left map show event-station path. Right upper panel: 20 second raw seismogram with pre-10 second noise and second half 10 second signal. Right bottom panel: spectrum of the second half 10 second signal (blue line), estimated spectrum of the signal (red line), and spectrum of first half 10 second noise (yellow line).

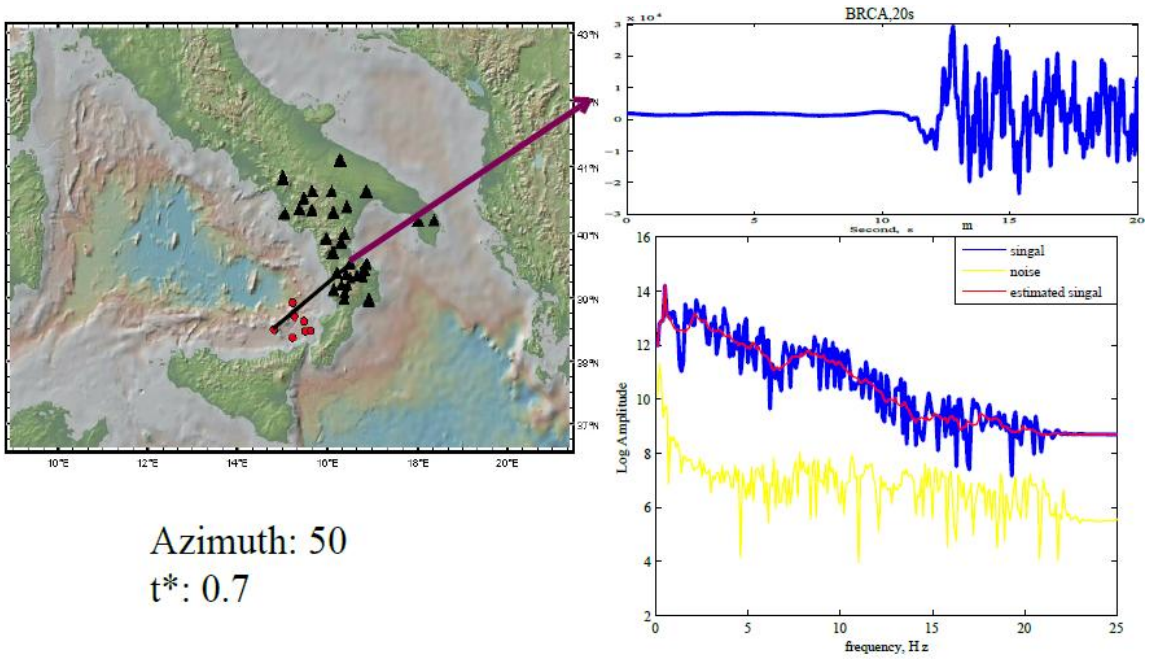

Figure 2.13: Example of Attenuation analysis. Left map show event-station path. Right upper panel: 20 second raw seismogram with pre-10 second noise and second half 10 second signal. Right bottom panel: spectrum of the second half 10 second signal (blue line), estimated spectrum of the signal (red line), and spectrum of first half 10 second noise (yellow line).

Figure 2.12 and 2.13 are examples of attenuation analysis. The left maps show event-station ray paths. Upper right panel is 20 second seismogram with pre-10 second noise and second half 10 second signal. Bottom right panel is logarithm of power spectrum. The blue line is the spectrum of the 10 second signal, the red line is estimated spectrum from moving average of the raw spectrum, and the yellow line is the spectrum of pre-10 second noise for comparison. Calculated t* and azimuth are given. We found that for the wave travel to north with azimuth 1.3 (Figure 2.12), the power spectrum of the signal decayed quickly, and gave a t* value of 1.41, indicating that the signal was strongly attenuated. Meanwhile, for the wave traveling to southern station with azimuth 50, the

power spectrum of the signal decayed relative slowly, and the t* value was 0.7, which implies weaker attenuation compared to the northern one.

I calculated all the t* for the M=5.5 earthquake and plot it against azimuth (Figure 2.14). I also used statistical discriminant analysis to classify the whole population into two classes.

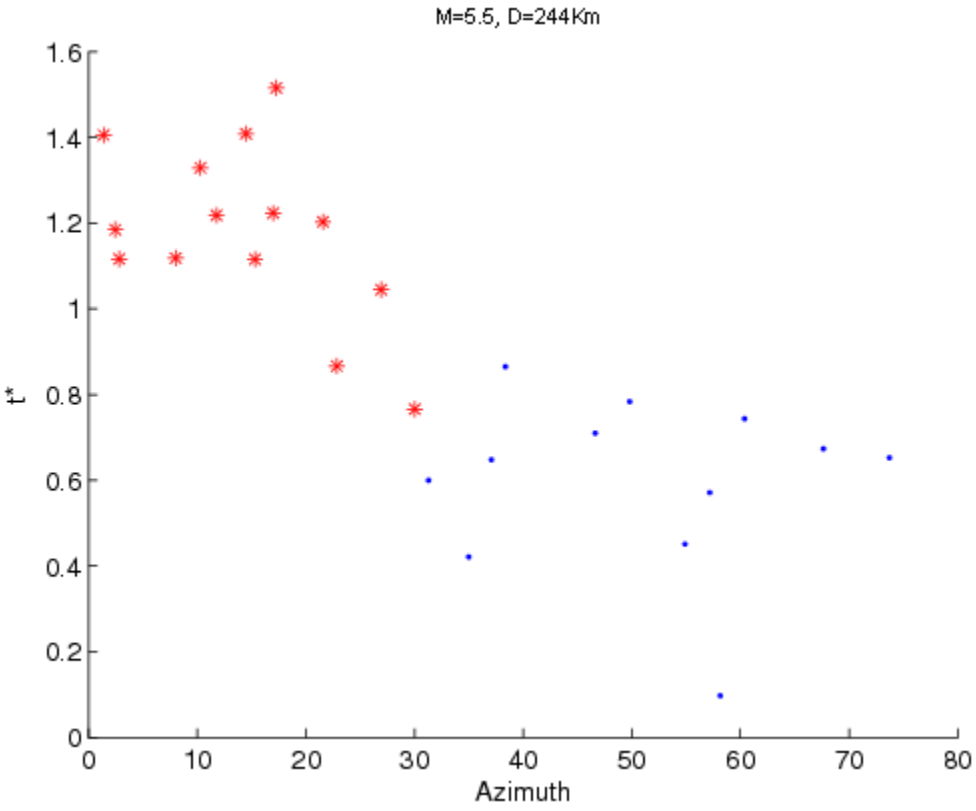

Figure 2.14: t* for M=5.5 event. Red star: statistical discriminant analysis results of one class, indicating strong-attenuation. Blue dot: statistical discriminant analysis results of second class, indicating weak-attenuation.

As shown in the figure 2.14, rays traveling to north (small azimuth) have larger t*, while rays traveling to south (large azimuth) have smaller t*. The statistical discriminant analysis results show that the separating boundary is around 30 degree between the two

classes. We conclude that rays traveling to the northern stations are more attenuated than rays traveling to the southern stations, because the larger t* indicate strong attenuation and vice versa. And the boundaries we found from attenuation analysis are consistent with the boundaries from scattering analysis.

Earlier works (O'Doherty & Anstey, 1971; Richards & Menke, 1983; Wu, 1985) have shown that seismic attenuation includes two parts, the intrinsic attenuation and the apparent attenuation. The intrinsic attenuation refers to the loss of energy by conversion to heat by internal friction, while the apparent attenuation refers to the redistribution of energy by scattering because of the heterogeneities in the Earth. While the physical mechanisms of these two types of attenuation are different, their effects on seismic signals are similar, causing amplitudes loss after traveling a certain distance. Menke and Dubendorff (1985) proposed an inversion method to discriminate the intrinsic attenuation and the apparent attenuation. When the apparent and intrinsic attenuation are additive, and the complete information on the total attenuation of both compressional and shear wave as a function of frequency is available, the intrinsic attenuation could be separated from the apparent attenuation by inverting the frequency spectra of normally incident compressional and shear waves. In our study, the key data that are necessary to perform the inversion, the measurements of total attenuation of both compressional and shear waves over a wide frequency bands, are not available. Thus, it is difficult for us to discriminate between what portion of the attenuation is caused by internal friction and what portion is due to scattering.

The quality factor Q is a measure of attenuation and Q is related to amplitude loss by,

$$A(x) = A_0 \exp\left(\frac{-\omega x}{2vQ}\right).$$

based on the constant Q model theory (Kjartansson, 1979). Where ω is the angular frequency, v is the velocity and A_0 is the initial amplitude and A(x) is the amplitude at distance x. Earlier I used t* value to characterize the attenuation, and t* is related to Q by,

$$t^* = \frac{t}{\bar{Q}} = \int \frac{dt}{Q}.$$

We, therefore, could apply inverse Q filter to compensate the attenuation by multiplying each frequency band by a factor of $\exp(-\frac{\omega}{2}t^*)$.

I applied the inverse Q filter to seismograms shown in section 2.4.1 (ALDC and CAVE). The attenuation compensated signals along with their FTAN spectrums are shown in Figure 2.15 and 2.16.

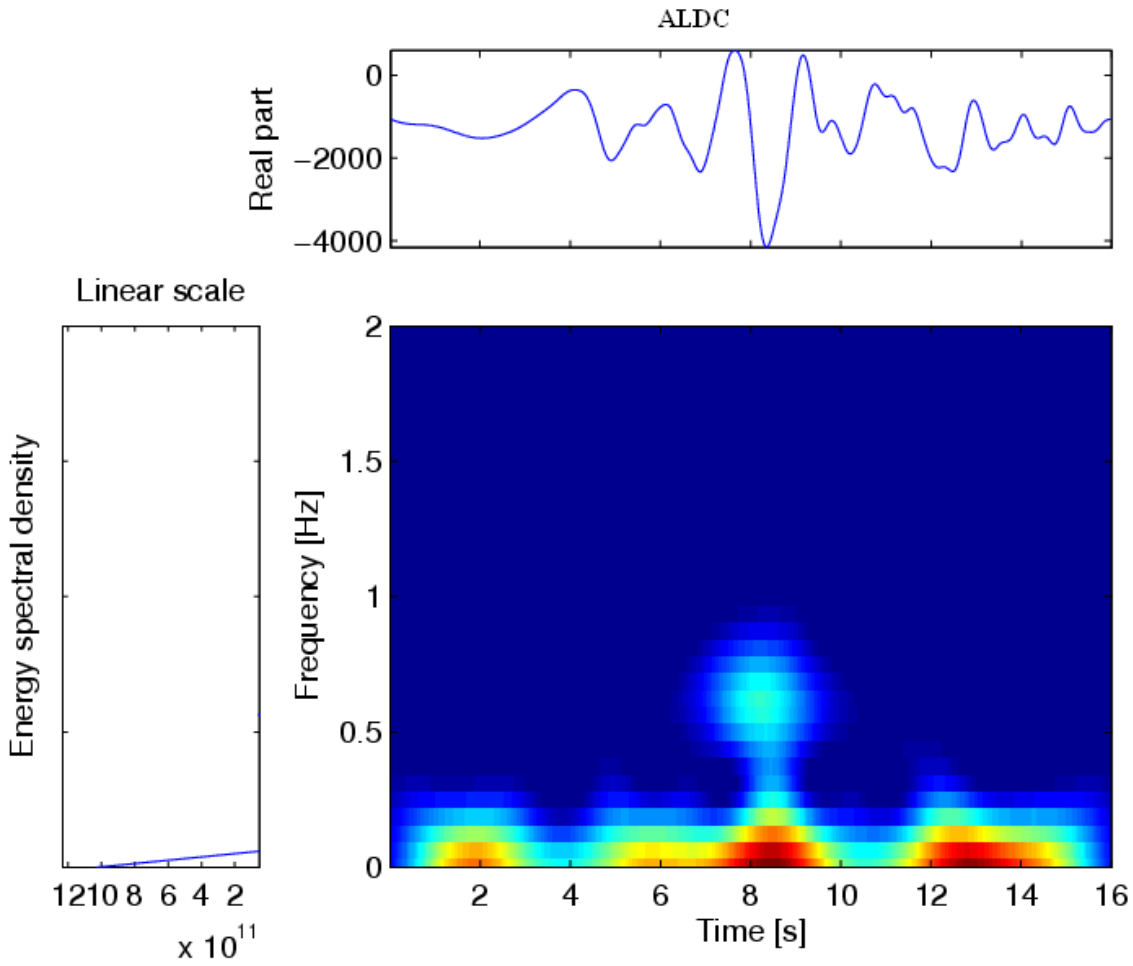

Figure 2.15: FTAN after applying inverse Q filter for ALDC. Upper panel: 16 seconds attenuation compensated seismic signal. Bottom left panel: power spectrum of the signal. Bottom right panel: FTAN spectrogram.

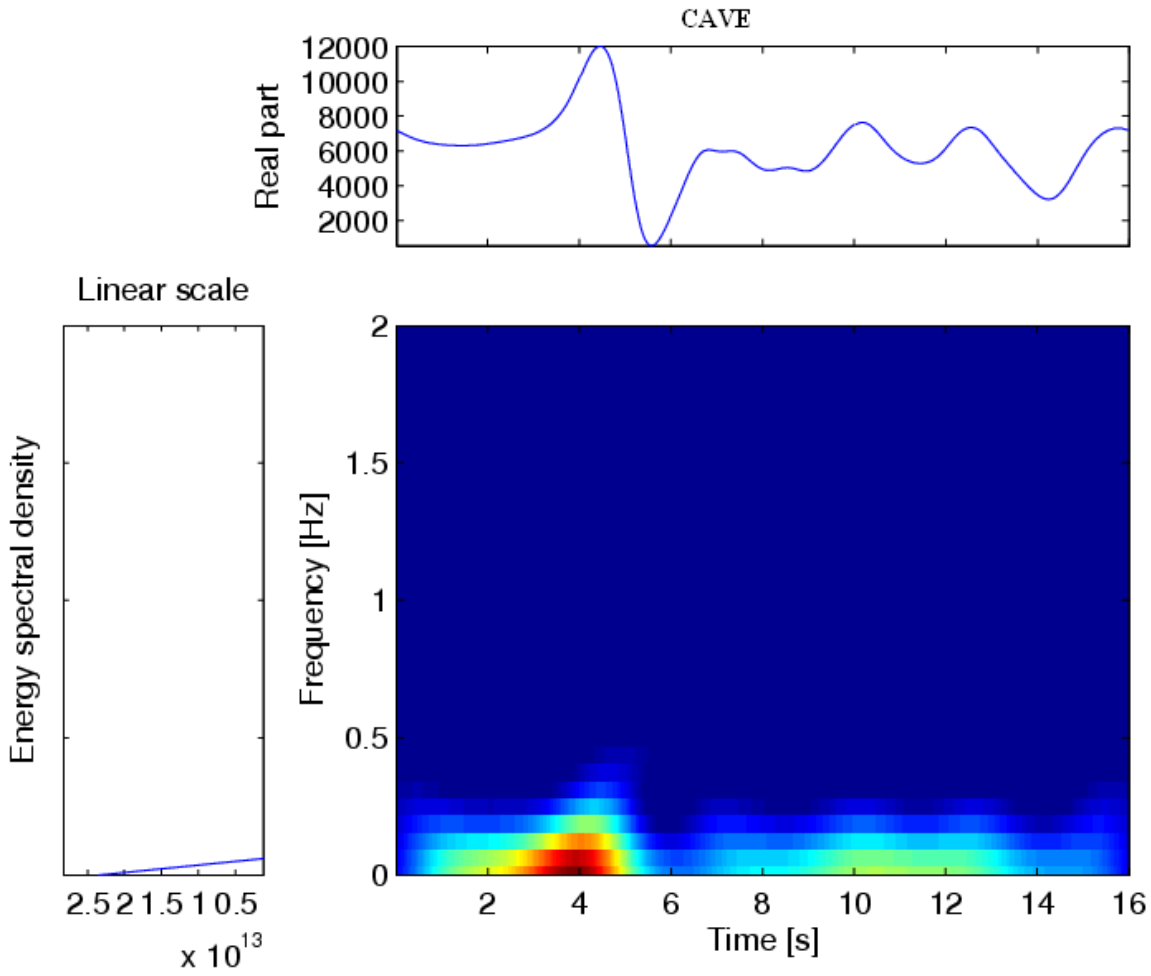

Figure 2.16: FTAN after applying inverse Q filter for CAVE. Upper panel: 16 seconds attenuation compensated seismic signal. Bottom left panel: power spectrum of the signal. Bottom right panel: FTAN spectrogram.

Compared with FTAN analysis in section 2.4.1, the attenuation compensated signals remove the effect of t* from the original signals, and the difference in FTAN spectrum (bottom right of Figure 2.7, 2.8, compared Figure 2.15 and 2.16) are, therefore, mainly due to attenuation. The remaining signals and their FTAN spectrum are intrinsic signals that are affected purely by scattering. For ALDC (Figure 2.7 and Figure 2.15), the P wave onset is clearly shown from inverse Q filtered signal at around 4th second. There are two relatively high energy parts, one being around 8 seconds, the other around 12th to 14th

second still exist in the filtered signals (Figure 2.15), which cannot be explained by inverse Q filter. I think these are caused by the scattering of the subducted slab that results in multiple arrivals after direct P wave arrival. For CAVE (Figure 2.8 and Figure 2.16), P wave energy is concentrated at around 4th seconds, as shown in both original spectrum and inverse Q filtered signals. Compared with ALDC, the inverse Q filtered signal of CAVE does not have too many high energy signals after direct P arrival, indicating that the wave traveling to CAVE does not have strong scattering as those seen in ALDC. This is consistent with our scattering analysis that waves go through the slab (i.e. ALDC) are scattered compared with waves go through the mantle (i.e. CAVE).

2.5 Discussion & Conclusion

The results from dispersion analysis and frequency-domain analysis consistently show that waveforms could be grouped by two populations according to the spatial pattern. Therefore, we believe that there must exist certain path-dependant propagation effects that produce these kinds of waveforms characteristics. Several possible explanations exist regarding the effects on waveforms. Crustal structure variation underneath each individual station could produce complexity of seismograms. Steckler et al. (Steckler et al. 2008) studied the teleseismic receiver functions from the same CAT/SCAN array in the Southern Apennines. Inferred P velocity profiles and correlation with crustal structures down to 40km do not show very significant differences between southern and northern stations. Thus, we came up with the assertion that it was unlikely that the crustal structures were so prominent to produce two consistent and distinctive patterns as

observed on the dispersion and scattering signals. Multiple phases, i.e. two phases with similar amplitude, might result in two arrivals, which look like what is observed in dispersion (Bokelmann 2007). But this could not explain signals scattering in frequency spectrum. Therefore, we were left with the proposition that subducting slab under the Tyrrhenian Sea led to the observed waveform characteristics.

Similar dispersions caused by subducted slab were also observed at other subduction zones (Bokelmann & Maufroy 2007; Abers & Sarker 1996). Several explanations have been proposed about the reason why subduction slab produce dispersed signals. A low velocity layer on top of the slab thus generate guided wave propagating along the slab is a reasonable explanation (Bokelmann & Maufroy 2007; Martin et al 2003). The low velocity layers are also found in Aleutian (Helffrich & Abers, 1997) and Chile-Peru subduction zone (Martin et al. 2003). Modeling studies by Abers (Abers 2005) and Martin (Martin et al. 2003) further confirm this argument. Most seismic tomography studies indicate the existence of subducting slab under the southern Tyrrhenian Sea. Neri (Neri 2009) and Chiarabba (Chiarabba 2008) both report a high velocity slab and a low velocity zone within the Tyrrhenian asthenosphere on top of the slab to the depth 100-150 km on their tomography model. Gvirtzman and Nur (Gvirtzman & Nur 1999) provided a 3-D sketch of the south Tyrrhenian subduction slab geometry. The heterogeneous structure of the subducted lithosphere could also cause scattering of wave travel within it, which explains why waves traveing to the southern stations are more scattering than those traveling to the north. Meanwhile, body wave attenuation is well observed in other subduction zone. Bowman (Bowman 1988) reported low attenuation in the subducting

Tonga slab relative to the surrounding mantle. He found that hot mantle materials above the slab are extremely attenuating for P-waves. Our observations of attenuation further confirm that cold subducting slab causes less attenuation for waves traveling within it than those traveling through hot mantle above. If it is indeed the subducting slab that cause the waveform complexity as observed in our dispersion, scattering and attenuation analysis, we could separate ray-paths according to whether they go through the slab or not. The separating line thus could indicate the location of slab boundary in 2-D geometry. The location of slab boundary we got is consistent with several previous geological and geophysical evidences. Carminati et al. (Carminati et al. 2005) investigated the seismicity and model the thermal state, and predicted the temperature and lateral anomaly of density distribution affected by the subducted slab under the Tyrrhenian Sea. Mattei et al. (Mattei et al. 2007) studied the palemagnetic, geologic and geodetic data to understand the tectonic evolution and formation of the Calabrian Arc. They found that the end of the Calabrian Arc bending during the Quaternary relating to the long-lived subduction of the Ionian slab, which caused the halting of the back-arc opening in the Southern Tyrrhenian Sea. Faccenna (Faccenna 2001) reconstructed the dynamic evolution of the Calabrian slab and experiment in lab to model the slab subduction process.

In summary, combined analysis of dispersion, scattering and attenuation allow us to get great insight in the slab effect on seismic signals in 2-D, as well as the location of the slab boundary. These analysis together provide a better 3-D knowledge of the subduction structure under the southern Tyrrhenian Sea.

Reference

1. Abers, G. A., and G. Sarker (1996), Dispersion of regional body waves at 100-150 km depth beneath Alaska: In situ constraints on metamorphism of subducted crust, *Geophys. Res. Lett*., **23**, 1171-1174.
2. Abers, G., (2005), Seismic log-velocity layer at the top of subduction slabs: observation, prediction, and systematics. *Phys Earth Plant. Inter*., **149**, 7-29.
3. Bokelmann, G., and E. Maufroy (2007), Mantle structure under Gibraltar constrained by dispersion of body waves, *Geophys. Res. Lett.*, **34**, L22305, doi: 10.1029/2007GL030964.
4. Bowman, J. R., (1988), Body wave attenuation in the Tonga subduction zone, *J. Geophys. Res.*, **93**, 2125-2139.
5. Carminati E., A.M. Negredo, J.L. Valera, C. Doglioni (2005). Subduction-related intermediate-depth and deep seismicity in Italy: insights from thermal and rheological modeling. *Phys Earth Plant. Inter*., **149**, 65-79
6. Chiarabba, C., P. De Gori, and F. Speranza (2008). The southern Tyrrhenian subduction zone: Deep geometry, magmatism and Plio- Pleistocene evolution. *Earth and Planetary Science Letters* **268**, 408–423;
7. Dziewonski, A., S. Block, and M. Landisman (1969), A technique for the analysis of transient seismic signals, *Bull. Seismol. Soc. Am.*, **59**, 427-444.
8. Faccenna, C., F. Funiciello, D. Giardini, , and P. Lucente (2001). Episodic back-arc extension during restricted mantle convection in the Central Mediterranean. *Earth and Planet. Sci. Lett.*, **187**,105-116.
9. Fisher, R. A. (1936). The use of multiple measurement in taxonomic problems, *Ann. Eugen*. **7**, 179-188
10. Fukunaga, K. Introduction to Statistical Pattern Recognition, Academic Press, San Diego, California, 1990.
11. Helffrich, G. R., S. Stein and B.J. Wood (1989), Subduction zone thermal structure and mineralogy and their relationship to seismic wave reflections and conversions at the slab/mantle interface, *J. Geophys. Res.*, **94**, 753-763.
12. Helffrich, G., G.A. Abers (1997). Slab low-velocity layer in the eastern Aleutian subduction zone. *Geophys. J. Int*. **130**, 640–648.
13. Iidaka, T., and M. Mizoue (1991), P-wave velocity structure inside the subducting Pacific plate beneath the Japan region, *Phys. Earth Planet. Int.*, **66**, 203-213.

14. Kim, W. Y., D. W. Simpson, and P. G. Richards (1993). Discrimination of regional earthquakes and explosions in eastern United States using high-frequency data, *Geophys. Res. Lett.*, **20**, 1507-1510.
15. Kim, W. Y., V. Aharonian, A. L. Lerner-Lam and P. G. Richards (1997). Discrimination of earthquakes and explosions in southern Russia using regional high-frequency three-component data from the IRIS/JSP Caucasus network, *Bull. Seismol. Soc. Am.*, **87**, 569-588
16. Kjartansson, E. (1979), Constant Q wave propagation and attenuation: *J. Geophys. Res.*, **84**, 4737-4748.
17. Knopoff, L. (1964) Q. *Rev. Geophysics*, **2,** 625–660.
18. Mattei, M., F. Cifelli, N. D'Agostino (2007), The evolution of the Calabrian Arc: Evidence from paleomagnetic and GPS observations. *Earth and Planet. Sci. Lett.*, **263**, 259-274.
19. Martin, S., A. Rietbrock, C. Haberland (2003). Guided waves propagating in subducted oceanic crust. *J. Geophys. Res.* **108**, doi: 10.1029/2003JB002450
20. Menke, W. and B. Dubendorff, (1985). Discriminating intrinsic and apparent attenuation in layered rock, *Geophys. Res. Lett.*, **12**,121-724.
21. Neri, G., B. Orecchio, C. Totaro, G. Falcone, and D. Presti (2009). Subduction beneath southern italy close the ending: results from seismic tomography, *Seismological Research Letters*, **80**, 63-70.
22. O'Doherty, R. F. and N. A. Anstey (1971). Reflections on amplitudes, *Geophys. Prospecting*, **19**, 430-458.
23. Portnoff, M.R (1980). Time-Frequency Representation of Digital Signals and Systems Based on Short Time Fourier Analysis. *IEEE Trans on ASSP*, **28**(1), 55-69.
24. Richards, P. G. and W. Menke, (1983). The apparent attenuation of a scattering medium, *Bull. Seismol. Soc. Am.*, **73**. 1005-1021
25. Steckler, M. S., N. Piana Agostinetti, C. K. Wilson, P. Roselli, L. Seeberg, A. Amato, and A. Lerner-Lam (2008), Crustal structure in the southern Apennines from teleseismic receiver functions, *Geology*, **36**, 155 – 158.
26. Taner, M. T., F. Koehler, and R. E. Sheriff (1979). Complex seismic trace analysis, *Geophysics*,**44**, 1041-1063
27. Wu, R. S. (1985). Attenuation of short period seismic waves due to scattering, *Geophys. Res. Lett.*, **9**, 9-12

Chapter 3. Shear-wave velocity structure characterization using Spatial Average-Coherency (SPAC) Analysis of microtremor

3.1 Introduction

[Overview]

It has been known by seismologists and earthquake engineers that local geology plays an important role during strong earthquakes. The intensity of ground motion is largely influenced by site-specific geological and soil condition. Site response of ground motion may vary in different areas according to subsurface geological structures and soil types. Therefore, the damage caused by an earthquake can vary significantly because of different site response (Seed & Schnable 1972). Soft, unconsolidated sediment materials could amplify ground motion during earthquakes and thus cause buildings on these grounds to become more vulnerable to earthquake damage than those built above the hard rocks. Many of the modern cities are built upon sediment rocks and therefore the damage caused by amplified ground motion of earthquakes is more devastating. The 1985 Mexico City earthquake (Seed et al 1988) and the 1989 Loma Prieta earthquake (Benuska 1990) are good examples of earthquakes causing severe damage to modern cities built on soft sediments. Both Mexico City and San Francisco-Oakland area are on deep clay deposits, and the ground motions during earthquakes were tremendously amplified and both cities were extensively destructed by the earthquakes. Therefore, an accurate estimation and

prediction of site-specific response of soil layers to earthquakes are highly necessary especially for cities in earthquake active areas.

Earthquakes could also cause soil liquefaction, a phenomenon of soil loses strength and stiffness in response to rapid applied stress during earthquake shaking, causing soil to behave like a liquid (Robertson & Fear 1995). The rapid and repeated shaking during large earthquakes cause water filled between originally saturated soil grains unable to flow out while pressure continues to accumulate. Eventually, the water pressure becomes greater than the stresses acting between the soil grains that keep them in contact with each other, thus cause soil to lose all of its strength and act like a flowing liquid. Earthquake liquefaction could cause severe damage to buildings built upon soils, which become liquefied during earthquake. Thus, better understanding of soil structure and its liquefaction potential would provide critical information for seismic risk assessment and earthquake risk mitigation studies.

Shear-wave velocity (Vs) is widely used in earthquake engineering and seismology community for seismic risk hazard investigation (Kramer 1996). Researchers have found that Shear-wave velocity information in soil and rock are critical parameters used for ground motion amplification and soil liquefaction predictions. For example, Vs is used for empirical prediction of strong ground motion (Boore et al 1997) and site coefficients for building codes (NEHRP 1997), for liquefaction potential characterization (Stokoe &

Nazarian 1985), for embankment stability analysis (Charlie et al 1985), and as input for numerical simulation of basin response (Graves, 1998).

[Vs30]

The average shear-wave velocity of the top 30m of the Earth, Vs30, which is computed by dividing 30m by the travel time from the surface to 30m, is an important parameter used in classifying sites in building codes (Dobry et al. 2000). For example, the National Earthquake Hazard Reduction Program (NEHRP) in the USA uses Vs30 as the index to classify the local site soil categories for the Uniform Building Code (UBC) (BSSC 2001). The site classes based on shallow shear-wave velocity, Vs30, are important in deriving strong-motion prediction equations (Boore et al., 1997), in construction of maps of NEHRP site classes (Wills et al. 2000, Table 3.1), and in applications of building codes to specific sites.

Site Class Definitions partially reproduced below

Site Class	Soil Profile Name	Average Properties in Top 100 feet (as per 2000 IBC section 1615.1.5) Soil Shear Wave Velocity, V_s	
		Feet/second	Meters/second
A	Hard Rock	$V_s > 5000$	$V_s > 1524$
B	Rock	$2500 < V_s \leq 5000$	$762 < V_s \leq 1524$
C	Very dense soil and soft rock	$1200 < V_s \leq 2500$	$366 < V_s \leq 762$
D	Stiff soil profile	$600 < V_s \leq 1200$	$183 < V_s \leq 366$
E	Soft soil profile	$V_s < 600$	$V_s < 183$

Table 3.1: NEHRP soil site classes, (http://www.nehrp.gov/)

As modern cities grow bigger and bigger, larger and larger population live in metropolitan areas nowadays. Highly-populated cities could face huge potential seismic risk in the event of strong earthquakes. Accurate assessment and evaluation of earthquake risk in cities has become necessary for earthquake damage mitigation purpose. Therefore, a rapid and accurate estimate of shallow shear-wave velocity could provide critical information needed for site-response evaluation, ground-motion prediction and site classes for earthquake hazard reduction purposes.

[Overview of existing method for Vs estimation]

Realizing the importance of Shear-wave velocity information for earthquake risk assessment, researchers have developed various methodologies to obtain Vs structure. They can be broadly classified into two categories. One is a direct measure of velocities

through logging from boreholes (invasive), and the other is an indirect seismic survey method (noninvasive). Boore (2006) has given a detailed review of each method.

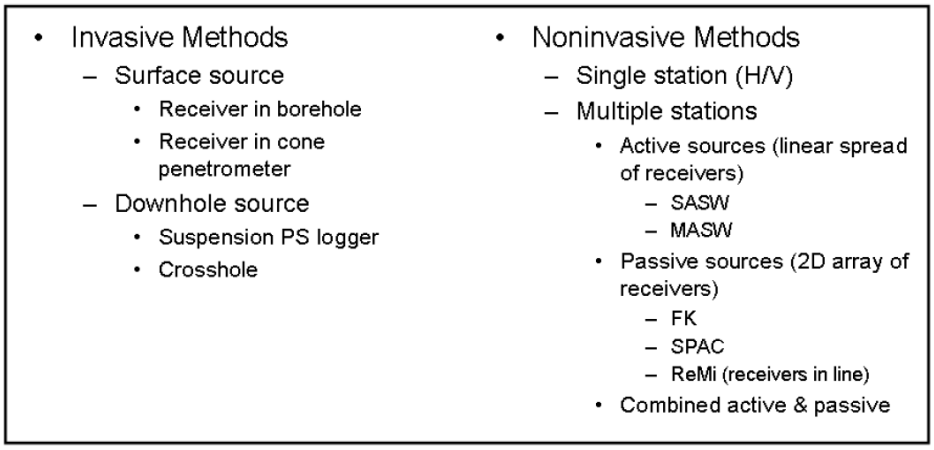

Figure 3.1: Summary of Vs estimation methods (Boore 2006)

[Borehole method]

Borehole logging technique is invasive. Seismic cone penetration test (SCPT) is a typical example of the borehole method. A deep hole is drilled in the ground to the depth of interest. A seismic cone penetration probe is lowered through the hole to the desired depth. Then a shear wave pulse is generated at the surface and recorded by the seismic transducer in the probe (Robertson et al. 1986). Shear wave velocities could then determined by simply dividing the differential travel times recorded at various probe depths by the difference of probe depth. An apparent drawback for borehole techniques is that they are invasive. It is sometime not possible to carry out in highly populated cities or historic sites when city protection needs to be considered. Also, the results from borehole are usually discrete data points, continuous estimates need to be done through interpolation or extrapolation. When there is abrupt jump or discontinuity of velocity

presented in the subsurface, the logging may not be able to accurately capture these irregularities.

[Non-invasive method & H/V]

Seismic survey, in contrast, is noninvasive in a sense that it does not require digging a hole in the ground. Shear-wave velocity could be indirectly estimated through different techniques. Noninvasive methods can be further subdivided into single station method and multiple stations (array) method. H/V ratio, the abbreviation of Horizontal-to-Vertical component spectral ratio, is the simplest single station analysis to infer subsurface structure information. H/V method is first proposed by Nogoshi and Igarashi (1971), and later popularized by Nakamura (1989). Bard (1998) gave a detailed review of the method, and it is now a widely used technique of qualitative or semi-quantitative assessment of sediment thickness over bedrock. Studies have found that the peak of H/V ratio is correlated with the fundamental resonance frequency of the site, thus provide an indicator of subsurface structure (Nogoshi and Igarashi, 1971; Nakamura 1989). Arai & Tokimatsu (2004) developed the method of the inversion for Vs from microtremor H/V spectrum. H/V ratio is particularly popular for earthquake microzonation studies where estimation of sediment type and thickness is necessary.

[Array technique]

All other noninvasive methods fall into multi-station array techniques. They all use the dispersive nature of surface wave, Rayleigh-wave in particular, to obtain shear-wave

velocity structure information. They differ from each other in terms of sources used, active vs passive source, and array configuration geometry, liner vs other 2-D geometry.

[Rayleigh wave dispersion]

Rayleigh-wave is one of the two types of surface wave, another being Love-wave, which is generated either by earthquakes or other sources of energy such as an explosion or sledgehammer impact, that travels along the Earth surface and is confined within very shallow depth below the surface. Resulting from the combination of P and SV motion, the particle motion of Rayleigh-wave is confined within the vertical plane (x-z plane, x being horizontal, z being vertical) normal to the travel direction of the wave (x direction). The most significant feature of Rayleigh wave is that Rayleigh wave become dispersive in medium where material elastic properties, specifically density and seismic velocity varies with depth. For Rayleigh wave traveling along the Earth's surface, typically waves of higher frequency travel slower than waves of lower frequency. This is because lower frequency wave has a relatively longer wavelength, and thus can penetrate deeper into the Earth than shorter wavelength wave. And because wave velocity generally increases with depth in the Earth, low frequency wave usually travel faster than high frequency wave, causing Rayleigh wave to become dispersive. The dispersive feature of Rayleigh wave could be characterized by dispersion curves, depicting different velocity of different frequencies, or different phases. Theoretical relationship has been built between 1-D vertical seismic velocity structure and dispersion curve (Aki & Richards 2002). Therefore, given Rayleigh-wave dispersion information, 1-D seismic velocity, particularly Shear-wave velocity could be inferred through mathematical operation called

inversion. If Rayleigh-wave dispersion data could be obtained, theoretically Shear-wave velocity could then be calculated. All multi-station array techniques of estimating shear wave velocity utilize the dispersive property of Rayleigh wave. Through different processing techniques, Rayleigh-wave dispersion curve can be estimated and shear wave velocity structure could then be inverted.

[SASW, MASW, f-k, beamforming, ReMi]

SASW (Spectral Analysis of Surface Waves) and MASW (Multichannel Analysis of Surface Waves) are two representative techniques of active sources linear array methods of estimating Vs. SASW method, first introduced by Nazarian in 1983 (Nazarian et al. 1983), consists of measuring surface wave phase velocity at numerous wavelengths, and using these measurements to calculate the dispersion curve for the site. It applies spectral analysis to ground roll (i.e. Rayleigh wave surface wave) generated by an impulsive source (sledgehammer) and recorded by a pair of receivers. The single pair of receivers is deployed and re-deployed based on calculated wavelength to sample the desired frequency range. Data are then analyzed in frequency domain to obtain the dispersion curve by calculating the phase difference between each receiver pairs. The SASW method has been used in many geotechnical engineering applications to acquire near-surface Vs information (Stokoe et al. 1994). Although it is easy to setup and needs only a pair of receivers, SASW require repeated re-configuration to sample multiple wavelengths to achieve acceptable picking of phase information, and thus become time and labor consuming for a given site. MASW method, developed by Part et al (1994), effectively overcomes the weaknesses of SASW method. For MASW method, a multi-

channel recording system, usually consists of 24 or 48 channel geophones, is used to record signal. An active source (sledgehammer) is used to generate signal. After a shot gather is collected, the time-distance record section (t-x) is transformed to frequency-slowness domain (f-p) through the wavefield transformation technique (McMechan and Yedlin 1981; Park et al. 1999). Dispersion curve could then be picked in f-p domain. The advantage of MASW over SASW is that only one experiment is needed to collect a shot gather data. Also unwanted noise could be reduced, and in f-p domain, not only fundamental mode, higher-mode dispersion curve can be picked in high frequency range, and the multi-mode dispersion curves could improve the inversion results effectively.

Both SASW and MASW are popular among geotechnical engineering and seismology community when shallow shear wave velocity information is needed. Although they differ in deployment and processing methods, they are fundamentally both active sources technique that an active source, like a sledge hammer is required to generate sources. This sometimes is not convenient to carry out, especially in highly populated cities. In contrast, passive sources experiments do not require controlled sources but use microtremors generated by either cultural (traffic, human activity) or natural (wind, ocean wave) phenomenon. Compared to active sources methods, passive sources techniques are rather quickly to deploy and will not be limited by the availability of sources, and thus become widely applied in estimation of shallow subsurface structure. Array methods of high-resolution beam-forming (HRBF) or frequency-wavenumber (f-k), pioneered by Lacoss et al. (1969) and Capon (1969), become popular recently. Researchers have successfully recovered useful information from ambient vibration or microtremor, which used to be considered as just noise. Liu et al (2000), Scherbaum et al. (2003), Wathelet et

al. (2004), Ohrnberger et al. (2004) and Kind et al (2005) applied HRBF/FK analysis on microtremor to obtain both phase velocity dispersion and shear wave velocity successfully both in large (Km) and small scale (m). HRBF/FK methods usually require stations to be deployed in 2-D geometry. Given one station in 2-D coordinate system (x,y) and recorded signal in time (t), the record section could be transformed to 2D wavenumber domain (kx,ky) and frequency domain (f). In wavenumber domain (kx,ky), for each frequency f, the weighted spectrum is the cross-power spectrum between all observation points of the array to each corresponding (kx,ky) point. The point with highest cross-spectral value for a given frequency is used to obtain the Rayleigh wave phase velocity. Possible sources locations could be inferred from the highest value in (kx,ky) domain. The method works well when the microtremor sources are unidirectional. But when the sources are located at various directions and come simultaneously, the velocity estimate might be incorrect.

The Refraction Microtremor (ReMi) method is a relatively new technique developed by Louie in 2001 (Louie 2001). It also uses passive microtremors as sources and uses linear configuration of the geophones. It applies tau-p transform (Thorson & Claerbout 1985) first to offset-time (x-t) shot gather, then frequency-slowness (f-p) transform of the tau-p section to f-p domain. Rayleigh wave could be separated in f-p domain and true phase velocity dispersion curve could be picked. One drawback of this method is that in low frequency range, it may require more subjective picking of dispersion than other techniques.

[SPAC overview]

The Spatial Auto-Correlation (SPAC) method was first introduced by Aki (1957, 1965), and generalized by Henstridge (1979), and become vastly used worldwide in Europe (Kudo et al 2002, Chouet et al 1998), Australia (Asten & Dhu 2004), and in US (Asten & Boore 2005). Researchers have been continuously improving the techniques based on Aki's original work (Tada et al 2007, 2009).

SPAC could be more accurately described by Spatial Average Coherence, reflecting its processing techniques, and still share the same acronym that Aki first used. The nature of SPAC method is that when records of ambient vibration are recorded from a constant distance pair of seismic stations along different azimuths, it is possible to compute the phase velocity of wave traveling across the array through azimuthally averaging station-pair correlation, or coherency, irrespective of the direction of the propagation. The SPAC method has inherent advantage that it extracts scalar wavespeed of propagating seismic energy across the array irrespective of the direction and number of sources. The insensitivity to source azimuth has great advantages when sources of microtremor are unknown in advance. In comparison, the beamforming or FK method require sources to be unidirectional. The quality of the result may decrease significantly when multiple sources are presented. It has been reported that when both f-k and SPAC method are applied to same data sets, SPAC tend to produce higher resolution results compared to f-k method. (Asten 2001, Okada 2003, Hartzell 2005)

Compared with other techniques, SPAC possesses the advantages of requiring neither drilling nor active sources. Using microtremors coming from any direction and from any distance, and only a few seismometers, SPAC could be carried out quickly and conveniently. The deployment can be adapted to nearly any space available, including city streets, empty lots, parks, and around the support pillars of infrastructure, such as bridges and elevated roadways.

Because of all the advantage SPAC has over other techniques, I chose SPAC method to estimate Vs structure. In section 3.2, I gave the detailed theoretical derivation of SPAC method, the procedure of obtaining Vs from microtremors, and test the method synthetically. In section 3.3, I discussed one important step in SPAC, which was the inversion of Vs from dispersion curve. In section 3.4, I applied the SPAC method to Charleston, South Carolina to test the method and compare the results with other techniques. In section 3.5, I applied the SPAC method to Manhattan, New York City to infer the subsurface Vs structures.

3.2 SPAC Methodology.

[Theoretical derivation]

Aki (1957) first proposed to use ambient vibration to determine phase velocity by what he called SPAC (Spatial Auto-Correlation) method. Aki thoroughly derived the theory in his original paper. Further improvements as well as practical examples were given later (Aki 1965). The essence of SPAC method is that when ambient vibrations are recorded

from a constant distance pair of seismic stations along different azimuths, the phase velocity of wave traveling across the array can be estimated by azimuthally averaging station-pair correlation, or coherency, irrespective of the direction of the propagation. The basic assumption Aki made is that the recorded 2D wavefield by the array is stochastic and stationary ambient vibrations, both in space and in time.

Let us assume that the stochastically stationary wavefield is formed by superposition of many plane waves propagating in any direction in the horizontal plane, with traveling speed c. The ground motion recorded at two locations (x, y) and $(x + \zeta, y + \eta)$ are written as $u(x, y, t)$ and $u(x + \zeta, y + \eta, t)$ respectively. The spatial autocorrelation function is defined as:

$$\phi(\xi, \eta, t) = \overline{u(x, y, t)u(x + \xi, y + \eta, t)}, \quad (3.2.1)$$

where the bar indicate time average. Under the assumption that the wavefield is stationary, the spatial autocorrelation only depends on the displacement (ζ, η) between two locations. Aki show that the azimuthal average of the spatial autocorrelation function (Aki 1957, equation 37) can be written as:

$$\overline{\phi(r)} = \frac{1}{2\pi} \int \phi(r, \psi) d\psi, \quad (3.2.2)$$

Where (r, ψ) are polar coordinates defined as:

$$\zeta = r cos\psi, \quad (3.2.3)$$

And

$$\eta = r sin\psi, \quad (3.2.4)$$

Aki show that there is a one-to-one correspondence exists between azimuthal average of the spatial autocorrelation function, $\overline{\phi(r)}$ and the power spectrum density of the wavefield $\Phi(\omega)$, where ω is the angular frequency (Aki 1957, equation 39):

$\overline{\phi(r)} = \frac{1}{\pi}\int_0^\infty \Phi(\omega) J_0(\frac{\omega}{c}r)d\omega$.(3.2.5)

Where J_0 is the Bessel function of first kind and zero-order. The argument of the Bessel function could also be written as:

$\frac{\omega}{c}r = kr = \frac{2\pi r}{\lambda}$. (3.2.6)

Where k is wavenumber and λ is wavelength.

When the wave is dispersive, we can substitute wavespeed c with $c(\omega)$.

Considering the signal is filtered to specific frequency ω_0, the azimuthal average could be written as (Aki 1957, equation 41):

$\overline{\phi(r)} \equiv \bar{\phi}(r,\omega_0) = P(\omega_0)J_0\left(\frac{\omega_0}{c(\omega_0)}r\right)$. (3.2.7)

Where $P(\omega_0)$is the power spectral density at frequency ω_0.

Define autocorrelation coefficient:

$\rho(r,\omega_0) = \frac{\phi(r,\psi,\omega_0)}{\phi(0,\psi,\omega_0)}$. (3.2.7)

The azimuthal averaged spatial correlation coefficient finally is:

$\bar{\rho}(r,\omega_0) = J_0(\frac{\omega_0}{c(\omega_0)}r)$ (3.2.8)

Aki pointed out that "if measures $\bar{\rho}(r,\omega_0)$ for a certain r and for various ω_0's, one can obtain the function $c(\omega_0)$, i.e. the dispersion curve of the wave for the corresponding range of frequency ω_0". (Aki 1957).

In his 1965 paper, Aki proposed that, by distributing several stations along a circle of radius r, with one station at the center of the circle, and subsequently recording several circles with different radii, an azimuthal average can be computed for each circle and for a fixed frequency ω_0, with r as independent variable in above equation.

Aki also showed in his 1957 paper that when the wavefield under investigation is isotropic, (i.e., the spatial spectral density depends only on the horizontal wavenumber, but not on the direction), the azimuthal average of the spatial autocorrelation function $\overline{\phi(r)}$ could be replaced by $\phi(r,\psi)$, the spatial autocorrelation function for any azimuth ψ. Asten (1976) further prove this in frequency domain and give frequency equivalent representation. The coherency between a station pair separated by distance r, $C(\omega,r)$ could also be represented by a Bessel function:

$C(\omega,r) = J_0(kr)$. (3.2.9)

Therefore, it is possible to use SPAC both in time domain through calculation of correlation coefficient as in equation (3.2.8) and in frequency domain by coherency as in equation (3.2.9).

The final product of the SPAC method is phase velocity dispersion curve. The dispersion curve could then be inverted for shear-wave velocity using standard inversion technique (Herrmann, 2002).

[Major steps of SPAC]

There are three major steps in SPAC method,

(1) Spatial coherency functions between station pairs of fixed distance and different azimuth are computed.

(2) Azimuthal average of the coherency is used to obtain phase velocity dispersion curve.

(3) Phase velocity dispersion curve is inverted for Shear-wave velocity structure.

As shown in the flowchart below, to implement the SPAC method, seismic stations are deployed around circles of different radius at first. Vertical motions of the microtremor are recorded for a period of time. SPAC coefficient could be calculated from microtremors. Phase velocity dispersion curve is then determined using Aki's formula. Finally, S-wave velocity is inverted from dispersion curves.

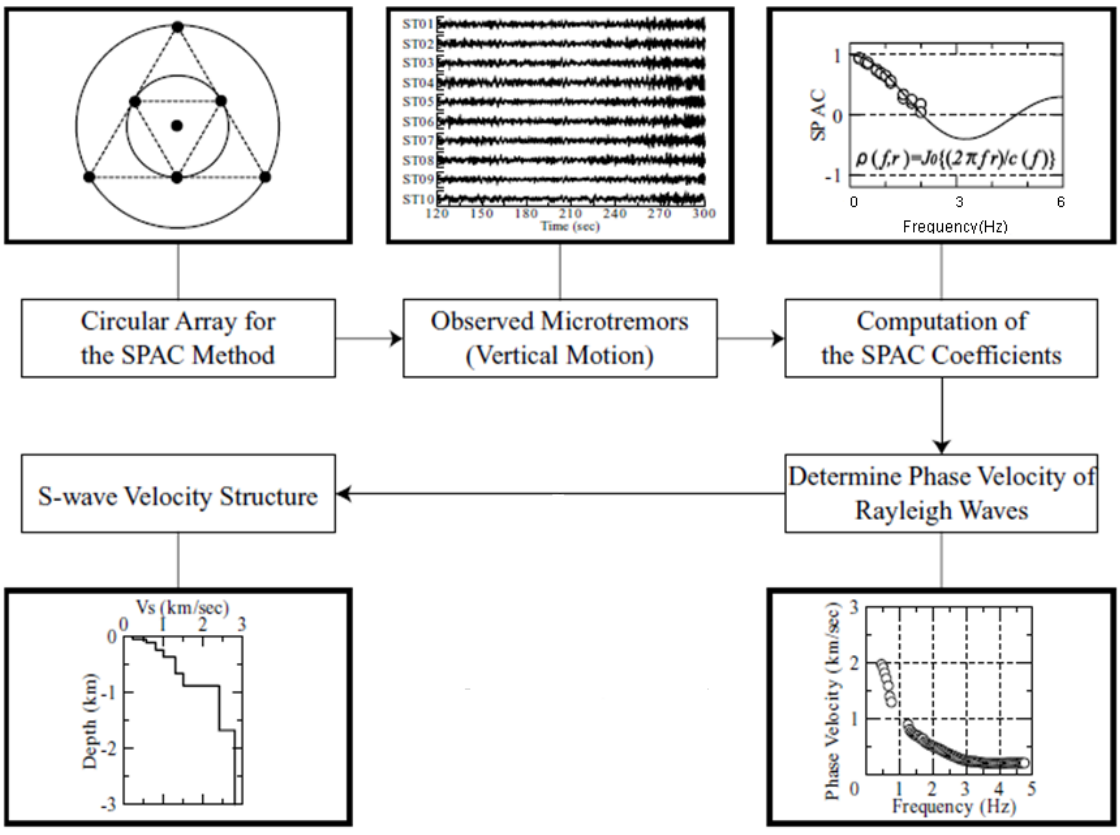

Figure 3.2: Flowchart of SPAC method. (Modified from Kudo et al, 2002)

[Numerical Modeling]

Asten (2006) has given a numerical process of modeling SPAC. The coherency measured by a single pair of geophones can be expressed as:

$$c_{jc}(f) = exp\{ir_{jc}kcos(\theta_{jc} - \phi)\} \text{ . (3.2.10)}$$

Where $c_{jc}(f)$ is the coherency of a single pair of geophones, $r_{jc}$is the displacement of the jth geophone relative to the center geophone c at azimuthal angle θ_{jc}, k is the spatial wavenumber at frequency f, and ϕ is the azimuth of propagation of a single plane wave across the array.

Theoretically, for a single plane wave recorded by an infinite number of geophones placed around a circle centered on a single reference geophone, the summation is expressed as an integration (an azimuthal average) that yields a real SPAC spectrum, which is a Bessel function in theory, as derived by Aki in his 1957 paper (Aki 1957),

Azimuth average: $(f) = \frac{1}{2\pi}\int_0^{2\pi} exp\{irkcos(\theta - \phi)\}d\theta$. (3.2.11)

$$= J_0(rk) = J_0(\frac{2\pi fr}{v(f)}) \text{ . (3.2.12)}$$

Where c(f) is spatially (azimuthally) averaged coherency, J_0 is the Bessel function of the first kind of zero order with the variable rk, f is the frequency, k is the scalar wavenumber, v(f) is the phase velocity dispersion curve, and r is the station separation in the circular array.

The numerical approach to model SPAC is to make the right-hand side of equation (3.2.11) a double summation over a finite number of m plane waves and n geophone pairs, as follow.

$$c(f) = c_r(f) + c_i(f) = \frac{1}{nm}\sum_j^n \sum_i^m \exp\{ir_{jc}kcos(\theta_{jc} - \phi_i)\}. \quad (3.2.13)$$

(Aki 1957, Asten, 2006)

This spatially averaged coherency for a finite sum is in general a complex number with real and imaginary parts $c_r(f)$ and $c_i(f)$. Asten (2003b) and Asten et al (2004) numerically modeled the equation above for finite circular arrays of two to seven stations.

I use the above equation (3.2.13) to numerical model the coherency function. Figure 3.3 shows examples of three and six stations along the circle to illustrate the behavior of SPAC compared with theoretical Bessel function for the finite array.

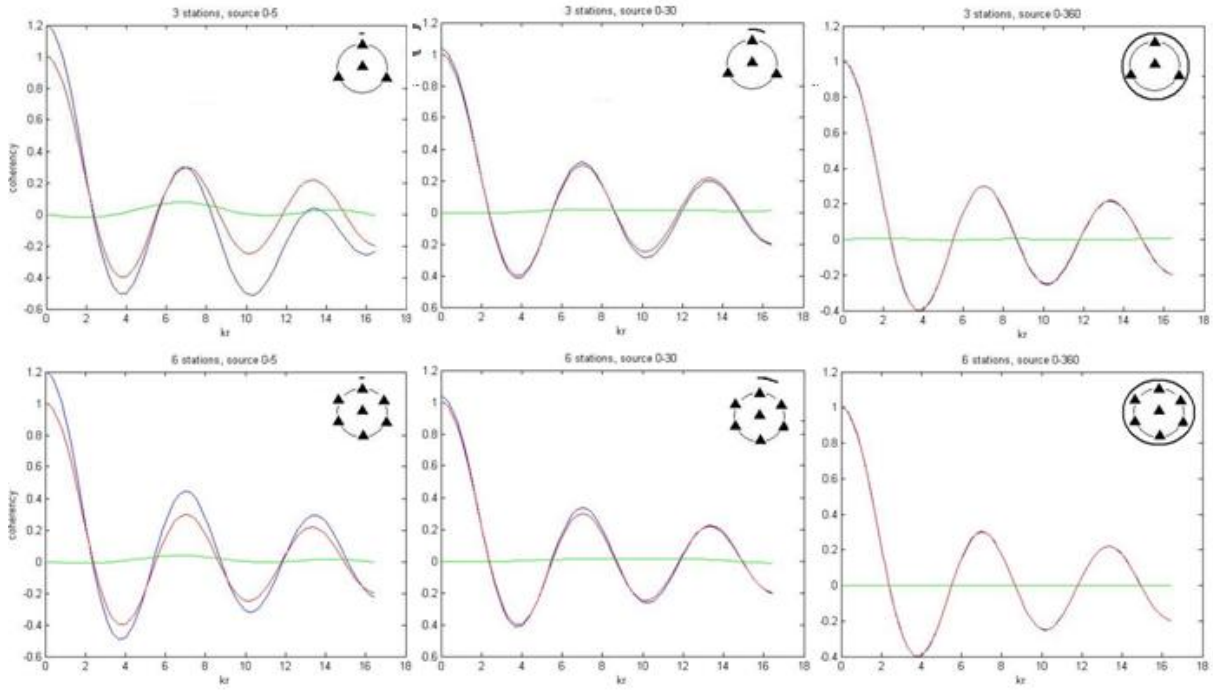

Figure 3.3: upper three: modeled SPAC for a triangular array, n=3, for source azimuth of $5°, 30°, 360°$. Bottom three: hexagon shape array, n=6.

For each panel, the upper-right corner cartoons show stations configuration (black triangle) and direction of incoming sources (black curve outside). The red line is theoretical Bessel function, the blue line is numerical modeled real component of SPAC function and the green line is imaginary component. The figure shows that real component approximates Bessel function better for hexagon array than for triangular array. Aki originally proposed that infinite number of stations along the circle was ideal, but it was difficult to carry out in reality. The approximation also becomes better when the range of incoming sources increases and it matches best when the sources are omnidirectional , i.e. from 360 degree. For first order approximation, calculated SPAC function for three stations array could very well approximate Bessel function when

sources are omnidirectional and the imaginary component is basically zero (Upper rightmost).

[Zero crossing picking of dispersion curve]

One critical step in SPAC method is to calculate dispersion curve using the relation derived by Aki (Equation):

$$\bar{\rho}(r,\omega_0) = J_0\left(\frac{\omega_0}{c(\omega_0)}r\right) \quad (3.2.8)$$

Because direct fitting of a Bessel function in equation (3.2.8) has the usual problems associated with matching waveforms, Ekström et al. (Ekström et al. 2009) proposed the use of zero crossings in the coherence as the dispersion observables, since the zero crossings should be insensitive to variations in the spectral power of the background noise. Since this is a common problem in urban noise studies, we use Ekström et al.'s (Ekström et al. 2009) method to obtain invertible dispersion curves from spatially averaged coherence. Ekström associate the zero crossings of coherency with corresponding Bessel function,

$$c(\omega_n) = \frac{\omega_n r}{z_n}. \quad (3.2.14)$$

Where $\omega_n$denotes the frequency of the nth observed zero crossing and z_n denotes the nth zero of Bessel function, r is inter-station distance, the corresponding phase velocity at frequency ω_n can be determined by above formula. Because observed coherencies are always noisy, it might not be obvious to associate a given zero with a particular zero

crossing of Bessel function due to missed or extra zero crossings. Ekström et al. (2009) proposed an estimation of a suite of dispersion curves to allow for missed or extra zero based on equation 3.2.14,

$$c_m(\omega_n) = \frac{\omega_n r}{z_{n+2m}}. \quad (3.2.15)$$

Where m takes the values of 0, ± 1, ± 2 …., indicating the number of missed or extra zero crossings. The final observed dispersion data is picked from these suites of dispersion curves with the most reasonable one falling within a realistic range.

After obtaining the phase velocity dispersion data from above formula, standard inversion techniques can then be applied to invert for Shear-wave velocity.

[Synthetic test: two-layers]

We calculated the synthetics using forward modeling to test the stability of picking dispersion data by Ekström's zero-crossing method. We forward calculated the dispersion curve using a simple 1-D two-layer (one layer over half-space) Earth model with materials parameters indicated in the figure below.

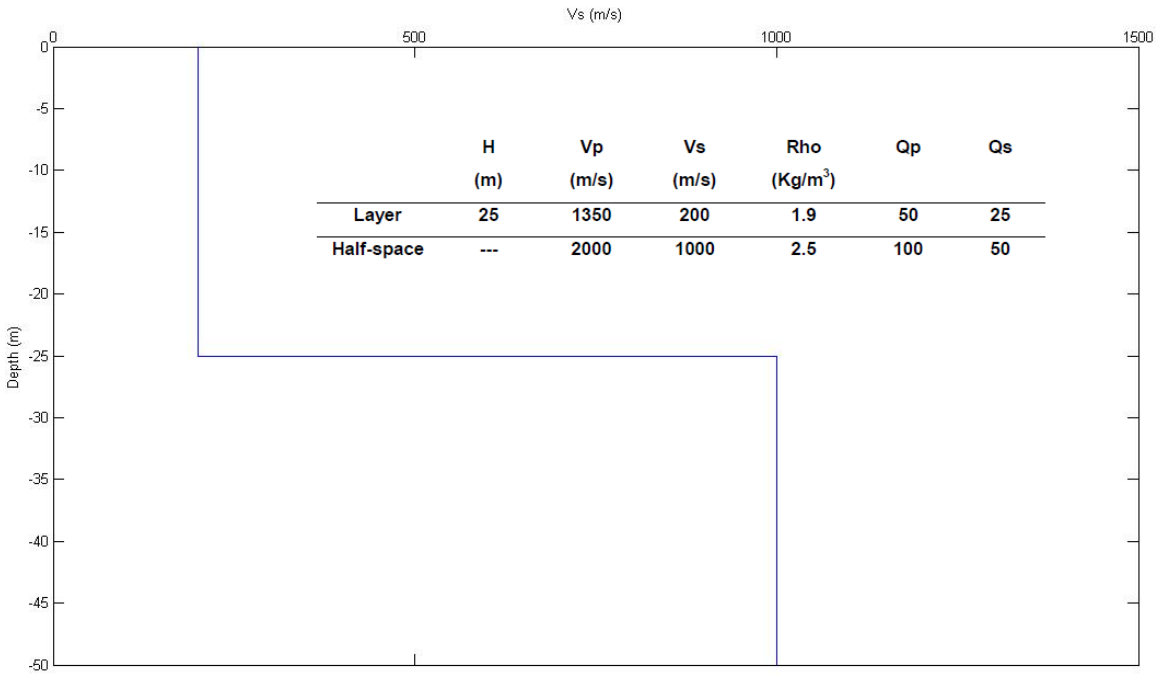

Figure 3.4: Earth model used for forward calculation of dispersion curve

In figure 3.4, H is layer thickness, Vp and Vs are P and S wave velocity respectively, Rho is density, Qp and Qs attenuation factor for P and S wave. Forward calculated dispersion curves are show in the figure below with the fundamental mode and first higher mode.

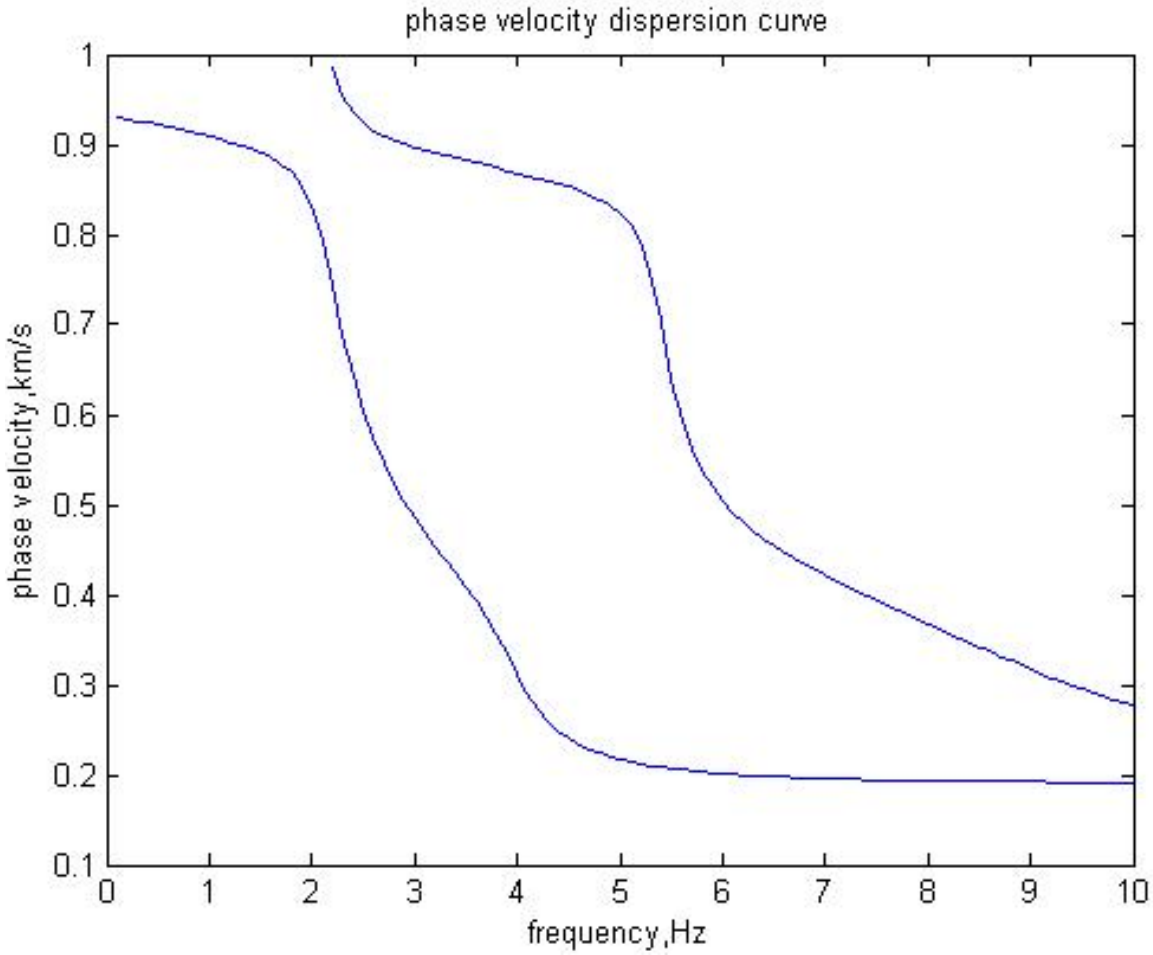

Figure 3.5: fundamental-mode and first higher mode dispersion curve calculated from Earth model in Figure 3.4.

We calculate the SPAC coefficient as a function of kr using Aki's formula. We perturb the forward calculated SPAC with different levels of white noise to mimic real world scenarios, because real world SPAC coefficient calculated from microtremors usually contain various level of noise. We ran a moving average on the noise-added SPAC function to smooth the curve. We then picked the zero-crossings of the smoothed curve using Ekström's method and compared them with theoretical Bessel function to calculate the dispersion curve. Our results are very consistent with what Ekström has pointed out,

that although the amplitude of the SPAC may fluctuate and tend to deviate from theoretical Bessel function when noise level is high, the zero-crossings of the SPAC function are very stable and robust. The recovered dispersion data are then compared with theoretical calculated dispersion curve, indicating very well fit (Figure 3.6).

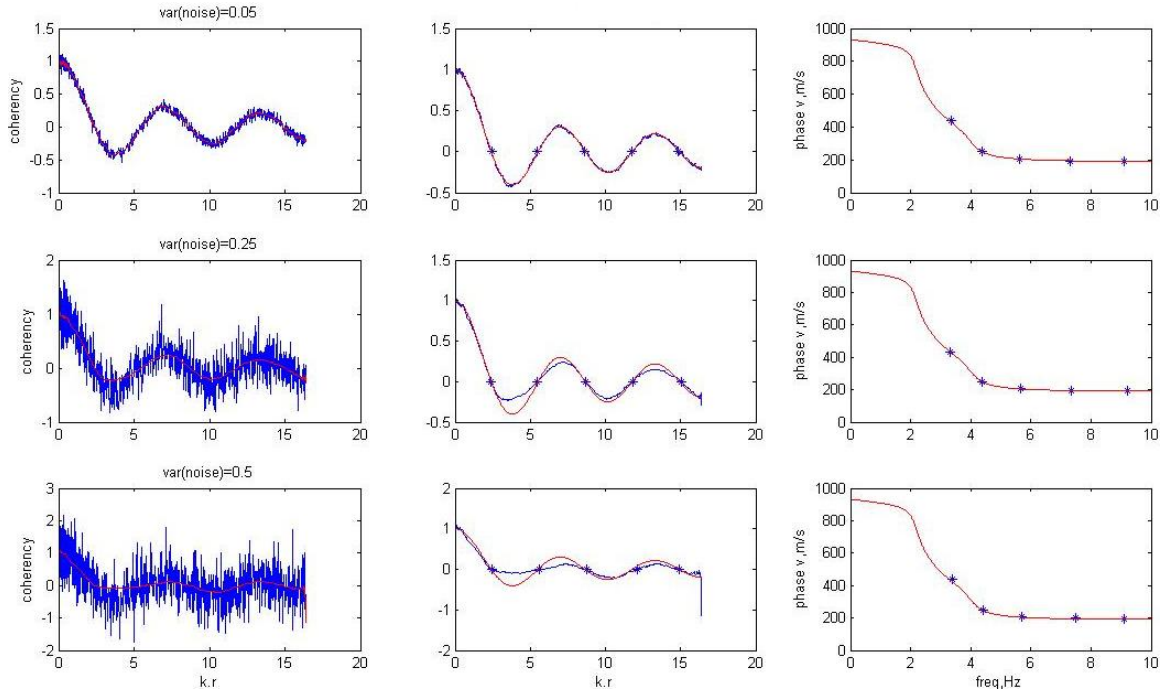

Figure 3.6: Synthetic SPAC function with inter-station distance r=50m. From top to bottom: different level of noise (white noise variance 0.05, 0.25, 0.5) added to forward calculated SPAC function. Blue lines in the three panels of left-most column represent noise-added SPAC function, and red lines represent moving averaged SPAC function. In the three panels of the middle column, the smoothed functions (blue) are then compared with theoretical Bessel function (Red), blue star indicate zero-crossing of smoothed function. The three panels of right-most column show theoretical dispersion curve (red) and calculated dispersion data using Ekström's method (blue star).

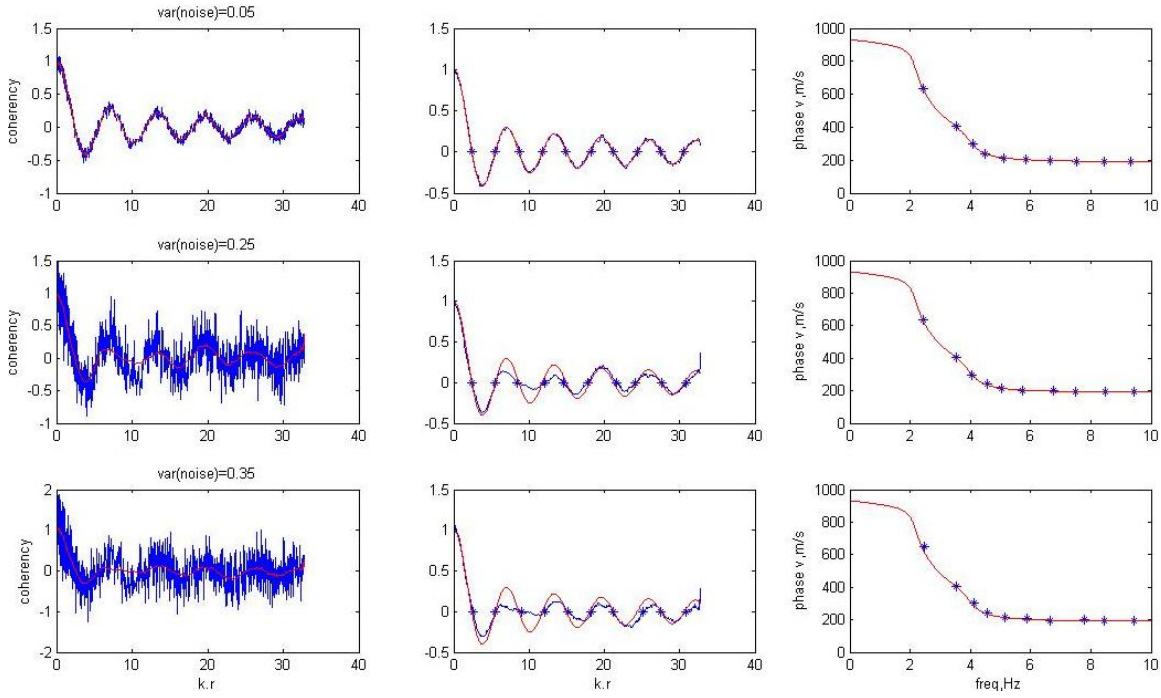

Figure 3.7: legends are same as figure 3.6, while this is calculated for inter-station distance r=100m.

Figure 3.6 and 3.7 show that more cycles of the Bessel function and thus more zero-crossings are expected as indicated by Aki's formula, because of the increasing value r in the arguments of Bessel function while other parameters remain unchanged. As noise level increases, the amplitude of smoothed SPAC function (Blue line in the middle column) deviate from theoretical Bessel function (Red line in the middle column), while the zeros (Blue star in the middle column) are quite stable. The recovered dispersion data (blue star in the right-most column) match well with theoretical dispersion curves (red line in the right-most column). The synthetic test shows the robustness of calculation of dispersion data from microtremor coherency function using SPAC methodology.

3.3 Inversion

Various inversion techniques could be applied to the calculated dispersion curve from SPAC method to invert for shear-wave velocity. I will discuss different inversion techniques in detail in the inversion chapter (Chapter 4). Standard linear least-square inversion (LSI) is the most straightforward one and has been widely used for inversion of dispersion data (Xia et al 1999, Warren et al 2008). Herrmann (2002) develop a standard code of LSI to do the dispersion curve inversion in his program and has been widely adapted. I use Herrmann's code to invert for Vs from dispersion data, and then develop more advanced inversion techniques in Chapter 4.

3.4 Charleston, South Carolina case study

[Introduction]

Charleston, South Carolina and vicinity was struck by a devastating M=6.9-7.3 earthquake on August 31, 1886 (Johnston, 1996; Bakun and Hopper, 2004), killing over 150 people and damaging >90% of the city's masonry structures (Côté, 2006). Continuing low-level seismicity (e.g., M=3.2 felt event, August 29, 2009) and extensive paleoliquefaction evidence (Talwani and Schaeffer, 2001) of past events have led to the Charleston vicinity being assessed the second highest seismic hazard in the United States east of the Rocky Mountains (Petersen et al., 2008). This high level of seismic hazard is an important public concern in Charleston, as evidenced by a recent seismic safety study of schools conducted by the Charleston County School District (http://www.ccsdschools.com/Departments_Staff_Directory/Capital_Improvements/seismic/index.php).

Currently, seismic site classification in Charleston is done primarily using the Seismic Cone Penetrometer Test (SCPT; see school seismic safety referenced above as an example) method and a database of SCPT boreholes is available (Chapman et al., 2006; Jaumé, 2006). Shear wave velocity has also been estimated using the refraction microtremor (ReMi) method at several locations in Charleston (Jaumé, 2006; Jaumé and Levine, 2008), including sites where SCPT has been conducted. These pre-existing shear wave structure studies make Charleston an attractive place to test additional methods of estimating shear wave structure.

We used the SPAC method to determine shallow shear wave velocity at sites in Charleston, South Carolina and vicinity where the shear wave structures are known via other methods. We evaluated the efficiency of the SPAC method both in terms of its ability to recover known shear velocity values and its ability to be utilized in the dense urban setting of historic downtown Charleston. In addition, we examined methods of integrating the SPAC results with refraction microtremor (ReMi) and Seismic Cone Penetrometer Test (SCPT) results already collected in Charleston, South Carolina.

[Experiment]

We conducted a pilot SPAC study in Charleston, South Carolina in early April 2010. We choose three locations in the Charleston area where previous shear wave velocity measurements (SCPT and/or ReMi) have been conducted (yellow squares in geology map, Figure 3.8). We used a triangle array with one station in the center and three at the

vertex of the triangle, as done for example by Stephenson et al. (2009). We deployed seismometers at 10 meter, 30 meter, and 60 meter, interstation distances (Figure 3.9). Approximately 30 minutes of microseismic noise were recorded at each station using CMG-6TD digital broadband seismometers owned by the College of Charleston.

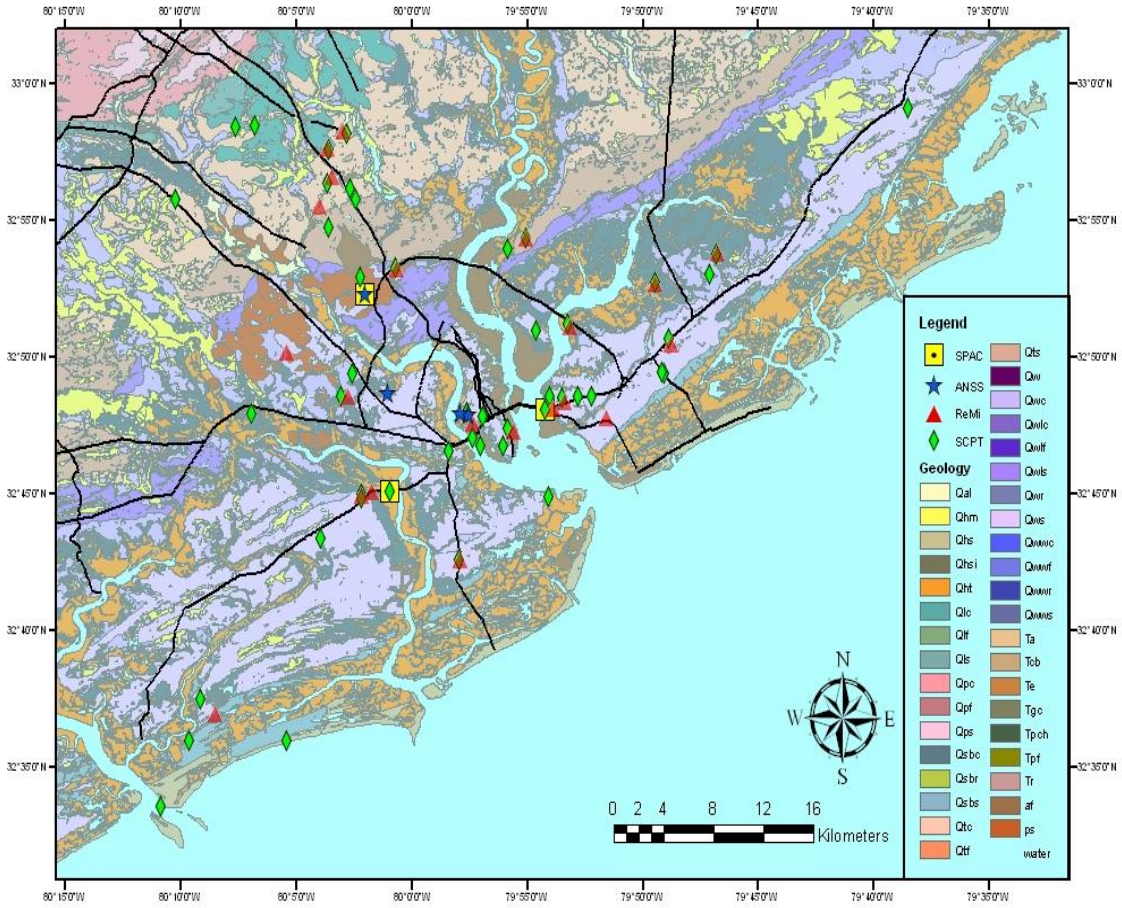

Figure 3.8: Geological map of Charleston, South Carolina and vicinity with ANSS strong motion sites (blue stars), ReMi surveys (red triangles), SCPT boreholes (green diamond) and the three sites where we conducted a SPAC survey in the spring 2010 (yellow squares) marked.

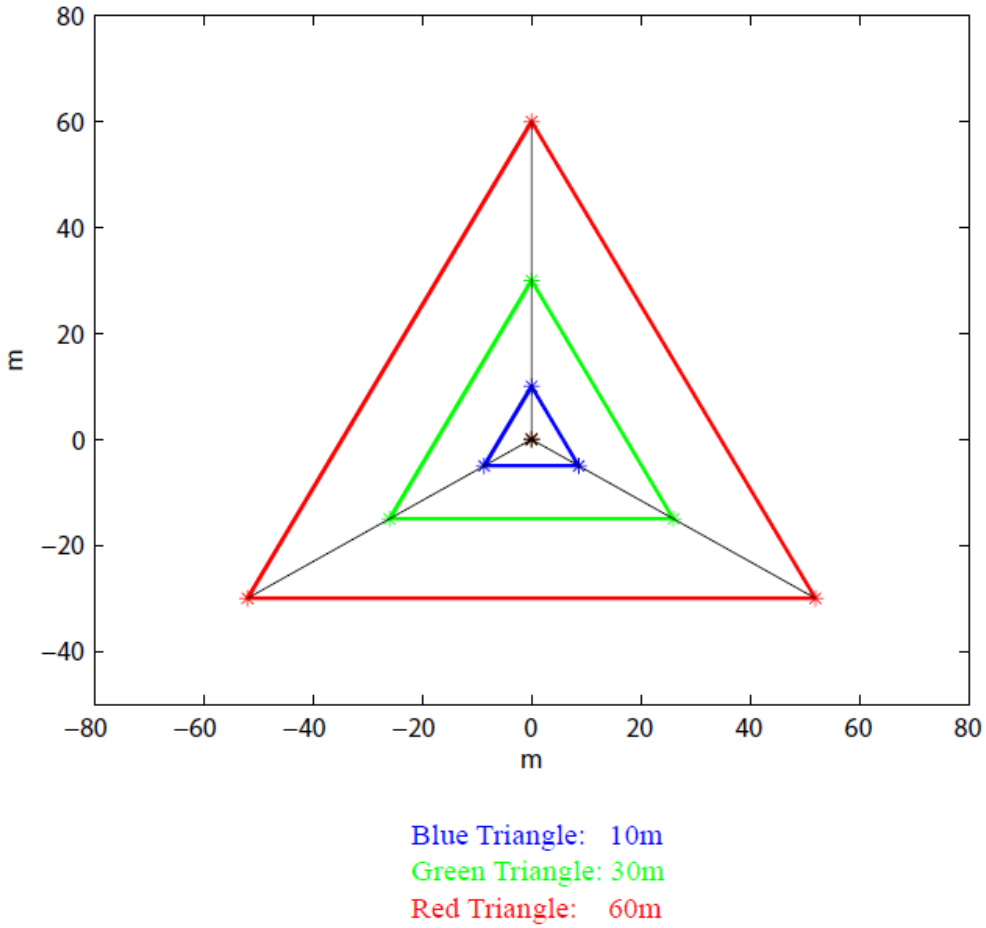

Figure 3.9: Array setup for SPAC study conducted in Charleston in April 2010. We use a triangle array with one station in the center and three at the vertex of the triangle. We deployed instruments at 10 meter, 30 meter, and 60 meter interstation distances. Different color represent different size array, stars indicate stations. Center station remains fixed while outside three are re-deployed accordingly.

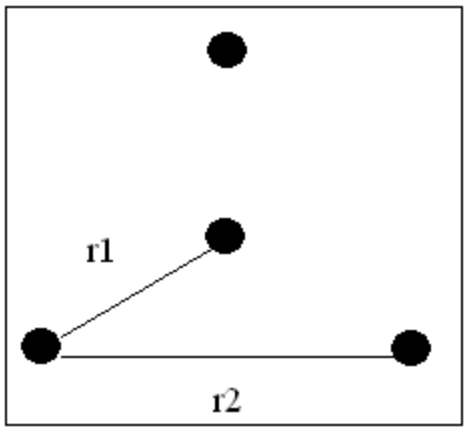

Figure 3.10: For each triangle array, there are two different interstation distances, r1 and r2 for calculating coherency.

From microtremor data we collected at three sites, we calculated the SPAC function following the procedure described in section 3.2. We then calculated the dispersion curve using zero-crossing method. The dispersion data are then inverted for shear wave velocity using Herrmann's code (Herrmann 2002).

[Results]

Figure 3.11 shows an example of the coherency at the Waterfront park. For each triangle, there are two different interstation lengths (Figure 3.10), for three triangles array in one site, there are a total of six different interstation distances. Six panels represent six different interstation distances from 10m to 104m. The blue lines are coherency, while the red lines indicate coherency zero. A clear pattern can be seen from the figure that as interstation distance increases, we get more zero crossings, and the first zero migrates

from higher frequency of 15Hz at r=10m to lower frequency of 3Hz at r=104m. This is consistent with Aki original formula and synthetic test's result.

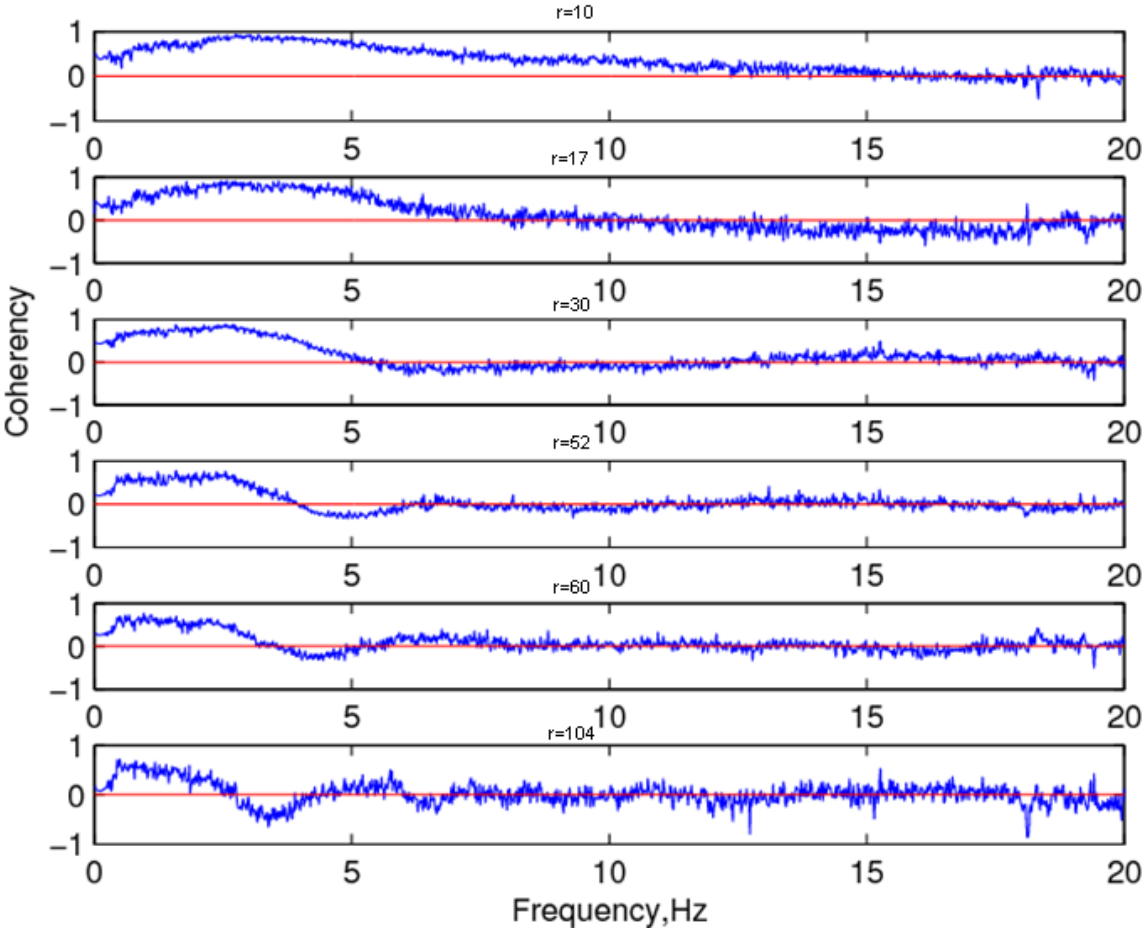

Figure 3.11: Coherency function calculated for the Waterfront Park site. From top to bottom: Interstation distance r increase from 10m to 104m. Blue line represent coherency, red line indicate coherency zero.

I used moving average method to smooth the coherencies. After experimenting different lengths smoothing windows, the results show that the positions of zeros of the coherency do not change significantly with window lengths. I, therefore, chose the averaging window with the length of 10% of the total length of the coherency. I picked the zeros of

coherency curve and associated the zeros with Bessel function's zero crossing follow Ekström et al.'s method (formula 3.2.14). Taking into account of possible missed or extra zeros in the coherency compared with the Bessel function, I used equation 3.2.15 to generate a suite of dispersion curves and select the one that fall within the realistic range. Figure 3.12 displays the suite of dispersion curves for interstation distance 30m,

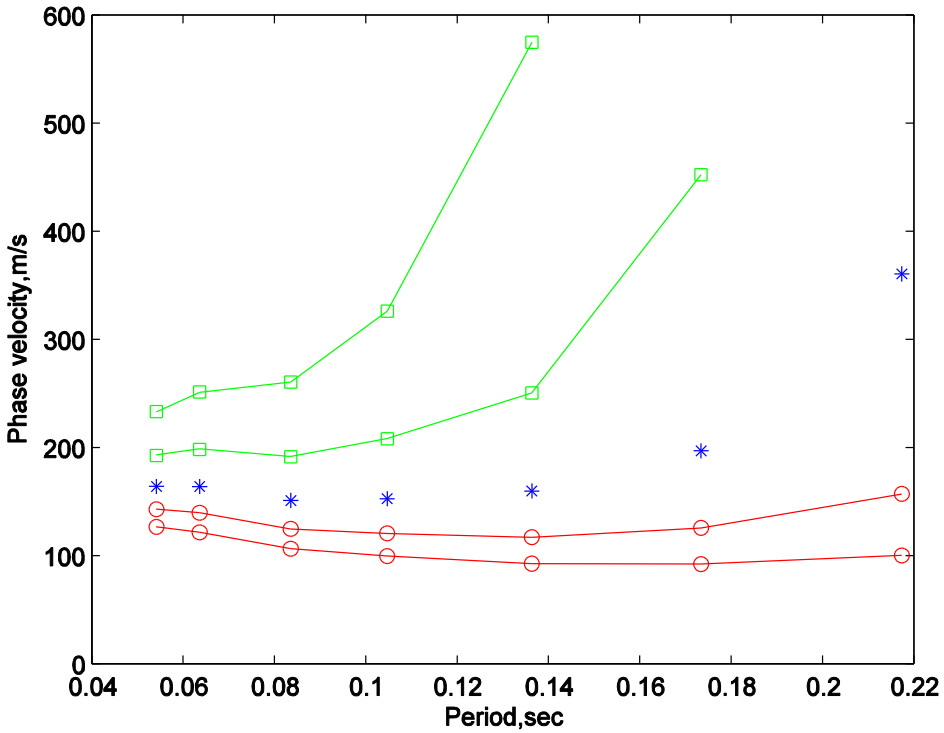

Figure 3.12: A suite of dispersion curve taking into account of missed or extra zeros when comparing observed coherency with the Bessel function. Green square: extra 1 and 2 zeros of coherency. Red circle: missing 1 and 2 zeros of coherency. Blue star: no missing or extra zero.

In Figure 3.12, among all dispersion curves, the one without any missing or extra zeros (blue star) is the most realistic one, especially considering the value of phase velocities at long periods (>0.1 second). I used the same algorithm to generate large suite of

dispersion curves for all interstation distances and discards all curves with unacceptable phase velocity values. The finally obtained observed dispersion data is shown in Figure 3.13.

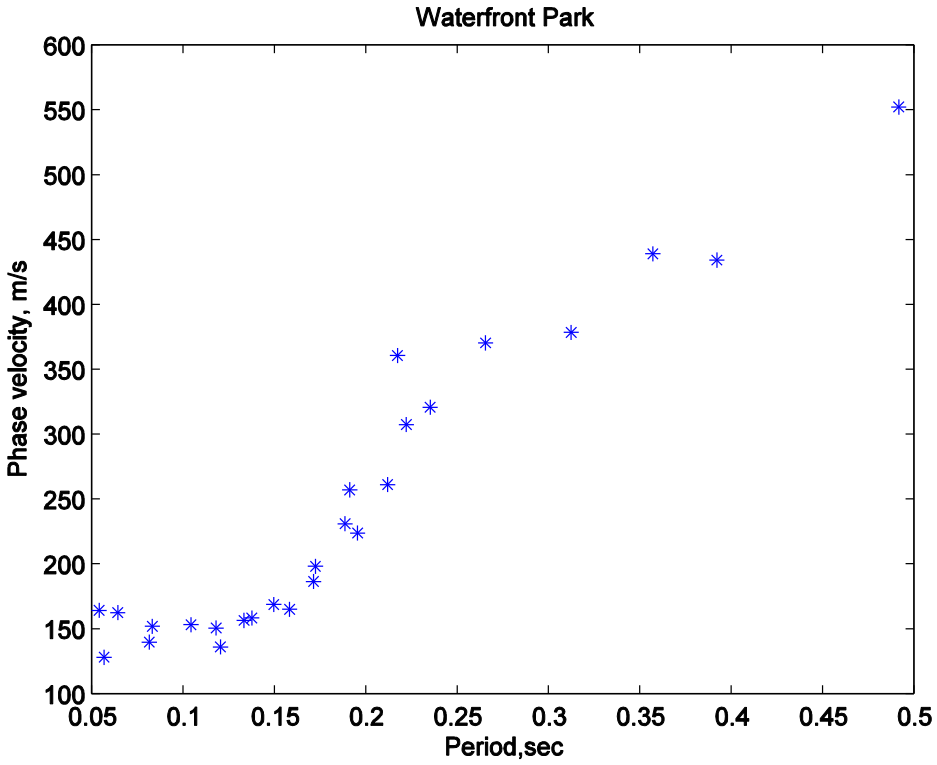

Figure 3.13: observed dispersion data getting from SPAC method.

I inverted for S-wave velocity structure from phase-velocity dispersion data by linearized least-squares inversion (LSI) method (Herrmann 2002).

I also constructed a 5 layer starting model, with fixed layer thickness of 6 meter, with constant P- and S-wave velocity, attenuation, and density for each layer. (Warren et al 2008).

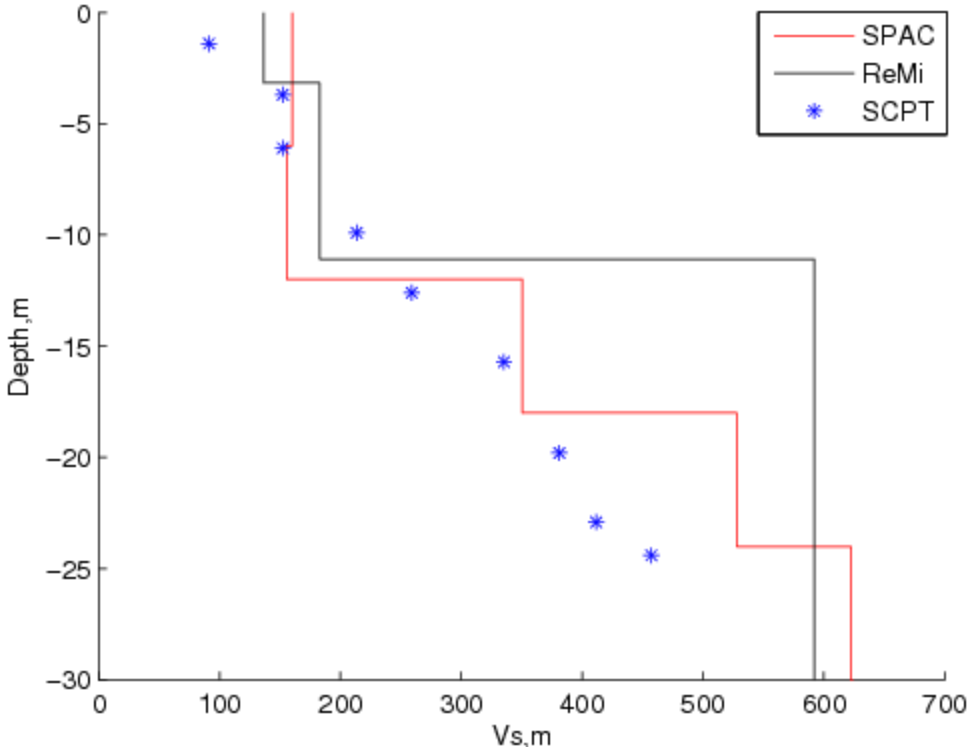

Figure 3.14: Waterfront park. Comparison of S-wave velocity structure obtained from SPAC (red line) with SCPT (blue star) and Refraction Microtremor (blue line)

I compared the Vs structure inverted from SPAC method with borehole measurement of SCPT and Refraction Microtremor results (Figure 3.14). It shows that the SPAC results agree with SCPT data. The SPAC result does not go exactly with the ReMi model, since previous ReMi method only invert for three layers, but the general velocity increasing trend is consistent in all three methods.

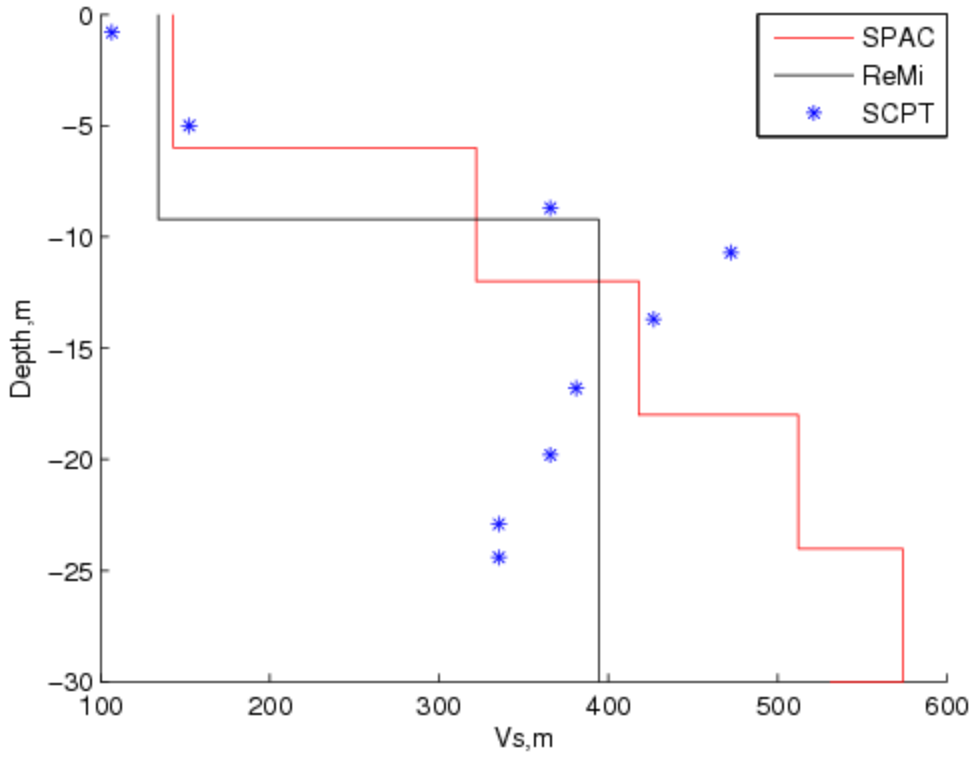

Figure 3.15: Maybank bridge (MBB) site. Comparison of S-wave velocity structure from SPAC (red line) with SCPT (blue star) and Refraction Microtremor (blue line).

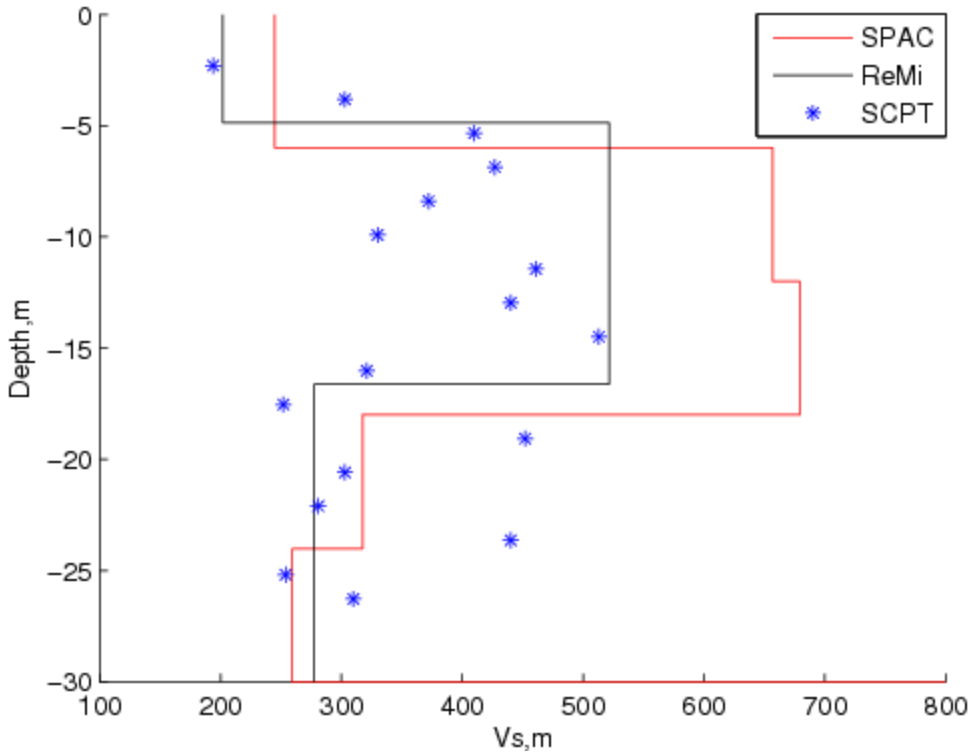

Figure 3.16: Trident Research center (TRC) site. Comparison of S-wave velocity structure from SPAC (red line) with SCPT (blue star) and Refraction Microtremor (blue line).

Figure 3.15, 3.16 are inverted shear wave velocity from two other sites, Maybank bridge (MBB) and Trident Research Center (TRC). Both of these two sites indicate a decreasing velocity, or low velocity zone (LVZ) below 10m. For TRC, the SCPT data is very scattered, but it falls into the range of SPAC and ReMi results. This is a drawback of borehole method as discussed previously (section 3.1). SCPT measurement is usually discrete data points and could not accurately capture features like velocity jumps and low-velocity zone.

We calculated the Vs30 for all three sites and classify the sites according to NEHRP soil classification table (www.nehrp.com). The Vs30 and the soil classes are given in Table 3.2. The determined Vs30 from SPAC are comparable with the Vs30 from ReMi and SCPT. Vs from SPAC are all within 5% of Vs from SCPT, and 15% from Vs from ReMi. All methods classify the site as soil classes D according to NEHRP classification.

Site	SPAC	SCPT	ReMi	Class
WFP	263 m/s	255 m/s	304 m/s	D
MBB	307 m/s	291 m/s	247 m/s	D
TRC	354 m/s	325 m/s	316 m/s	D

Table 3.2: Comparison Vs30 calculated using three different methods (SPAC, ReMi and SCPT) and Soil class for three sites (WFT, MBB and TRC) in Charleston.

3.5 New York City microtremor study

The New York City metropolitan area, with a population of more than 8 million, is the most populous city in United States, and is one of the largest cities in the world as well. About one-fifths of the total population lives in the heart of the New York City, the Manhattan Island. Although the east coast of U.S. is considered to have less seismic hazard than the west coast, Manhattan is still considered to have high seismic risk because of its large population, high economic value, and dense skyscrapers and critical infrastructures in the city. Accurate site characterization is thus extremely necessary for urban seismic hazards study. As discussed in the beginning of this chapter, shear wave velocity information is useful for seismic hazards study in terms of site response and ground motion prediction. Traditional techniques of inferring Vs information including

borehole drilling methods and active sources seismic survey methods are not easy to carry out in the big metropolitan area of the New York City, especially in the densely populated lower Manhattan area with lots of high-rise buildings. As discussed previously in this chapter, SPAC method stands out because of its significant advantages over other methods, including easy deployment and not requiring sources and drilling. A microtremor study is conducted by USGS in the New York City in 2007 to investigate the shear wave velocity structure and depths of high velocity contrast (soil-bedrock). Microtremor data are collected at six sites in lower Manhattan to evaluate the effectiveness of estimating Vs profile using SPAC method in the world largest metropolitan area (Figure 3.17).

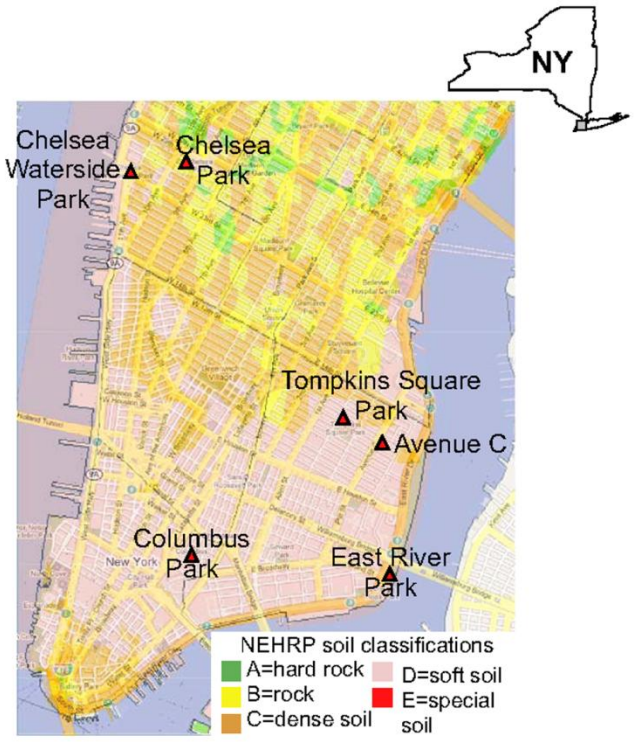

Figure 3.17: Map of lower Manhattan showing location of sites for SPAC study. (From Stephenson 2009)

Site	10m	30m	60m
Chelsea Waterside Park (CWP)		X	X
Chelsea Park (CP)	X	X	X
Columbus Park (COL)	X	X	X
East River Park (ER)		X	X
Tompkins Square Park (TSP)	X	X	

Table 3.3: Array size used for SPAC at each 5 sites.

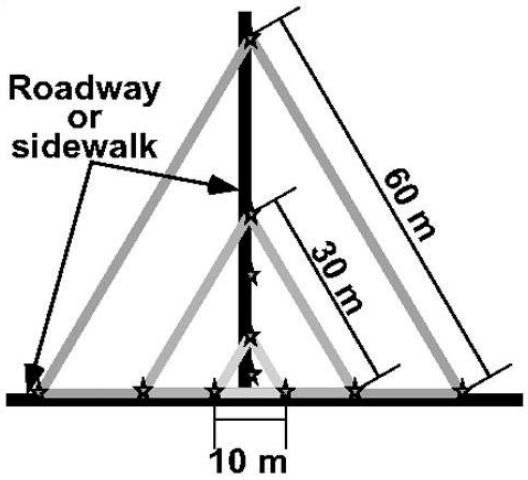

Figure 3.18: Triangular array used for Manhattan SPAC study. Three gray triangles represent 10, 30, 60m array size. (From Stephenson 2009)

Different sizes triangular array are used at each site based on space available (Table 3.3). 30 minutes microtremor data are acquired using four seismometers for each array (Figure 3.18). The selected sites are city parks, sidewalk and roadway. I estimate the Vs structure of five sites with the same SPAC method as for Charleston.

Figure 3.19 gives an example of the calculated coherency spectrum at TSP site.

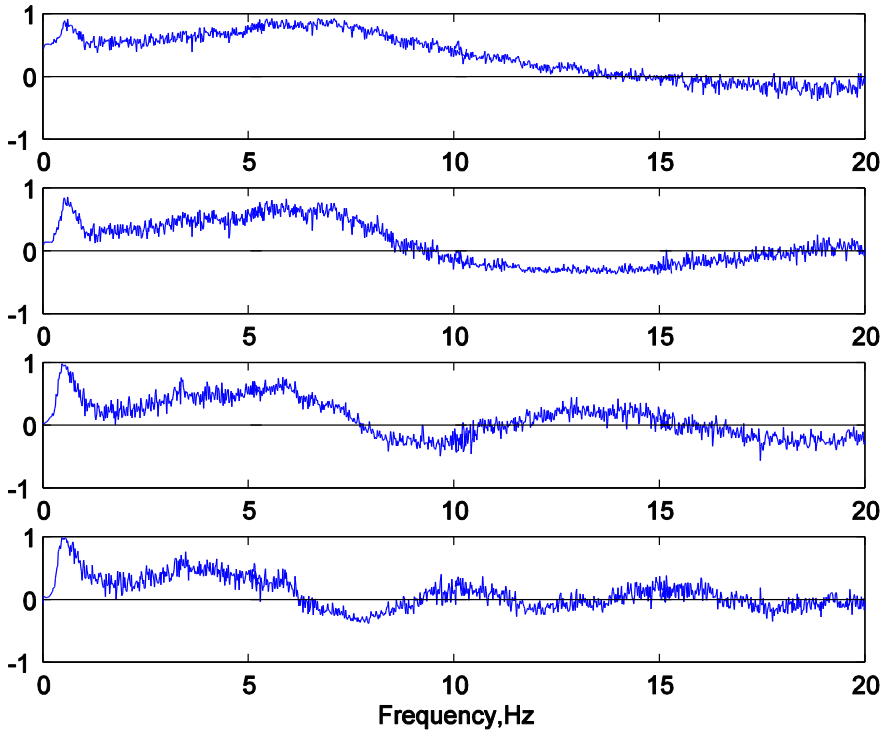

Figure 3.19: TSP site coherence, from top to bottom: interstation distance 5.77, 10, 17.32 and 30m.

Dispersion data is calculated from associated the zeros of coherence with zeros of Bessel function. (Figure 3.20)

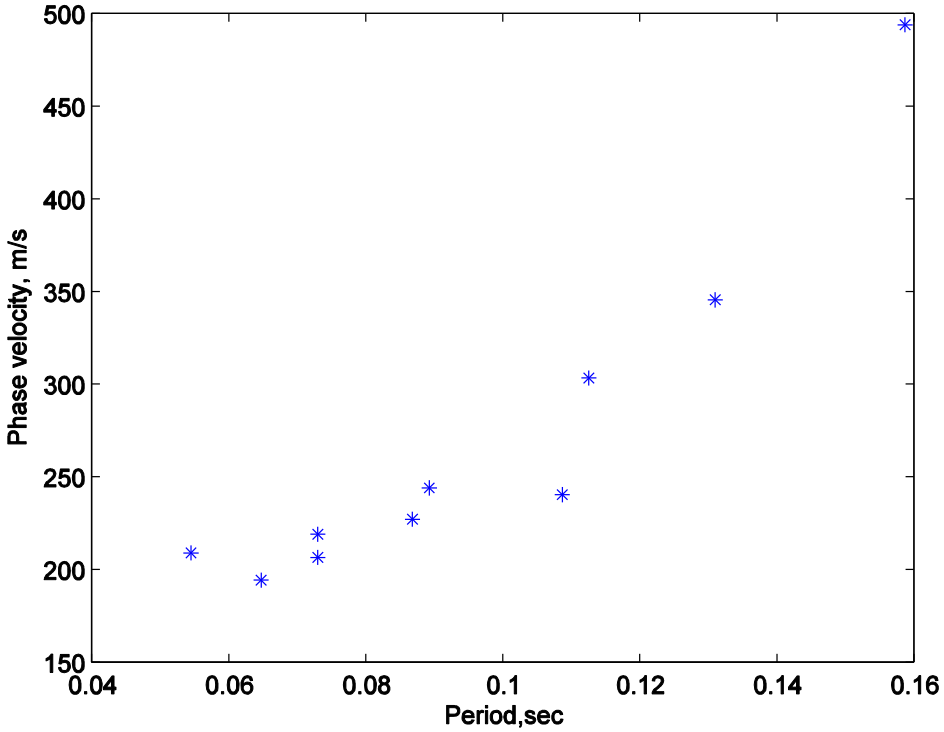

Figure 3.20: TSP site. Observed dispersion data from microtremor coherence spectrum.

Vs structure is inverted from the dispersion data using linear inversion (Herrmann 2001).

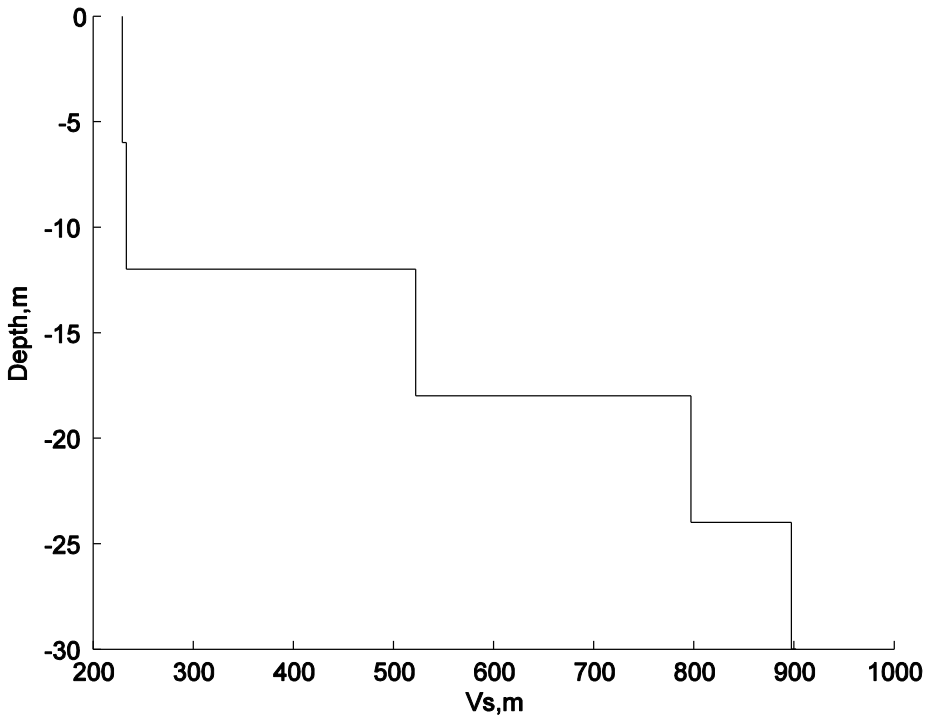

Figure 3.21: TSP site. Linear inverted Vs structure.

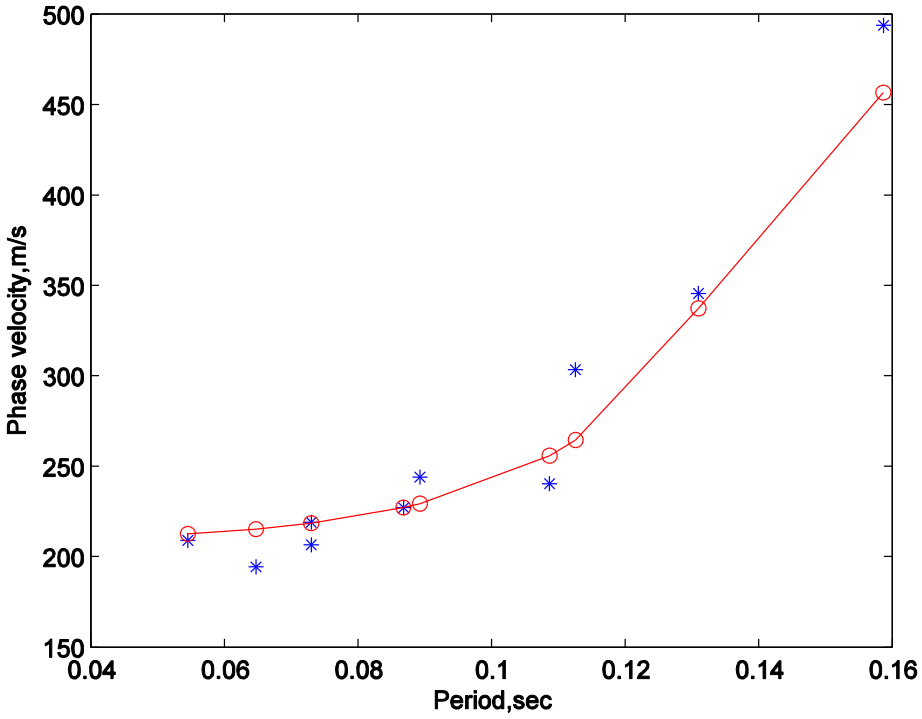

Figure 3.22: TSP site. Forwarded calculate dispersion curve (red circle) compared with observed dispersion data (blue star).

The forward calculated dispersion curve from the inverted Vs using linear inversion fit into the observed dispersion data very well (Figure 3.22).

Previous studies (Baskerville, 1994) have found that the bedrock underneath lower Manhattan is mainly late Proterozoic to Paleozoic metamorphic rocks with depth range from outcropping to > 55m. Soil deposits primarily consist of glacial units, tidal deposits and man-made fill. Thus, the low velocity soil materials, Vs ranges from 140m/s to 300 m/s, overlying high velocity bedrock, Vs around 2000 m/s is the typical subsurface structure in lower Manhattan. The linear inverted Vs (Figure 3.22) does not quite catch

the sharp velocity contrast between shallow soil and underlying bedrock. To estimate the soil-to-bedrock layer thickness, we need to use prior information regarding to the soil and bedrock Vs.

Instead of linear inversion, I used the grid search method to estimate the soil-to-bedrock depth. I inverted for the two-layer Vs model, letting first layer's soil Vs to range from 150 m/s to 250m/s, and fix the second layer's bedrock Vs at 2000m/s. I chose the layer thickness ranging from 4m to 40m and find the Vs model that could well explained observed dispersion data. I compared the two-layer Vs model with the Vs interpreted by Stephenson et al. (Stephenson et al 2009), as well as the estimated bedrock depth information from geological map (Baskerville 1994). The Vs for TSP site is given in Figure 3.23.

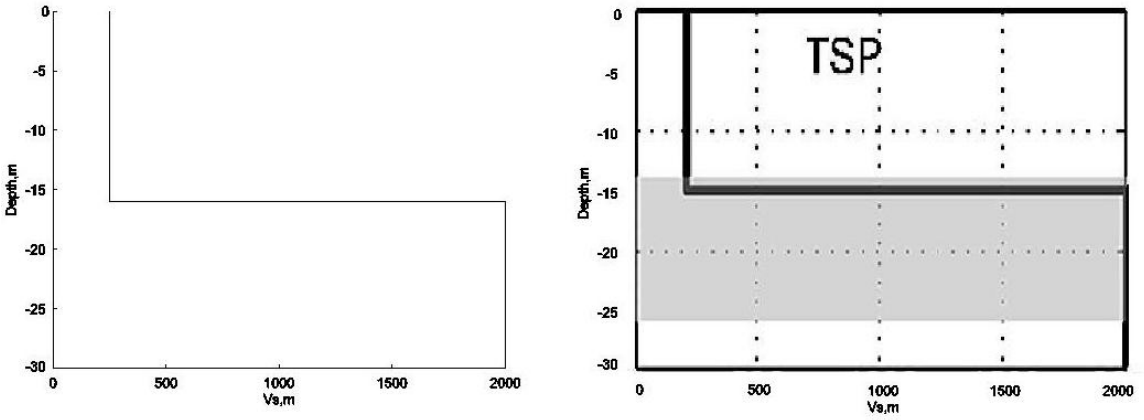

Figure 3.23: TSP site. Left: two-layer Vs model using SPAC method. Right: Interpreted Vs from [Stephenson et al 2009]. Dark black line: Joint interpreted Vs by three authors. Grey area: zone of expected bedrock depth based on maps of Baskerville [1994].

Figure 3.23 shows that the inverted Vs from SPAC using grid search method is very consistent with the Vs interpreted by Stephenson et al. The depth of bedrock is estimated to be 16m, which is very close to the expected bedrock depth of 15m from the geological map (Baskerville, 1994). I invert for the Vs for other four sites using grid search method, the results are given in Figure 3.24 to 3.27.

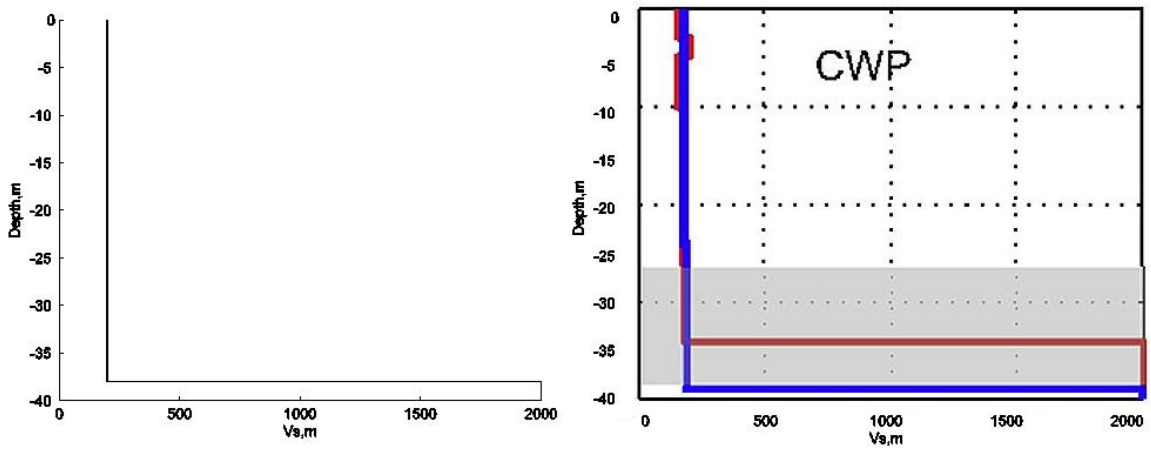

Figure 3.24: CWP site. Left: two-layer Vs model using SPAC method. Right: Interpreted Vs from (Stephenson et al 2009). Red and blue lines denote two Vs models estimated independently by two authors Stephenson [WS] and Hartzell [SH]. Grey area: zone of expected bedrock depth based on maps of Baskerville (1994).

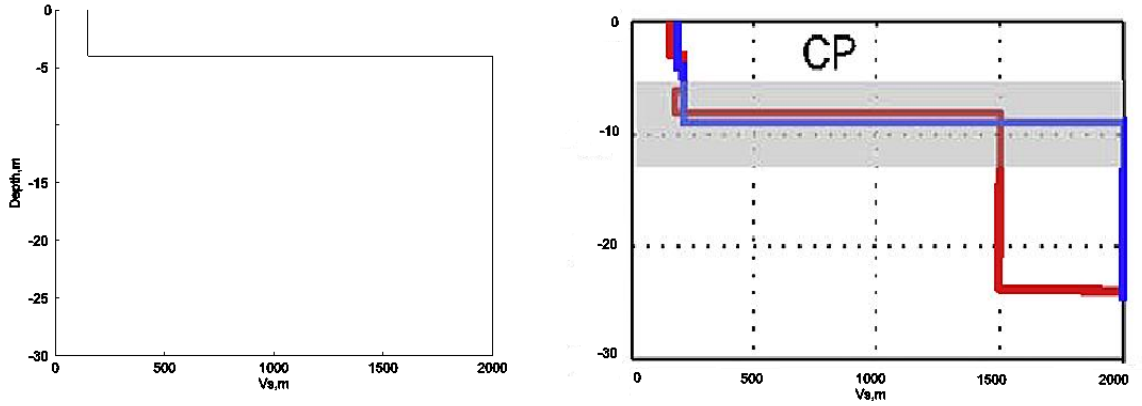

Figure 3.25: CP site. Left: two-layer Vs model using SPAC method. Right: Interpreted Vs from (Stephenson et al 2009). Red and blue lines denote two Vs models estimated independently by two authors Stephenson [WS] and Hartzell [SH]. Grey area: zone of expected bedrock depth based on maps of Baskerville (1994).

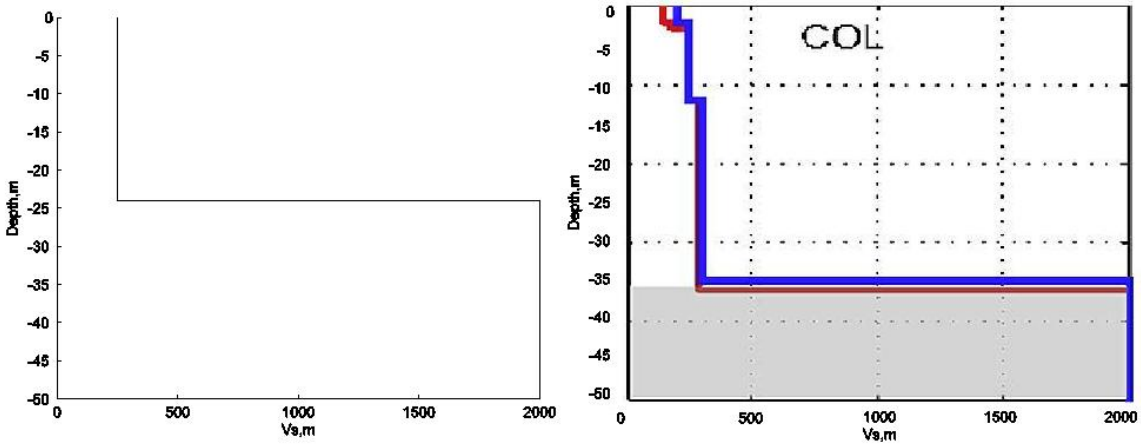

Figure 3.26: COL site. Left: two-layer Vs model using SPAC method. Right: Interpreted Vs from (Stephenson et al 2009). Red and blue lines denote two Vs models estimated independently by two authors Stephenson [WS] and Hartzell [SH]. Grey area: zone of expected bedrock depth based on maps of Baskerville (1994).

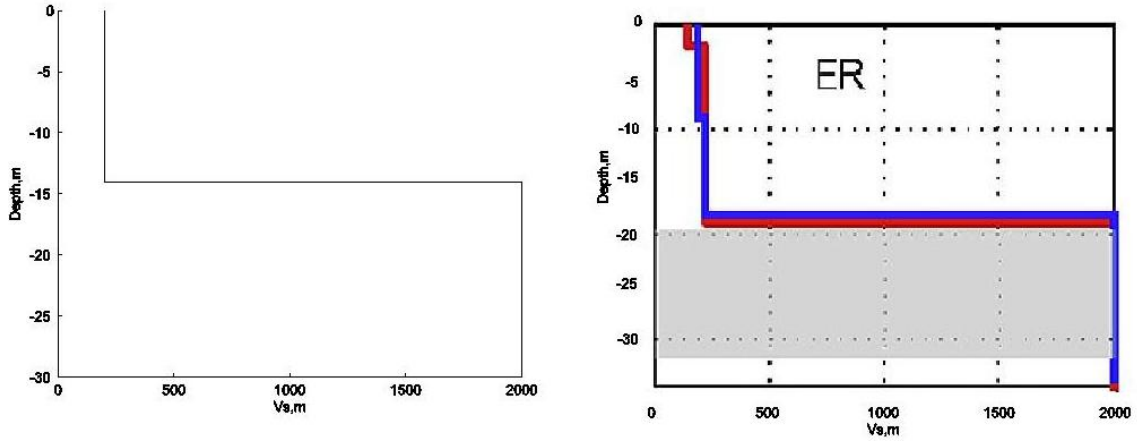

Figure 3.27: ER site. Left: two-layer Vs model using SPAC method. Right: Interpreted Vs from (Stephenson et al 2009). Red and blue lines denote two Vs models estimated independently by two authors Stephenson [WS] and Hartzell [SH]. Grey area: zone of expected bedrock depth based on maps of Baskerville (1994).

The inverted Vs structures correlate well with the Vs obtained by Stephenson et al. The estimated depths of bedrock are also consistent with the expected bedrock depth based on previous geological information.

The study in Manhattan using SPAC method shows that reliable Vs information could be obtained by analyzing microtremor data. SPAC method is proved to be effective for site characterization in the metropolitan area.

3.6 Conclusion

In this chapter, I thoroughly discussed the SPAC methodology of estimation shallow shear wave velocity structure from microtremor data. After summarizing the importance of obtaining shear wave velocity information for earthquake site-response study, I

reviewed existing methods of estimating shear wave velocity. SPAC method stands out because of its non-destructive nature, its easiness to carry out, and its insensitivity to sources. By reviewing theoretical basis laid out by Aki in 1950s, I carried out numerical modeling to test the applicability of obtaining SPAC coefficient using triangle array, and it has shown that when sources are omnidirectional, the SPAC function obtained from triangle array could well approximate the theoretical Bessel function. One critical step in SPAC method is to calculate dispersion curve from SPAC function. I used the method proposed by Ekström, in which zero-crossings of SPAC function were associated with the zeros of Bessel function to derive dispersion curve. I ran the forward modeling to test this procedure, leading to the conclusion that the zeros were robust compared with theoretical Bessel function, even when different levels of noises were added to SPAC function. After dispersion curve is obtained from microtremor coherency, different inversion techniques could then be applied to invert for shear wave velocity structure. I applied the SPAC method to two real world examples, Charleston, South Carolina and Manhattan, the New York City. For Charleston, shallow subsurface shear wave velocity is critical information in the context of earthquake hazard risk assessment and mitigation. I compared the shear wave velocity structures estimated from SPAC method with previous results from borehole SCPT and ReMi. Generally, SPAC correlates well with SCPT and ReMi result. In Manhattan, the estimated depths of bedrock from SPAC method are consistent with the expected bedrock depth based on previous geological information.

In summary, the experiments in Charleston and Manhattan show that SPAC method of analyzing microtermor provides an attracted way to characterize shallow shear wave velocity in urban areas. The experiment can be implemented effectively in cities without the need of drilling or active sources. The Vs estimation from SPAC is consistent with that from other techniques.

Reference

1. Aki, K., (1957), Space and time spectra of stationary stochastic waves, with special reference to microtremors*: Bulletin of the Earthquake Research Institute*, **35**, 415–456.
2. Aki, K., (1965), A note on the use of microseisms in determining the shallow structures of the earth's crust: *Geophysics*, **30**, 665–666.
3. Aki and Richards, (2002), Quantitative Seismology (second ed.), University Science Books, Sausalito, CA
4. Arai, H. Tokimatsu, K., (2004). S-Wave Velocity Profiling by Inversion of Microtremor H/V Spectrum, *Bull. Seism. Soc. Ame*, **94**, 53–63
5. Asten, M. W., (1976), The use of microseisms in geophysical exploration: Ph.D. thesis, Macquarie University
6. Asten, MW, and Dhu, T., (2004), Site response in the Botany area, Sydney, using microtremor array methods and equivalent linear site response modelling . Australian Earthquake Engineering in the New Millennium, Proceedings of a conference of the Australian Earthquake Engineering Soc., Mt Gambier South Australia, Paper 33.
7. Asten, M.W., and Boore, D.M., (2005), Blind comparisons of shear-wave velocities at closely spaced sites in San Jose, California: U.S. Geological Survey Open-File Report 2005-1169
8. Asten, M.W., (2006). On bias and noise in passive seismic data from finite circular array data processed using SPAC methods. *Geophysics*, **71**(6): V153 - V162.
9. Bakun, W.H., and M.G. Hopper (2004). Magnitudes and locations of the 1811-1812 New Madrid, Missouri and the 1886 Charleston, South Carolina earthquakes, *Bull. Seism. Soc. Amer*. **94**, 64-75.
10. Bard, P.-Y., (1998), Microtremor measurements, a tool for site effect estimation?, State-of-the-art paper: 2nd International Symposium on the Effects of Surface Geology on Seismic Motion, 3, 1251–1279.
11. Baskerville, C. A. (1994), Bedrock and engineering geologic maps of New York County and parts of Kings and Queens counties, New York, and parts of Bergen and Hudson counties, New Jersey, U. S. Geol. Surv. Misc. Invest. Ser., MAP I-2306.
12. Benuska, L., (1990). Loma Prieta Earthquake Reconnaissance Report. Earthquake Spectra, EERI, Supplement to vol. 6, May

13. Boore, D. M., W. B. Joyner, and T. E. Fumal (1997). Equations for estimating horizontal response spectra and peak acceleration from Western North American earthquakes: a summary of recent work, *Seism. Res. Lett*. **68**, 128–153.
14. Boore, D. M. (2006). Determining subsurface shear-wave velocities: A review, in Proceedings Third International Symposium on the Effects of Surface Geology on Seismic Motion, Grenoble, France, 30 August - 1 September 2006, Paper Number:103
15. Building Seismic Safety Council (BSSC) (2001). NEHRP recommended provisions for seismic regulations for new buildings and other structures, 2000 Edition, Part 1: Provisions, prepared by the Building Seismic Safety Council for the Federal Emergency Management Agency (Report FEMA 368), Washington, D.C.]).
16. Capon, J., (1969), High resolution frequency-wavenumber analysis: Proceedings of the IEEE, 57, 1408–1418.
17. Chapman, M. C., Martin, D. R., Olgun, C. G., and Beale, J. N. (2006). Site-response models for Charleston, South Carolina, and vicinity developed from shallow geotechnical investigations, *Bull. Seism. Soc. Amer*. **96**, 467-489
18. Charlie, W. A., G. T. Jirak, and D. O. Doehring (1985). Seismic analysis of Horse Creek Dam, Hudson, Colorado, in Proc. Conf. on Measurement and Use of Shear Wave Velocity for Evaluating Dynamic Soil Properties, Denver, Colorado, 1 May 1985, R. D. Woods, (Editor), American Society of Civil Engineers, New York.
19. Chouet, B., De Luca, G., Milana, G., Dawson, P., Martini, M., and Scarpa, R. (1998). Shallow velocity structure of Stromboli Volcano, Italy, derived from small aperture array measurements of Strombolian tremor. *Bull. Seism.Soc. Am.*, **88**, 653-666
20. Côté, R. (2006). City of Heroes: The Great Charleston Earthquake of 1886, Corinthian Books, Mt. Pleasant, South Carolina, 556 pp
21. Dobry, R., R. D. Borcherdt, C. B. Crouse, I. M. Idriss, W. B. Joyner, G. R. Martin, M. S. Power, E. E. Rinne, and R. B. Seed (2000). New site coefficients and site classification system used in recent building seismic code provisions, *Earthquake Spectra* **16**, 41–67.
22. Ekström, G., G. A. Abers, S. C. Webb, (2009). Determination of surface-wave phase velocities across USArray from noise and Aki's spectra formulation, *Geophys. Res. Lett.*, **36**, L18301.
23. Graves, R. W. (1998). Three-dimensional finite-difference modeling of the San Andreas Fault: source parameterization and ground-motion levels, *Bull. Seism. Soc. Am*. **88**, 881–897.

24. Hartzell, S., D. Carver, T. Seiji, K. Kudo, and R. Herrmann, (2005), Shallow shear-wave velocity measurements in the Santa ClaraValley, Comparison of spatial autocorrelation (SPAC) and frequency wavenumber (FK) methods, in M. W. Asten and D. M. Boore, eds., Blind comparisons of shearwave velocities at closely spaced sites in San Jose, California: U. S. Geological Survey Open-File Report 2005-1169.
25. Henstridge, J. D., (1979). A signal processing method for circular arrays: *Geophysics*, **44**, 179–184.
26. Herrmann, R. B. (2002). Computer programs in seismology, version 3.25: Saint Louis University, Saint Louis, Missouri
27. Jaumé, S. C. (2006). Shear wave velocity profiles via seismic cone penetration test and refraction microtremor techniques at ANSS strong motion sites in Charleston, South Carolina, *Seism. Res. Lett*. **77**, 771-779
28. Jaumé, S. C., and Levine, N. S. (2008). Shallow Shear Wave Velocity Structure of the Charleston Historical District, South Carolina: Comparison of Surficial Methods and Borehole Results, Final Rpt. USGS Award Number 05HQGR0072, 17 pp.
29. Johnston, A. C. (1996). Seismic moment assessment of earthquakes in stable continental regions, III. New Madrid 1811–1812, Charleston 1886, and Lisbon 1755, *Geophys. J. Int.* **126**, 314–344
30. Kind, F., D. Fah, and D. Giardini, (2005), Array measurements of S-wave velocities from ambient vibrations: *Geophys. J. Int*. **160**, 114–126
31. Kramer, S. L. (1996). Geotechnical Earthquake Engineering, Prentice-Hall,Upper Saddle River, New Jersey.
32. Kudo, K., Kanno, T., Okada, H., Ozel, O., Erdik, M., Sasatani, T., Higashi, S., Takahashi, M., and Yoshida, K., (2002), Site-specific issues for strong ground motions during the Kocaeli, Turkey, earthquake of 17 August 1999, as inferred from array observations of microtremors and aftershocks: *Bull. Seism. Soc. Am,* **92**, 448- 465.
33. Lacoss, R. T., E. J. Kelly, and M. N. Toksoz, (1969), Estimation of seismic noise structure using arrays: *Geophysics*, **34**, 21–38.
34. Liu, H., D. M. Boore, W. B. Joyner, D. H. Oppenheimer, R. E. Warrick, W. Zhang, J.C.Hamilton, and L.T. Brown, (2000), Comparison of phase velocities from array measurements of Rayleigh waves associated with microtremor and results calculated from borehole shear-wave velocity profiles: *Bull. Seism. Soc. Am*, **90**, 666–678.
35. Louie, J.N. (2001). Faster, better: Shear-wave velocity to 100 meters depth from refraction microtremor arrays, *Bull. Seism. Soc. Am*. **91**, 347—364.

36. McMechan, G. A., and M. J. Yedlin, (1981), Analysis of dispersive waves by wavefield transformation: *Geophysics*, **46**, 869–874
37. Nakamura,Y., (1989), Amethod for dynamic characteristics estimation of subsurface using microtremors on the ground surface: *Quarterly reports of the RailwayTechnical Research InstituteTokyo*, **30**, 25–33.
38. Nazarian, S., Stokoe,K. H., II, and Hudson,W. R., (1983), Use of spectral analysis of surface waves method for determination of moduli and thicknesses of pavement systems: Transport. Res. Record, 930, 38–45.
39. NEHRP 1997. NEHRP Recommended Provisions for Seismic Regulations for New Buildings and Other Structures, Part 1: Provisions, Building Seismic Safety Council, Washington, D. C.] ICBO 1997 [ICBO (1997). 1997 Uniform Building Code, Vol. 2, International Conference of Building Officials, Whittier, California.
40. Nogoshi, M., and T. Igarashi, (1971), On the amplitude characteristics of microtremor, Part II: *Journal of the Seismological Society of Japan*, **24**, 26–40.
41. Ohrnberger, M., F. Scherbaum, F. Krüger, R. Pelzing, and S.-K. Reamer, (2004), How good are shear wave velocity models obtained from inversion of ambient vibrations in the Lower Rhine Embayment _N.W. Germany?: Bollettino di GeofisicaTeorica edApplicata, 45, 215–232.
42. Okada, H., (2003), The microtremor survey method, SEG of Japan, K. Suto, trans: Geophysical Monograph Series 12, SEG.
43. Park, C.B., Miller, R.D., and Xia, J., (1999), Multichannel analysis of surface waves (MASW); *Geophysics*, **64**, 800-808
44. Petersen, Mark D., Frankel, Arthur D., Harmsen, Stephen C., Mueller, Charles S., Haller, Kathleen M., Wheeler, Russell L., Wesson, Robert L., Zeng, Yuehua, Boyd, Oliver S., Perkins, David M., Luco, Nicolas, Field, Edward H., Wills, Chris J., and Rukstales, Kenneth S., (2008). Documentation for the 2008 Update of the United States National Seismic Hazard Maps: U.S. Geological Survey Open-File Report 2008–1128, 61 p.
45. Robertson, P. K., R. G. Campanella, D. Gillespie, and A. Rice (1986). Seismic CPT to measure in situ shear wave velocity. *Journal of Geotechnical Engineering* **112**, 791–803.
46. Robertson, P.K., and Fear, C.E. (1995). "Liquefaction of sands and its evaluation.", Proceedings of the 1st International Conference on Earthquake Geotechnical Engineering, Tokyo

47. Scherbaum, F., K.-G. Hinzen, and M. Ohrnberger, (2003), Determination of shallow shear wave velocity profiles in the Cologne, Germany area using ambient vibrations: *Geophys. J. Int*. **152**, 597–612.
48. Seed, H. B. and Schnabel, P. B., (1972). Soil and Geological Effects on Site Response During Earthquakes. Proc. of First International Conf. on Microzonation for Safer Construction – Research and Application, vol. I, pp 61-74
49. Seed, H. B., Romo, M. P., Sun, J. I., Jaime, A., and Lysmer, J., (1988). The Mexico earthquake of September 19, 1985-Relationships between soil conditions and earthquake ground motions. *Earthquake Spectra*, EERI, Vol. 4, No. 4, pp. 687-729
50. Stephenson, W. J. , Hartzell, S. , Frankel, A. D. , Asten, M. , Carver, D. L. , and W. Y. Kim (2009). Site characterization for urban seismic hazards in lower Manhattan, New York City, from microtremor array analysis, *Geophys. Res. Lett*. **36**, L03301, doi: 10.1029/2008GL036444.
51. Stokoe, K. H. II, and S. Nazarian (1985). Use of Rayleigh waves in liquefaction studies, in Proc. Conf. on Measurement and Use of Shear Wave Velocity for Evaluating Dynamic Soil Properties, Denver, Colorado, 1 May 1985, R. D. Woods, (Editors), American Society of Civil Engineers, New York.
52. Stokoe, K. H., II, Wright, G. W., James, A. B., and Jose, M. R., (1994), Characterization of geotechnical sites by SASW method, inWoods, R. D., Ed., Geophysical characterization of sites: Oxford Publ.
53. Tada, T., Cho, I. and Shinozaki, Y. (2007). Beyond the SPAC method: Exploiting the Wealth of Circular-Array Methods for Microtremor Exploration, *Bull. Seism. Soc. Am.*, **97**, 2080-2095
54. Tada, T., Cho, I. and Shinozaki, Y. (2009). New Circular-Array Microtremor Techniques to Infer Love-Wave Phase Velocities. *Bull. Seismol. Soc. Am.*, **99**(5): 2912 - 2926.
55. Talwani, P., and W. T. Schaeffer (2001). Recurrence rates of large earthquakes in the South Carolina coastal plain based on paleoliquefaction data, *J. Geophys. Res.* **106**, 6621-6642.
56. Thorson, J. R., and J. F. Claerbout (1985). Velocity-stack and slant-stack stochastic inversion, *Geophysics* **50**, 2727–2741.
57. Warren, L.M., J.A. Snoke, and D.E. James, (2008). S-wave velocity structure beneath the High Lava Plains, Oregon, from Rayleigh-wave dispersion inversion, *Earth Planet. Sci. Lett.*, **274**, 121-131.

58. Wathelet, M., D. Jongmans, and M. Ohrnberger, (2004), Surface-wave inversion using a direct search algorithm and its application to ambient vibration measurements: *Near Surface Geophysics*, **2**, 211–222.
59. Wills, C. J., M. Petersen, W. A. Bryant, M. Reichle, G. J. Saucedo, S. Tan, G. Taylor, and J. Treiman (2000). A site-conditions map for California based on geology and shear-wave velocity, *Bull. Seism. Soc. Am.* **90**, S187–S208.
60. Xia, J., Miller, R.D., and Park, C.B., (1999), Estimation of near-surface shear-wave velocity by inversion of Rayleigh waves, *Geophysics*, **64**(3), 691-700

Chapter 4. Shear wave velocity inversion from surface wave dispersion

4.1 Inverse problem overview

An important task faced by geophysicists and seismologist is to make inference and extract information about the Earth interior structure. Most of the time, it is difficult to observe directly and acquire information, including physical and chemical properties, temperature, composition, seismic velocity, etc. regarding to the Earth deep interior, because it is usually hard or even impossible for scientists to get into the inside of the Earth to measure these data. Therefore, geophysicists usually make indirect observation at the surface of the Earth, then build physical models and make inference on the Earth internal structure by solving models' unknowns. Mathematically, this process of inferring model parameters from observations is called inverse problem. In geophysics, it is called geophysical inverse problem.

Geophysical inverse problems are usually the oppose process to the classic forward problem (Figure 4.1). Scientists, physicists and mathematicians use fundamental physical models to describe and characterize the real world. The model can be described abstractly with a set of parameters **m**, and the "forward problem" is formulated as calculating data **d** from model **m** through a physical model. Mathematically, this process can be represented as: $G(\boldsymbol{m}) = \boldsymbol{d}$, where G is a function describing the physical model that relates the model **m** with data **d**. The "inverse problem", on the contrary, is given a set of measurement,

data **d**, and the physical model, the function **G**, to infer the model parameters **m**. Different literatures use different terminologies. Mathematicians usually refer to $G(\boldsymbol{m}) = \boldsymbol{d}$ as the "mathematical model" and to **m** as the "parameters". Scientists call **G** the "forward operator" and **m** the "model". We will use scientists' term thereafter, refer to **m** as model, or more specifically the Earth model, and refer to the relation $G(\boldsymbol{m}) = \boldsymbol{d}$ as the "physical model" (Aster et al 2004).

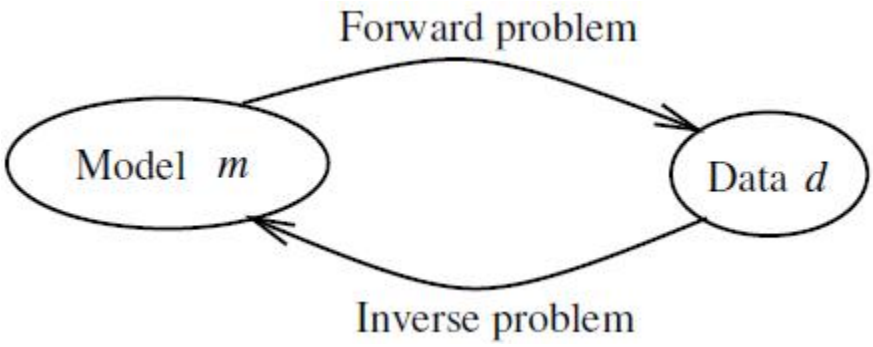

Figure 4.1: Forward & Inverse problem. (Sneider & Trampert, 1999).

The forward problem of finding **d** given **m**, according to $G(\boldsymbol{m}) = \boldsymbol{d}$, usually involves computing **G(m)** through some standard mathematical techniques, including ordinary differential equation (ODE), partial differential equation (PDE), evaluating integral, etc. The inverse problem, on the contrary, is solving **m** given **d**, which is usually not an easy task (Aster et al 2004). The inverse problem is generally more difficult to solve than its forward counterpart because most of the complicated functions do not have analytical representations of the inverse function, G^{-1}.

When dealing with the Earth model, we usually want to use a set of finite number of parameters to characterize the physical model, **m**. And the data **d** we observed which needed to be processed on the computer could only be discrete data points. In this case, both **m** and **d** are vectors and the problem of estimating model **m** from data **d** is called **discrete inverse problem** or **parameter estimation problem**, and the relationship becomes a set of equations:

$$G(\boldsymbol{m}) = \boldsymbol{d}, \quad (4.1.1)$$

where **m** is n-element vector, and **d** is m-element vector.

Under certain circumstances, the relationship between model parameter **m** and data **d** is linear, or could be linearized, the set of equation in (4.1.1) could be written in matrix form:

$$G(\boldsymbol{m}) = \boldsymbol{Gm} = \boldsymbol{d} \quad (4.1.2)$$

Where **m** is $n \times 1$ vector, **d** is $m \times 1$ vector, and G is $m \times n$ matrix.

Solving **m** is now in the context of matrix algebra and standard linear algebra techniques could be applied. This type of problem is called **discrete linear inverse problem**. I will discuss the techniques for solving discrete linear inverse problems in section 4.3.

Generally, the relationship between **m** and **d** is not a simple linear, but a more complicated non-linear function, and the problem of inverting for **m** from $G(\boldsymbol{m}) = \boldsymbol{d}$ is called **non-linear inverse problem**. There is usually no exact analytical solution to the equation (4.1.1), because the nonlinearity often complicates the problem. Scientists have developed some advanced numerical techniques and algorithms to solve the non-linear inverse problems, I will discuss two of them, Monte Carlo and Simulated Annealing in section 4.4.

There are three basic but important questions to be considered when solving the inverse problem, which are the solution's existence, uniqueness, and stability.

- **Existence**. The model we build is always an abstraction of the real world. Therefore, sometimes the data we observed may not have models to fit in, because the physical model is incorrect, or too simple, or there are too much noise contained when we make observation. The first question to ask is whether the solution exists.

- **Uniqueness**. The forward problem of computing **d** from G(m) is always an one-to-one mapping, the opposite is not always the case. In other word, there may be more than one model **m** that could fit the data **d**, which cause the nonuniqueness of the solution. Appropriate evaluation of these models is then needed in order to choose the most reasonable ones.

- **Stability**. Since data **d** always contain noises, the problem could be written more precisely as,

  $\boldsymbol{d} = G(\boldsymbol{m_{true}}) + \boldsymbol{\eta}$, (4.1.3)

  where $\boldsymbol{m_{true}}$ is the true model, and η is all noises associated with the observation and/or measurements. The inverse problem of estimating $\boldsymbol{m_{true}}$ from data **d** could become extremely unstable meaning that even a small change in the measurement, i.e. $\boldsymbol{\eta}$, can result in an enormous change in the estimated model **m**. This is called **ill-posed** in the case of continuous inverse problem and **ill-conditioned** in the case of discrete inverse problem. We usually do not want the estimated model **m** to fluctuate wildly with even a small change in data. Additional constraints, or a process referred to **regularization**, are usually applied for ill-posed and/or ill-conditioned problem to make the solution stable.

4.2 Surface wave dispersion inversion for Vs

As discussed in Chapter 3, the dispersive feature of seismic surface wave, particular Rayleigh wave, makes it possible to obtain shear wave velocity structure in the Earth by interpreting Rayleigh wave dispersion curve. Theoretical studies of surface wave were first given by Thomson (1950) and Hanskell (1953), who formulated the problem and provide the method of forward calculation of surface wave dispersion curve using matrix techniques. The matrix method for surface wave is basically used to solve the eigenvalue problem of the system of differential equations. A dispersion function is constructed, which is an implicit function of frequency, phase velocity, thickness, elastic parameters

and damping of the layers. The dispersion curves are the roots, or eigenvalues, of the dispersion equations. This method of calculating dispersion curve is also known as **propagator matrix method**, since the motion-stress field is propagated through a stack of homogeneous layers over a homogeneous half-space (Aki & Richard 2002).

Seismologists usually model the Earth as homogeneous layered structure (Figure 4.2), with layer property (v_S, v_P, ρ, h) denoting shear wave velocity, compressional P-wave velocity, density and layer thickness respectively. Subscript i indicates the number of layer from 1 to n, including infinite half-space.

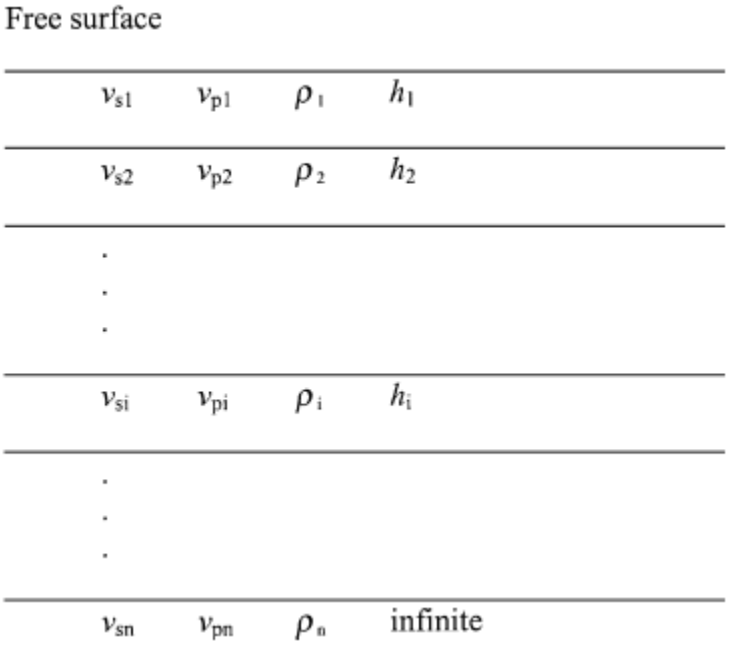

Figure 4.2: layered Earth model, $(\boldsymbol{v_S, v_P, \rho, h})$ denote Shear velocity, P wave velocity, density, and layer thickness for each layer i. (Xia et al 1999)

The matrix form of calculating Rayleigh-wave dispersion curve can be written as:

$$F\left(f_j, c_{Rj}, \boldsymbol{v_S, v_P, \rho, h}\right) = 0 \text{ , (j=1,2,…,m)} \quad (4.2.1)$$

Where F represents the nonlinear, implicit characteristic equation, f_j is the frequency in Hz; c_{Rj} is the Rayleigh-wave phase velocity to be determined at frequency f_j; bold case indicates layer vector; $\boldsymbol{v_S} = (v_{s1}, v_{s2}, \dots, v_{sn})^T$ is the S-wave velocity vector, with v_{si} being the shear-wave velocity of the ith layer; n is the number of layers; $\boldsymbol{v_P} = (v_{P1}, v_{P2}, \dots, v_{Pn})^T$ is the P-wave velocity vector with v_{Pi} being the P-wave velocity of the ith layer; $\boldsymbol{\rho} = (\rho_1, \rho_2, \dots, \rho_n)^T$ is the density vector; and $\boldsymbol{h} = (h_1, h_2, \dots, h_{n-1})^T$ is the thickness vector. Rayleigh-wave phase velocity c_{Rj} at the specific frequency f_j is determined by solving for the root of equation (4.2.1) given a set of model parameters, $(\boldsymbol{v_S}, \boldsymbol{v_P}, \boldsymbol{\rho}, \boldsymbol{h})$**.** The problem of determining elastic property $(\boldsymbol{v_S}, \boldsymbol{v_P}, \boldsymbol{\rho})$ for each layer given Rayleigh-wave phase velocity c_{Rj} for each frequency f_j is inverse problem.

Since the relationship between Rayleigh-wave phase velocity, c_{Rj} and layer's elastic property $(\boldsymbol{v_S}, \boldsymbol{v_P}, \boldsymbol{\rho})$ is highly nonlinear and implicit as represented by function F in equation (4.2.1), the inverse problem of determine shear wave velocity $\boldsymbol{v_S}$ from phase velocity c_{Rj} is not an easy task, either linearization of the equation (4.2.1) or advanced numerical techniques is needed for the inversion.

4.3 Linear Inversion

As discussed in section 4.1, the general inverse problem is to determine the model parameters **m** given observed data d using the relation, $G(\boldsymbol{m}) = \boldsymbol{d}$**.** Linear inversion lies the ground for more complicated inverse problem in that when the problem could be

written in matrix form, $\boldsymbol{Gm = d,}$ standard linear algebra techniques could be applied to solve the unknown **m**. Even when the problem is nonlinear, sometimes it can be **linearized** so that linear inversion techniques could be used. I will discuss the tools used to solve linear inversion problem first in this section, and then show how to solve nonlinear problem by linearization.

For discrete linear inverse problem, the data vector $\boldsymbol{d}$ is a $m \times 1$ vector indicating that there are total of m observation data points, the model is parameterized by n parameters as the $n \times 1$ vector $\boldsymbol{m}$. The relationship between model m and data d is formulated as

$$\boldsymbol{Gm = d} \quad (4.3.1)$$

where G is a $m \times n$ matrix.

When noise is considered, the formula could be written as

$$d = Gm_{true} + \eta \quad (4.3.2)$$

Where η is noise.

We always want to find the true model m_{true} or the closest model to true model, which could minimize the error term η and could best fit the data d.

Least-square method is a classic linear algebra technique to solve **m** in equation (4.3.1). The misfit of the residuals, $\boldsymbol{r = d - Gm,}$ measured in 2-norm, is minimized.

Menke (1989) and Tarantola (2005) both gave the least square solution to the discrete linear inverse problem:

$\widetilde{m} = (G^T G)^{-1} G^T d$, (4.3.3)

Where $\widetilde{m}$ is the least square solution, T denotes matrix transpose, -1 denotes matrix inverse.

Menke (1989) and Tarantola (2005) show that the above solution $\widetilde{m}$ minimize the 2-norm of the residual, $\|r\| = \|\boldsymbol{d} - \boldsymbol{Gm}\|$**,** where $\|\quad\|$denotes 2-norm.

[Ill-posed problem, regularization]

In order to get the least-square solution using equation (4.3.3), one important prerequisite is that the matrix $G^T G$ is invertible. In some cases, the matrix $G^T G$ is not invertible. The problem is **ill-posed** if the matrix $G^T G$ or GG^T is not invertible. Even if the inverse matrix exists, sometimes it is **ill-conditioned,** so even a small change in the data vector **d** will lead to a big change in the model estimation $\widetilde{\boldsymbol{m}}$. We usually expect the estimation model to be insensitive to small changes in the data. The **damped least-square method** introduced by Levenberg (1944) could overcome the ill-posed and ill-conditioned problem. Mathematically, the ill-posedness and ill-conditioning result from zero or close to zero of the singular values of matrix $G^T G$ (Snieder & Trampert 1999).

Recall that for the least-square method, we want to seek a solution which minimizes the 2-norm of the residuals, that is:

Min $\|\boldsymbol{d} - \boldsymbol{Gm}\|$, (4.3.4)

For damped least square method, we add a damping term to the function we want to minimize, that is,

Min $\|\boldsymbol{d} - \boldsymbol{Gm}\|^2 + \alpha^2\|\boldsymbol{m}\|^2$ (4.3.5)

Where $\alpha^2\|\boldsymbol{m}\|^2$ is the damping term, α is **damping factor**, or **regularization parameter**.

By solving (4.3.5), we actually comprise in finding a model that both fits the data reasonable well and the model size is not too large.

The damped least square solution to (4.3.5) given is by Levenberg (1944),

$\widetilde{m} = (G^T G + \alpha^2 I)^{-1} G^T d$ (4.3.6)

Where I is the identity matrix with diagonal elements 1, and others being zero.

Comparing the damped least square solution (4.3.6) with least square solution (4.3.5), it can be found that the effect of adding the damping factor α is to make the eigenvalues of $G^T G$ moved away from zero, thus the matrix $G^T G + \alpha^2 I$ is invertible.

[Linearized inverse, Iterative methods]

The discussion above is a summary of the methods used to solve discrete linear equation, $Gm = d$, where the data **d** are linear related with the model parameters **m** through matrix

G. For more complicated model, the relationship between model **m** and data **d** is not a simple linear function, but a more complicated non-linear function,

$G(m) = d.$ (4.3.7)

For this type of functions, one solution is to linearize the function G using Taylor's expansion so that a linear relationship between perturbations in the data and the perturbations in the model can be obtained (Sen & Stoffa, 1995).

Denote the observed data as $\boldsymbol{d_{obs}}$, a small perturbation to the model $\Delta\boldsymbol{m}$ is applied to the reference model $\boldsymbol{m_0}$, the data calculated from any model is denoted by synthetic data $\boldsymbol{d_{syn}}$, ,

That is,

$d_{obs} = G(m_0 + \Delta m),$ (4.3.8)

and

$d_{syn} = G(m_0)$, (4.3.9)

Using Taylor's series to expand (4.3.8) around the reference model $\boldsymbol{m_0}$, we obtain

$G(m_0 + \Delta m) = G(m_0) + \frac{\partial G(m_0)}{\partial m}\Big|_{m=m_0} \Delta m + second\ and\ high\ order\ terms.$ (4.3.10)

Ignoring the higher order terms and using equation (4.3.8) and (4.3.9), we have

$$d_{obs} = d_{syn} + \frac{\partial G(m_0)}{\partial m}\Big|_{m=m_0} \Delta m. \quad (4.3.11)$$

Or

$$\Delta d = J_0 \Delta m. \quad (4.3.12)$$

where $\Delta d = d_{obs} - d_{syn}$ is the data misfit, and J_0 is the sensitivity matrix, or partial derivatives matrix of the synthetic data with respect to the model parameters.

Equation (4.3.12) expresses the linear relationship between the perturbations in data Δd and the perturbations in the model parameters Δm (Sen & Stoffa 1995).

The idea of iterative inversion method is based upon the above derivation by Taylor's theorem. During each iteration, the model is updated by a small amount Δm, which is computed from the data misfit Δd. The iteration process continues until the data misfit Δd is small enough.

Denote the model at kth iteration as m^k, the local approximation around m^k using Taylor's theorem is:

$$G(m^k + \Delta m) \approx G(m^k) + J(m^k)\Delta m = d. \quad (4.3.13)$$

Where $J(m^k)$ is the partial derivative matrix, or Jacobian matrix,

$$J(m^k) = \begin{bmatrix} \frac{\partial G_1(m^k)}{\partial m_1} & \cdots & \frac{\partial G_1(m^k)}{\partial m_n} \\ \vdots & \ddots & \vdots \\ \frac{\partial G_m(m^k)}{\partial m_1} & \cdots & \frac{\partial G_m(m^k)}{\partial m_n} \end{bmatrix}. \quad (4.3.14)$$

Two widely used algorithms of iterative method for non-linear inversion are Gauss-Newton method (GN) and Levenberg-Marquardt (LM) method (Aster 2004).

For GN method, model update at the kth iteration Δm_k is obtained by solving normal equation,

$$J_k{}^T J_k \Delta m_k = J_k{}^T \Delta d_k. \quad (4.3.19)$$

Where J_k denote the Jacobian matrix $J(m^k)$ for model m^k, Δd_k denote data misfit $d_{obs} - G(m^k)$ with respect to model m^k.

It can be seen that the GN method would fail when $J_k{}^T J_k$ is singular.

LM method is developed to overcome this singularity problem. For LM, a damping term is added, and the normal equation to be solved becomes,

$$(J_k{}^T J_k + \lambda \boldsymbol{I}) \Delta m_k = J_k{}^T \Delta d_k. \quad (4.3.20)$$

Here λ is the damping factor, and I is identity matrix.

The LM method is very useful for solving geophysical inverse problem because matrix $J_k{}^T J_k$ is often singular thus not invertible.

The flow diagram of LM iterative algorithm is given as following,

****

Given observed data vector d_{obs}, and starting model m

Loop over iteration i=1,2,… for kth iteration

- $d_{syn} = G(m_k)$ synthetic data vector
- $\Delta d = d_{obs} - d_{syn}$ data residual
- If data residual is small enough, usually $\|\Delta d\| < \xi$, ξ is a very small number.
- Then exit loop.
- Else continue to next step
- $J_k = \frac{\partial G(m_k)}{\partial m}\Big|_{m=m_k}$ Jacobian matrix
- $(J_k{}^T J_k + \lambda \boldsymbol{I})\Delta m_k = J_k{}^T \Delta d$ solve for model update Δm_k
- Update model: $m_{k+1} = m_k + \Delta m_k$

End loop

****

The computation of partial derivative matrix, Jacobian matrix is a key step in order for the linear iterative inversion to succeed. Rayleigh wave dispersion curve is known to be a function of P-wave velocity (Vp), S-wave velocity (Vs), density and layer thickness (equation 4.2.1). Through analyzing the Jacobian matrix, Xia (Xia et al. 1999) shows that S-wave velocity is the dominant influence on fundamental model Rayleigh wave dispersion data. So in practice, we can assign the Vp and density as known constants, fix layer thickness, and only invert for Vs through calculating the Jacobian matrix as the partial derivative of dispersion with respect to Vs. I used the damped weighted least square algorithm based on the above iterative LM method (Herrmann 2001) to do the linear inversion of Shear wave velocity from dispersion curve obtained by SPAC method at Charleston, South Carolina (Chapter 3). For the linear inversion, I fixed the Vp to Vs velocity ratio, density and layer thickness during the iteration, and only inverted for the Vs. The Vs model with 5 layers of the same layer thickness was chosen. I inverted for the upper 30m Vs structure. The results for Waterfront park site are given as follows.

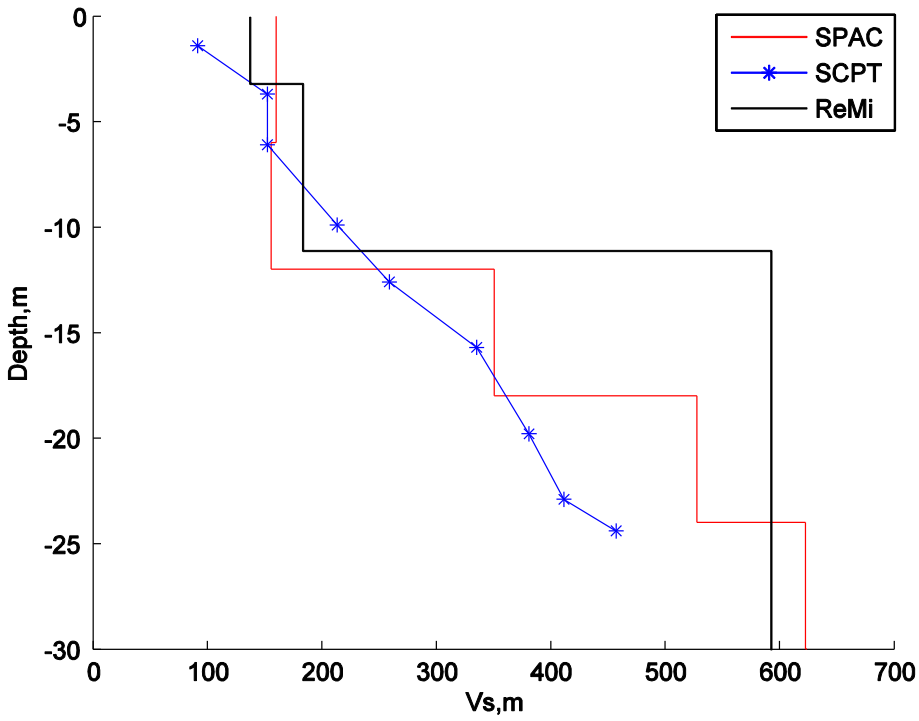

Figure 4.3: Waterfront park site (WFP). Inverted Vs structure from SPAC using linear inversion (red line), compared with Vs obtained by borehole SCPT (blue star) and Refraction Microtremor (black line) method.

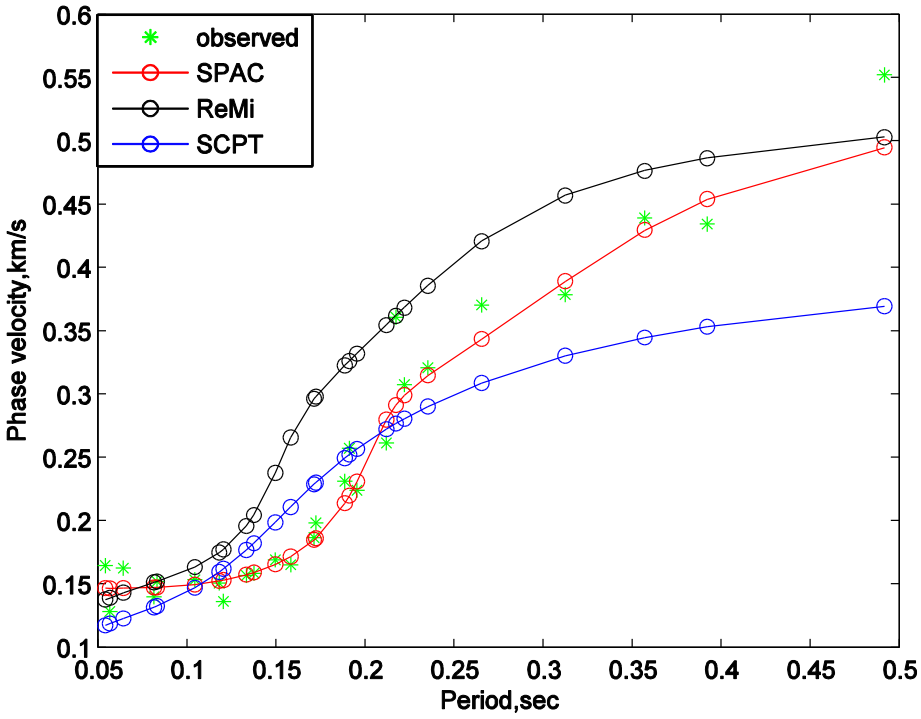

Figure 4.4: WFP site. Comparison of dispersion curves. Observed dispersion data (green star), and forward calculated dispersion curves from different models based on Figure 4.3. Red circle: calculated dispersion from Vs obtained using linear inversion of SPAC. Black: calculated dispersion from Vs obtained using ReMi, Blue: calculated dispersion from Vs obtained through SCPT.

The linear inversion result is compared with Vs models obtained by using borehole SCPT and Refraction Microtremor (ReMi) method in Figure 4.3. The linear inverted Vs model correlates well with those Vs models from SCPT and ReMi. A general velocity increasing trend can be seen in all three models. I forward calculate the dispersion curves, using Vs model obtained from linear inversion, SCPT, and ReMi methods. The dispersion curves that are compared with observed dispersion data are plotted in Figure 4.4. It is shown that the linear inversion resulting from SPAC gives the best fit of the observation (Red circle in Figure 4.4).

It is known that how the model is parameterized has an effect on the final inversion result. In the Vs inverse problem, the number of layers in the model may influence the inverted Vs structure. I also tried to invert for the 10 and 15 layers model.

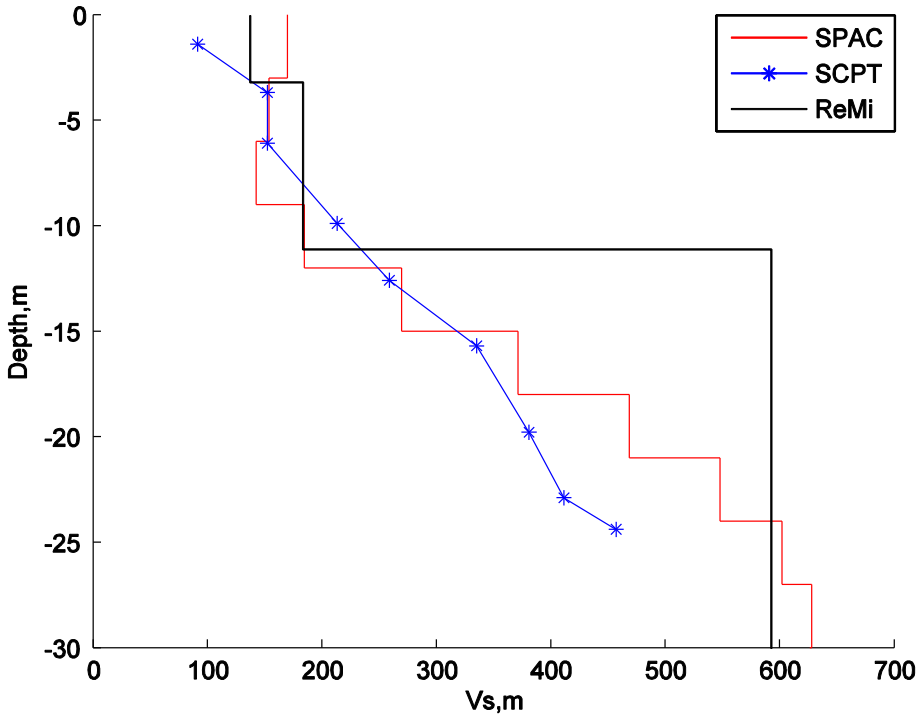

Figure 4.5: WFP site. Linear inverted Vs from SPAC (red line) for 10 layers, compared with Vs obtained by SCPT (blue star) and ReMi (black line) method.

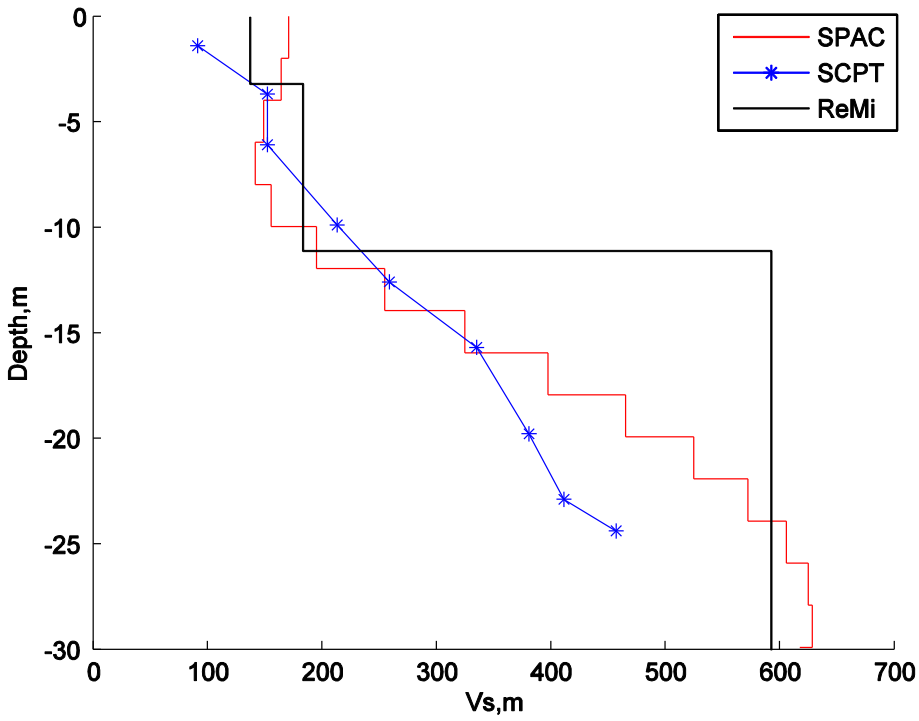

Figure 4.6: WFP site. Linear inverted Vs from SPAC (red line) for 15 layers, compared with Vs obtained by SCPT (blue star) and ReMi (black line) method.

I forward calculated the dispersion curve from the 5, 10 and 15 layer Vs model obtained by the linear inversion. The dispersion curves are plotted in Figure 4.7.

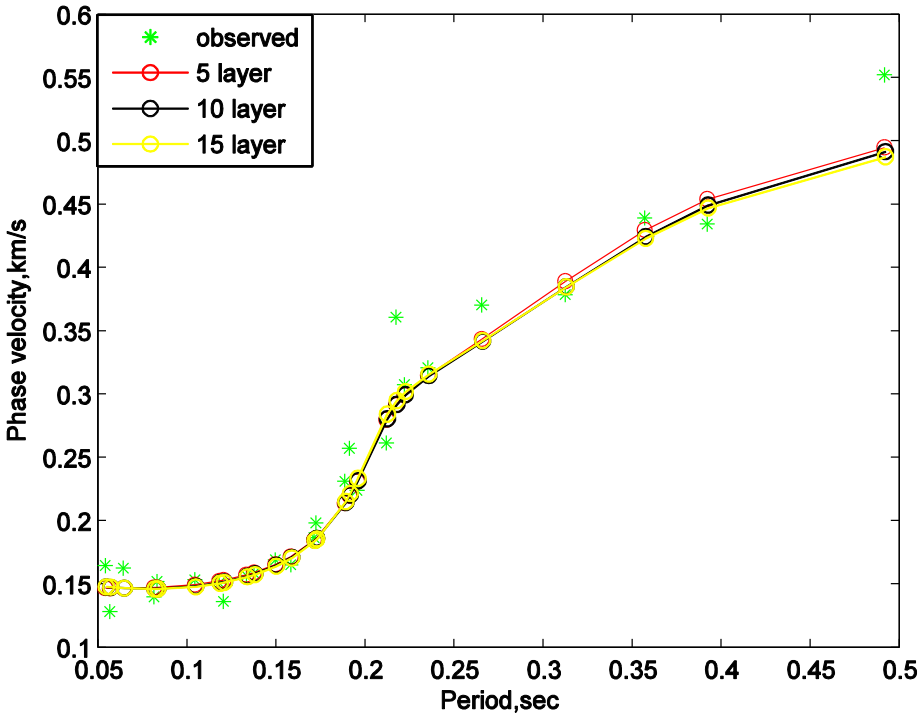

Figure 4.7: WFP site. Comparison of forward calculated dispersion curves for different number of layers Vs model. Red circle: 5 layer model (Figure 4.3), Black circle: 10 layer model (Figure 4.5), Yellow circle: 15 layer model (Figure 4.6). Green star: observed dispersion data.

The forward calculated dispersion curves using the 5, 10 and 15 layer Vs model show that these three models fit observation equally well. The number of layers in this case does not affect the result much, because the dispersion data is a normal dispersion, which means that the phase velocity increases with period and shear wave velocity increases with depth. In this case, the 5-layer model is sufficient to characterize the subsurface structure for WFP site.

The linear inversion results for Maybank bridge site (MBB) are given in Figure 4.8

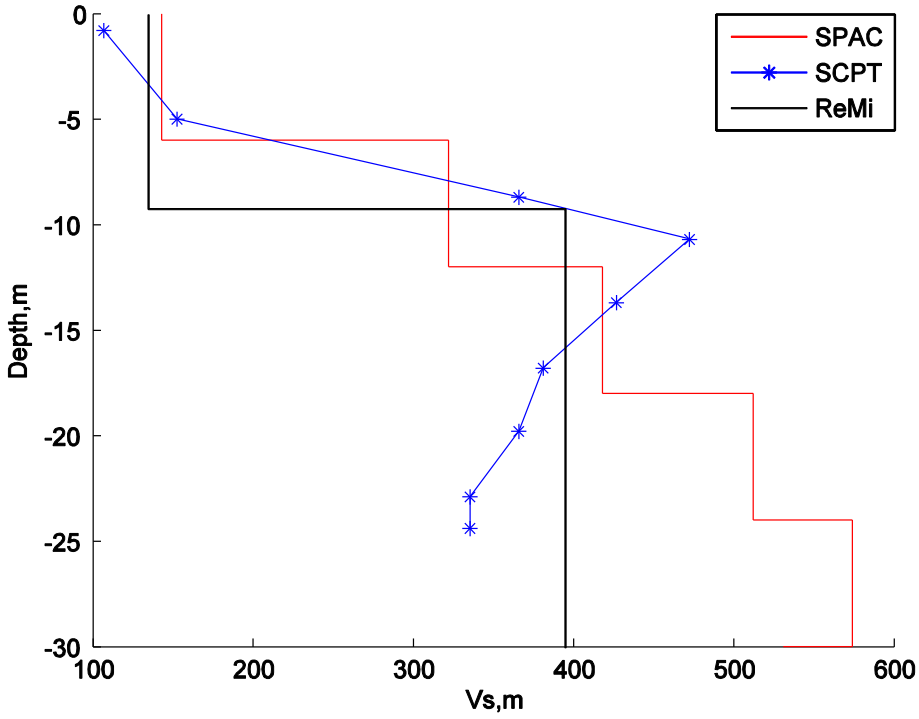

Figure 4.8: Maybank bridge site (MBB). Inverted Vs structure from SPAC using linear inversion (red line), compared with Vs obtained by borehole SCPT (blue star) and Refraction Microtremor (black line) method.

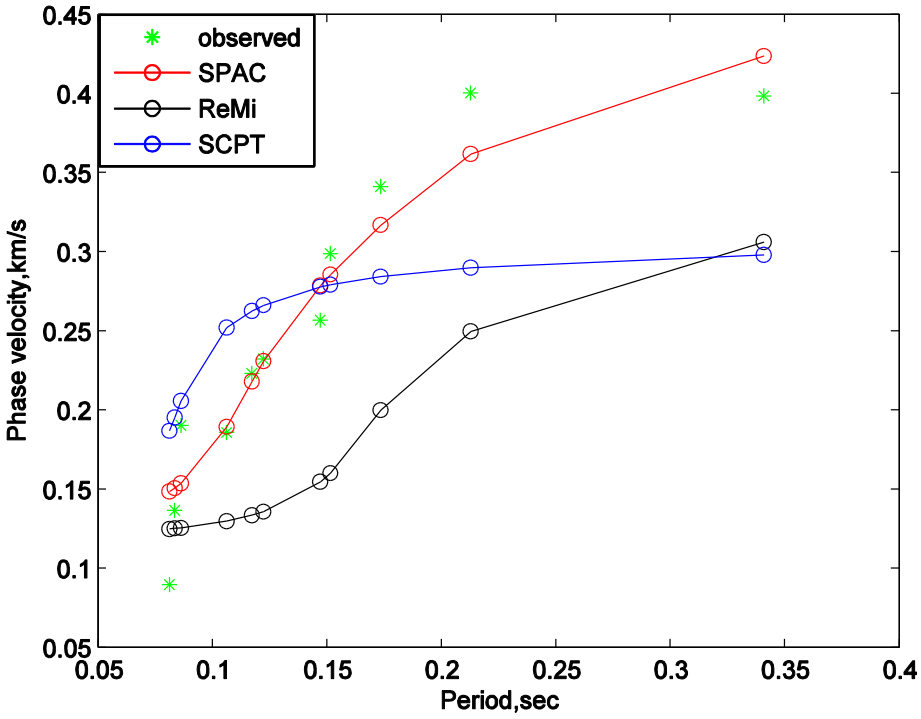

Figure 4.9: MBB site. Comparison of dispersion curves. Observed dispersion data (green star), and forward calculated dispersion curves from different models based on Figure 4.8. Red circle: calculated dispersion from Vs obtained using linear inversion of SPAC. Black: calculated dispersion from Vs obtained using ReMi, Blue: calculated dispersion from Vs obtained through SCPT.

In Figure 4.9, the forward calculate dispersion curve using the Vs model from the linear inversion fits the observation well compared with Vs models from ReMi and SCPT. However, in Figure 4.8, Vs models from both ReMi and SCPT indicate that there is a velocity discontinuity at around depth 10m. The linear inversion result does not capture this irregularity. Taking into account the velocity discontinuity, I forced a sharp velocity change at around depth 10m and redid the linear inversion. I also inverted for the 10 and 15 layer Vs model.

The results after forcing a velocity discontinuity at around depth 10m for 5, 10 and 15 layer models are given below:

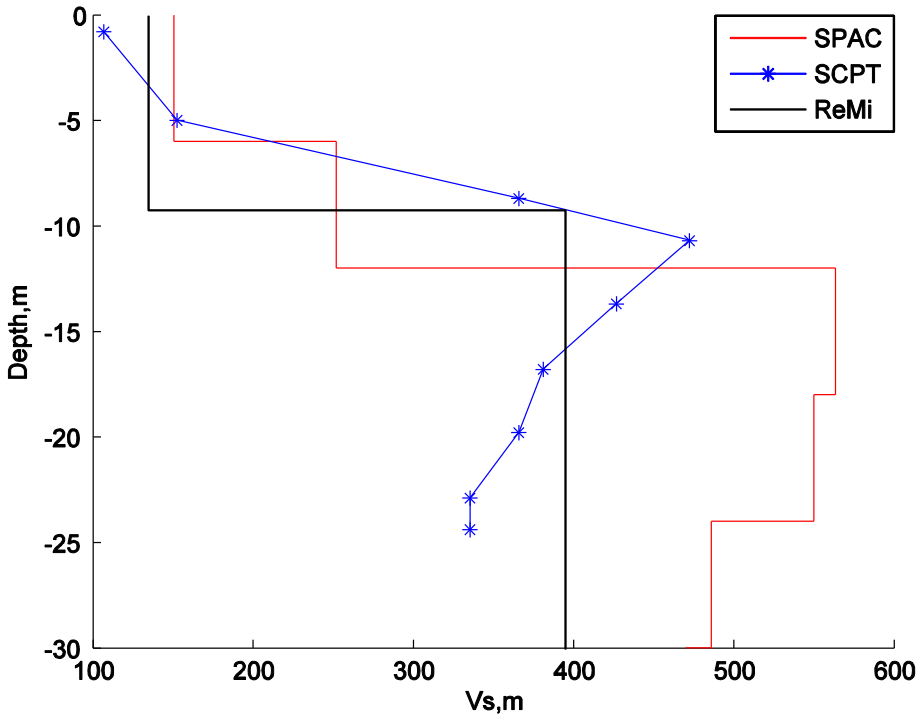

Figure 4.10: MBB site. Inverted 5-layer Vs structure from SPAC using linear inversion, with a forcing velocity discontinuity at 3rd layer (12m) (red line), compared with Vs obtained by SCPT (blue star) and ReMi (black line) method.

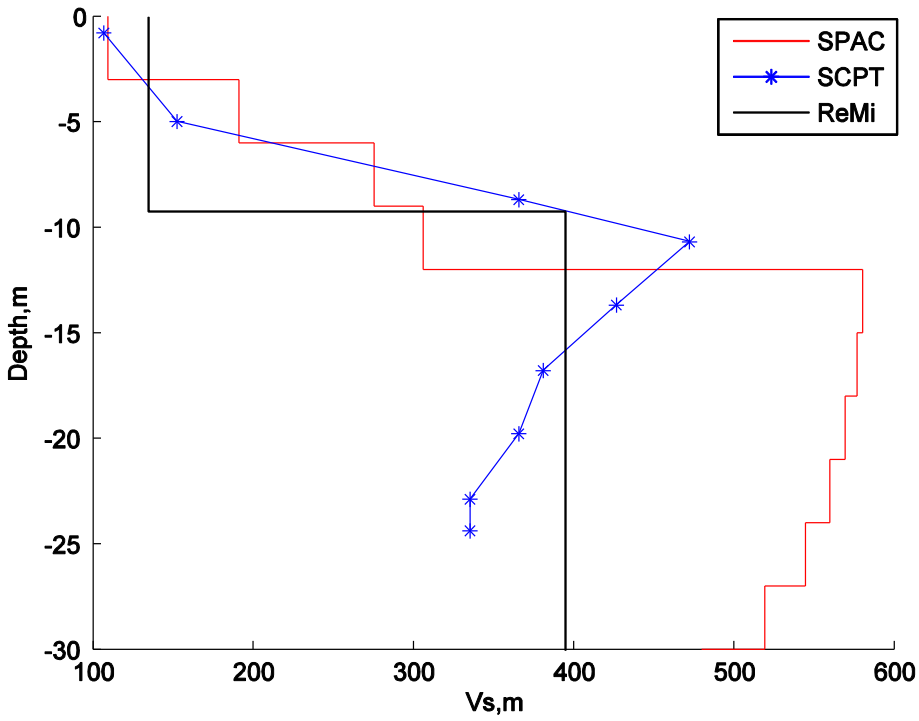

Figure 4.11: MBB site. Inverted 10-layer Vs structure from SPAC using linear inversion, with a forcing velocity discontinuity at 5th layer (12m) (red line), compared with Vs obtained by SCPT (blue star) and ReMi (black line) method.

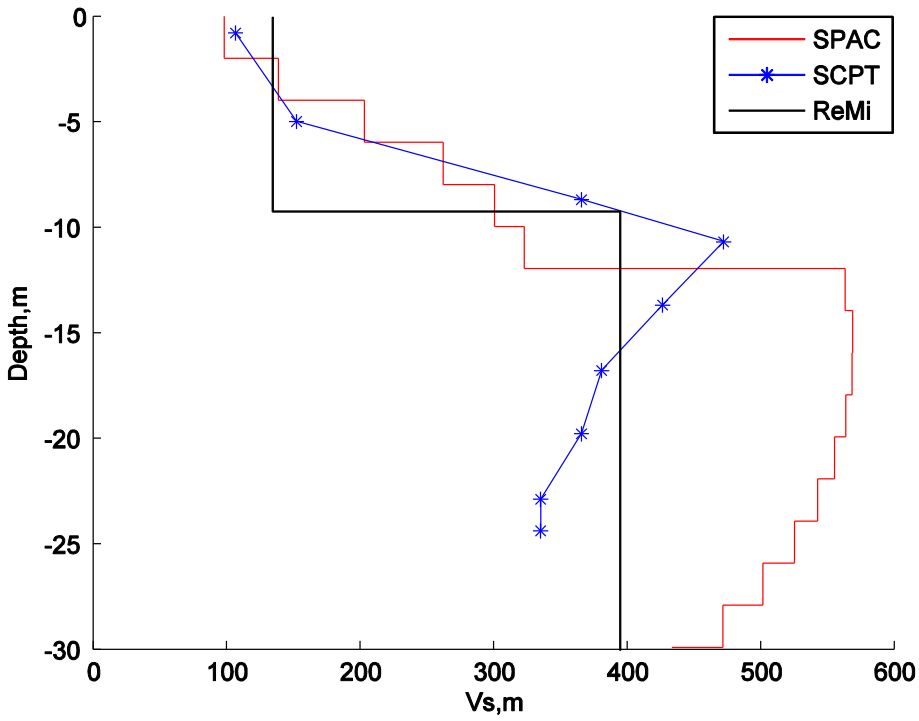

Figure 4.12: MBB site. Inverted 15-layer Vs structure from SPAC using linear inversion, with a forcing velocity discontinuity at 7th layer (12m) (red line), compared with Vs obtained by SCPT (blue star) and ReMi (black line) method.

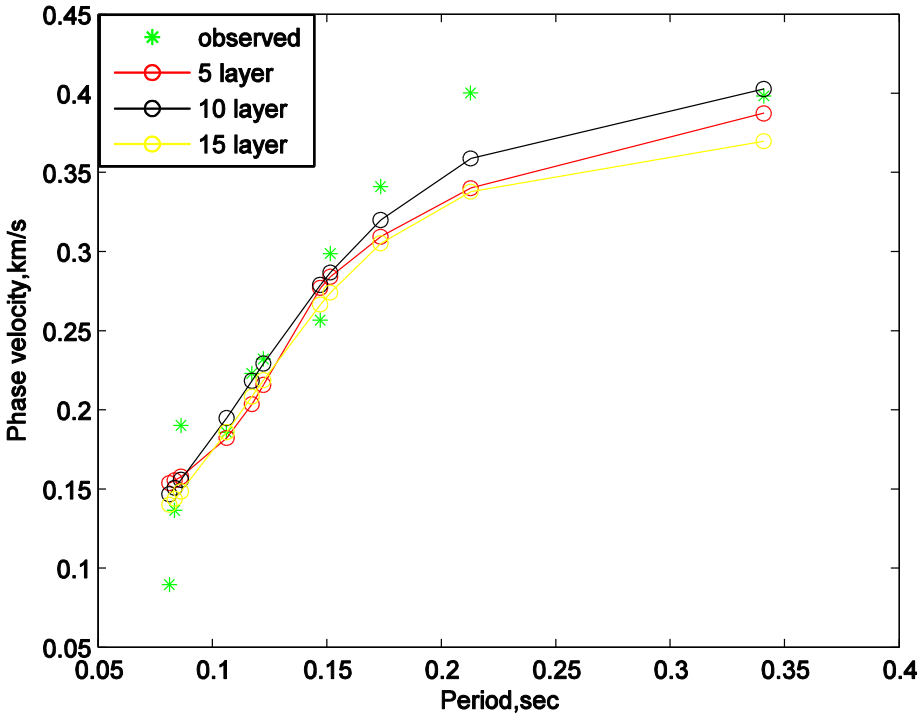

Figure 4.13: MBB site. Comparison of forward calculated dispersion curves for different number of layers Vs model. Red circle: 5 layer model (Figure 4.10), Black circle: 10 layer model (Figure 4.11), Yellow circle: 15 layer model (Figure 4.12). Green star: observed dispersion data.

Comparing with the observed dispersion, the forward calculated dispersion curves using the 5, 10 and 15 layer Vs models with a forced velocity discontinuity at depth 12m indicate a good fit (Figure 4.13). Figure 4.10 to Figure 4.12 show that the inverted Vs models correlate well with ReMi and SCPT for upper 10m depth as well as the sharp velocity jump at around 10-12m. The shear wave velocity below depth 12m is slightly higher for linear inverted models than for SCPT and ReMi models.

The linear inversion results for Trident Research Center (TRC) site are given in Figure 4.14

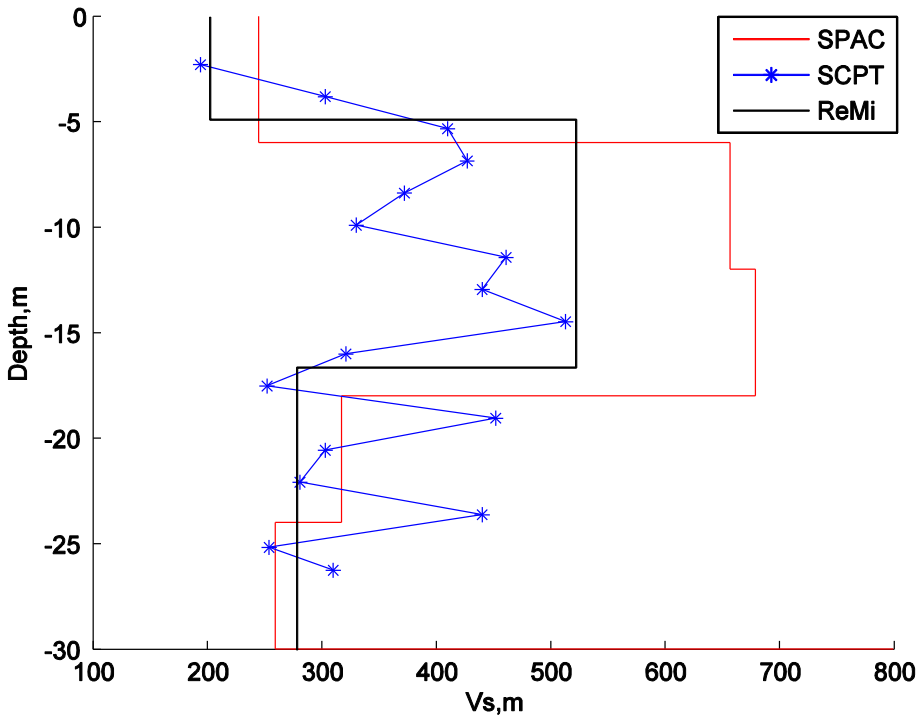

Figure 4.14: Trident Research Center (TRC) site. Inverted Vs structure from SPAC using linear inversion (red line), compared with Vs obtained by SCPT (blue star) and ReMi (black line) method.

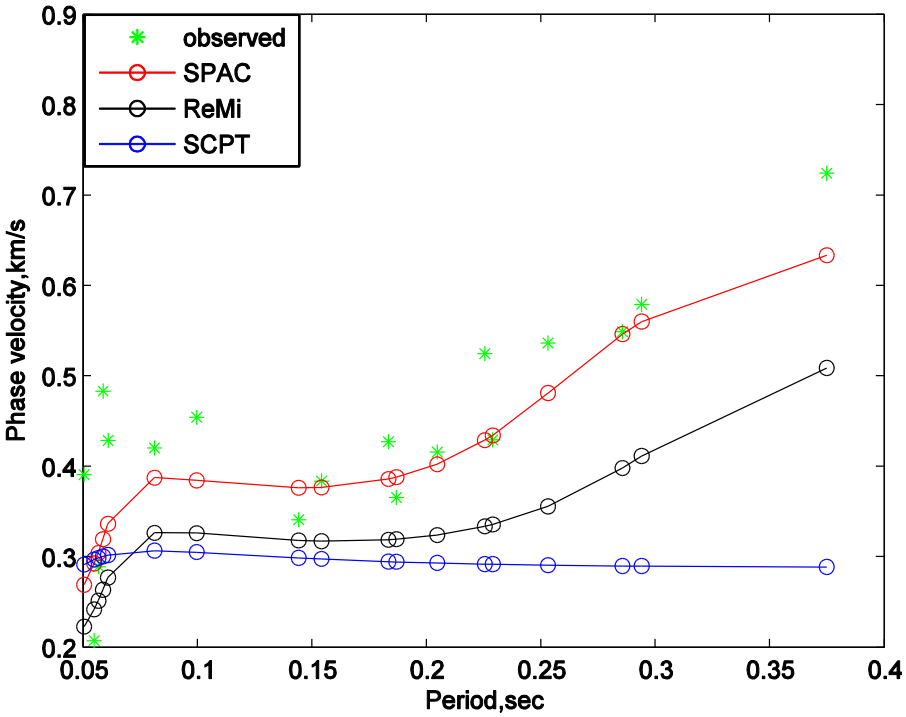

Figure 4.15: TRC site. Observed dispersion data (green star), and forward calculated dispersion from different models based on Figure 4.14. Red: calculate from Vs obtained using linear inversion of SPAC. Black: calculated from Vs obtained using ReMi, Blue: calculated from Vs that obtained from SCPT.

The Vs from linear inversion correlate well with the ReMi model. A low velocity zone in the depth range 17-30m can be seen in both ReMi and SPAC model (Figure 4.14). The SCPT measurements are scattered for TRC site. The sampling of SCPT is dense compared with the other two sites, and thus the highly heterogeneous subsurface might be the reason for this scattering. But generally, SCPT data falls within the range of the inverted Vs model. Forward calculated dispersion curves show that the linear inverted Vs model fits the observation best compared with the ReMi and SCPT models.

Figure 4.13 indicates two sharp velocity changes in the Vs structure, one being around 6m, the other being around 16m. I thus forced two sharp velocity boundaries at 6m and 16m and inverted for the 10 and 15 layers model to compare for the number of layers' effect on the inversion. The forward calculated dispersion curves using the 5,10,15 layers model are compared with observed data in Figure 4.17.

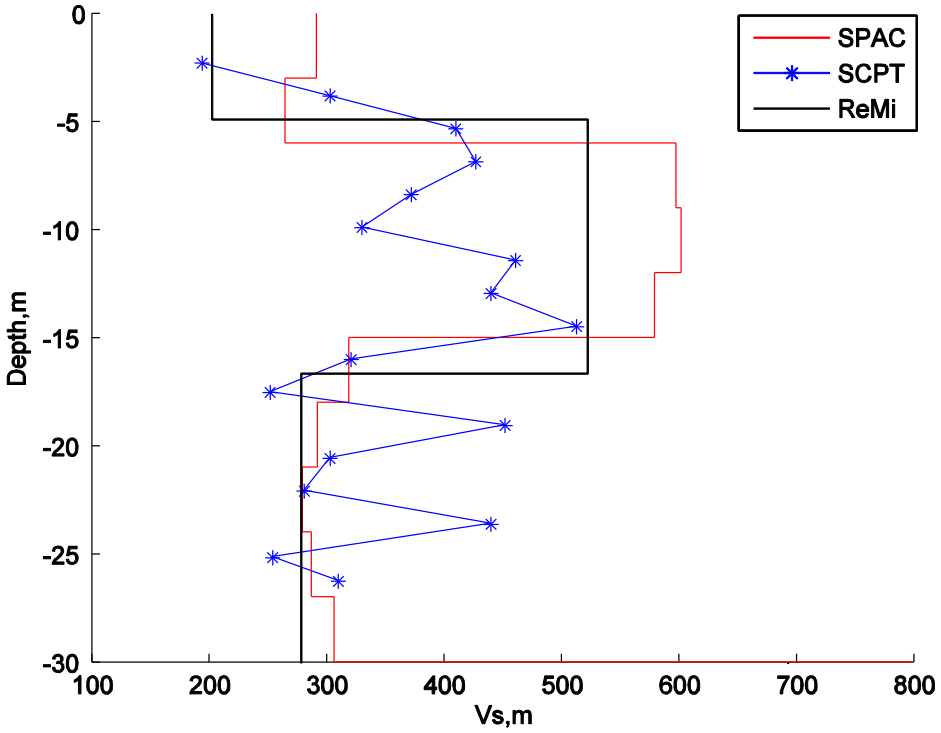

Figure 4.16: TRC site. Inverted 10-layer Vs structure from SPAC using linear inversion, with a forcing velocity discontinuity at 3rd layer (6m) and 6th layer (15m) (red line), compared with Vs obtained by SCPT (blue star) and ReMi (black line) method.

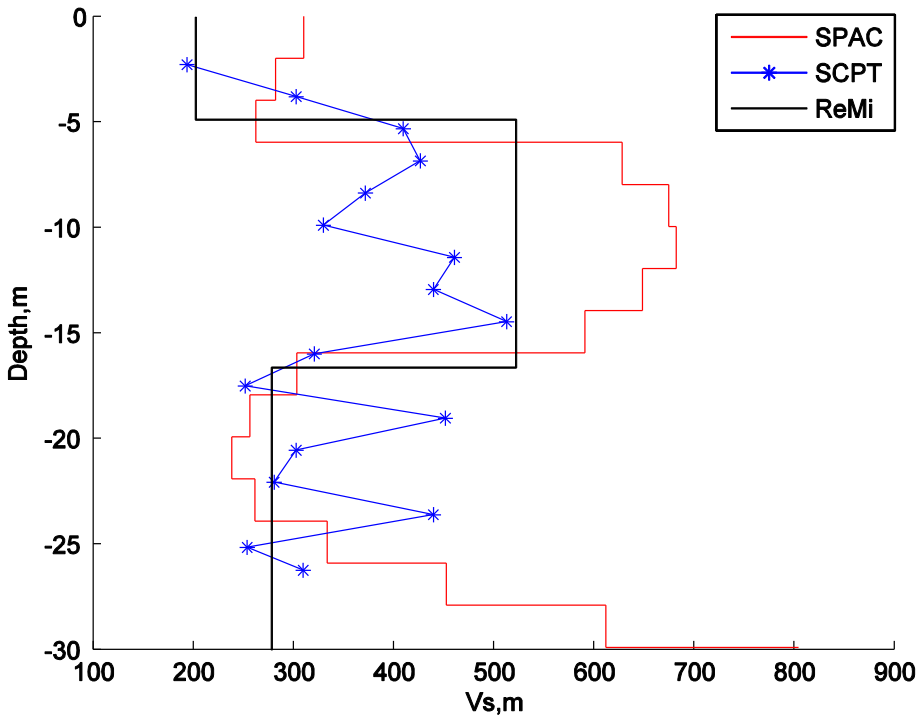

Figure 4.17: TRC site. Inverted 15-layer Vs structure from SPAC using linear inversion, with a forcing velocity discontinuity at 4th layer (6m) and 9th layer (16m) (red line), compared with Vs obtained by SCPT (blue star) and ReMi (black line) method.

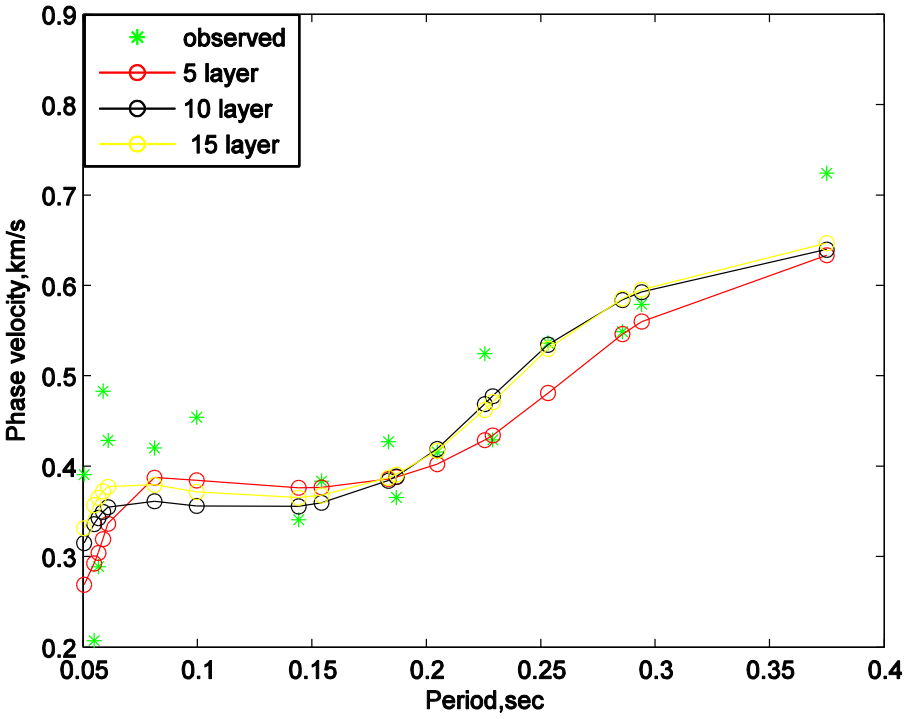

Figure 4.18: TRC site. Comparison of forward calculated dispersion curves for different number of layer Vs model. Red circle: 5 layer Vs model (Figure 4.14), Black circle: 10 layer Vs model (Figure 4.16), Yellow circle: 15 layer Vs model (Figure 4.17). Green star: observed dispersion data.

By forcing sharp velocity boundary at around 5m and 16m, the inverted Vs models match SCPT and ReMi well. All models have a "low-high-low-high" velocity structure, that the Vs increasing at around 5m from below 300m/s to 500m/s, then decreasing to 300m/s at depth 15m, and again increasing at around 30m depth.

4.3.1 Effect P wave velocity on inversion

Although shear velocity is the most sensitive to Rayleigh wave dispersion curve, other layer properties, including P wave velocity, density, and layer thickness, also have effect

on the inversion of shear velocity from surface wave dispersion data. Among them, P wave velocity (Vp) is considered to have certain contribution to the Vs inversion. I thus examined different Vp values' effects on Vs inversion. I fixed Vp with 1500m/s, Vp/Vs ratio as 2,3,4 and did the inversion respectively. The inverted Vs for the three sites are shown from Figure 4.19 to 4.21

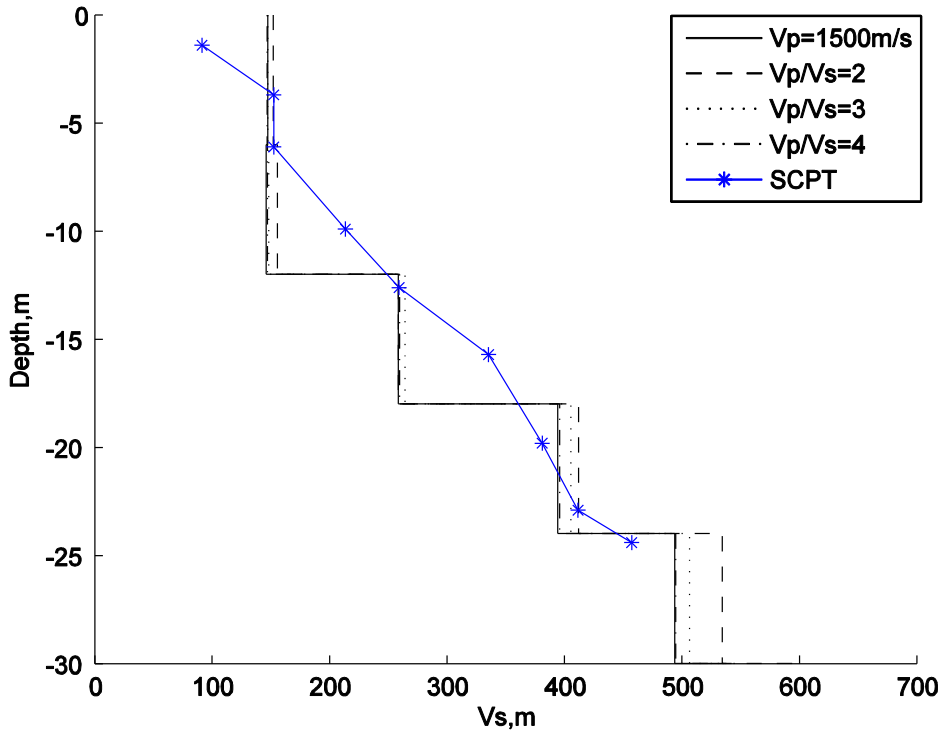

Figure 4.19: WFP site. Different Vp value inversion. Solid line: fix Vp=1500m/s. Dash line: fix Vp/Vs=2. Dotted line: fix Vp/Vs=3. Dash-Dot line: fix Vp/Vs=4. Blue star: SCPT data.

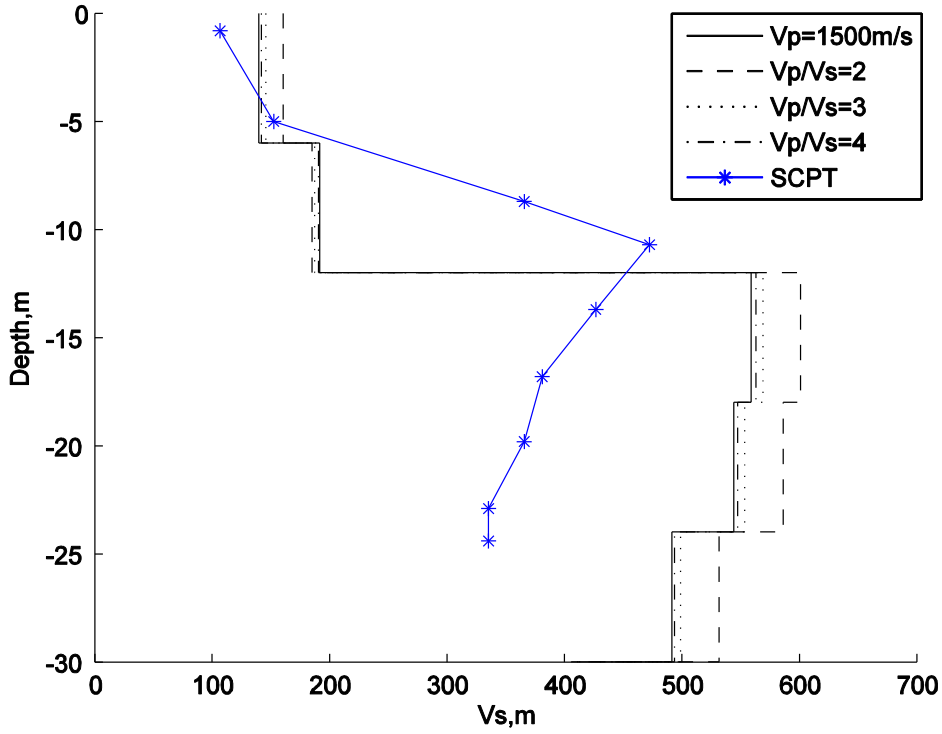

Figure 4.20: MBB site. Different Vp value inversion. Solid line: fix Vp=1500m/s. Dash line: fix Vp/Vs=2. Dotted line: fix Vp/Vs=3. Dash-Dot line: fix Vp/Vs=4. Blue star: SCPT data.

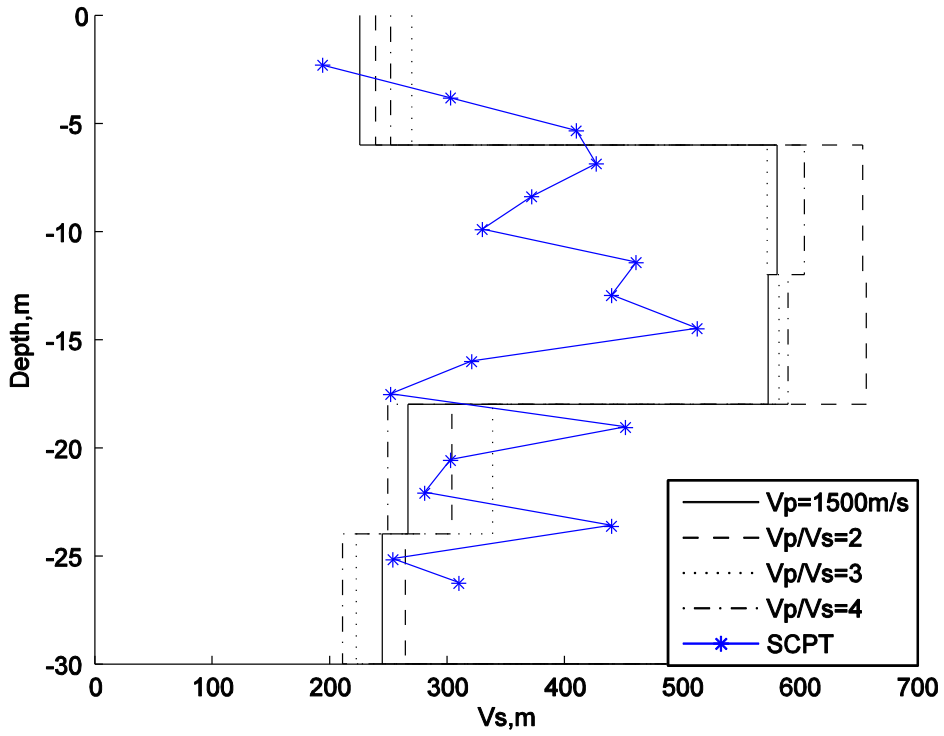

Figure 4.21: TRC site. Different Vp value inversion. Solid line: fix Vp=1500m/s. Dash line: fix Vp/Vs=2. Dotted line: fix Vp/Vs=3. Dash-Dot line: fix Vp/Vs=4. Blue star: SCPT data.

The inverted Vs models above indicate that the Vp values do not have significant effect on the Vs inversion.

4.3.2 Effect of depth on inversion

Although the aim of our research is to investigate the shallow Vs structure (Vs30, upper 30m), the SPAC method could in principle go to any depth, as long as the size of array is properly chosen. The minimum depth depends on the minimum sampled wavelength, which is related to the spatial sampling, and equals to the minimum interstation distance. The maximum depth depends on the maximum propagating wavelengths, which is related to the largest distance between any two stations in the array. The maximum inversion depth has a significant effect on inversion as shown in Figure 4.22 to 4.24 for WFP site,

with a maximum depth of 50m, 75m, 100m respectively, compared with depth of 30m in Figure 4.3. When the initial model started with equal layer thickness and the same velocities, the inversion with the shallowest maximum depth of 30m (Figure 4.3) yields the best match with borehole SCPT measurements. Although Vs of the deeper layers (>30m) are not well constrained by the borehole data, because the borehole did not reach 30m, Vs of shallow layers of all models (<30m) are not affected significantly by the maximum depth of the inversion. The increasing velocity feature from 100m/s near surface to above 400m/s at around 30m is well represented by all models.

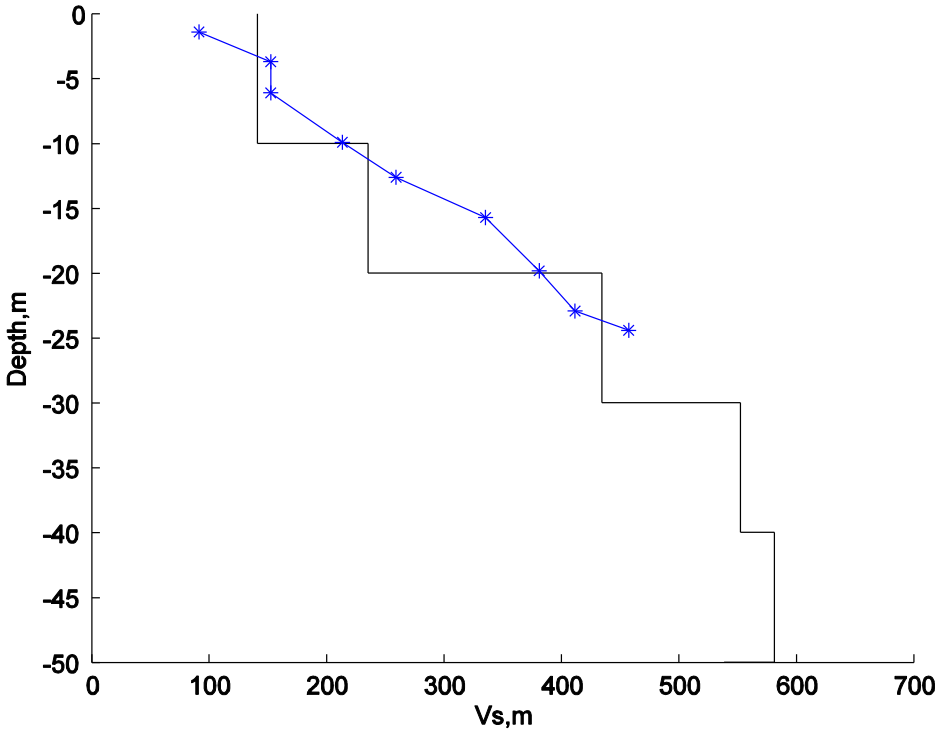

Figure 4.22: WFP site. Black line: Inverted Vs with maximum depth 50m. Blue star: borehole SCPT data.

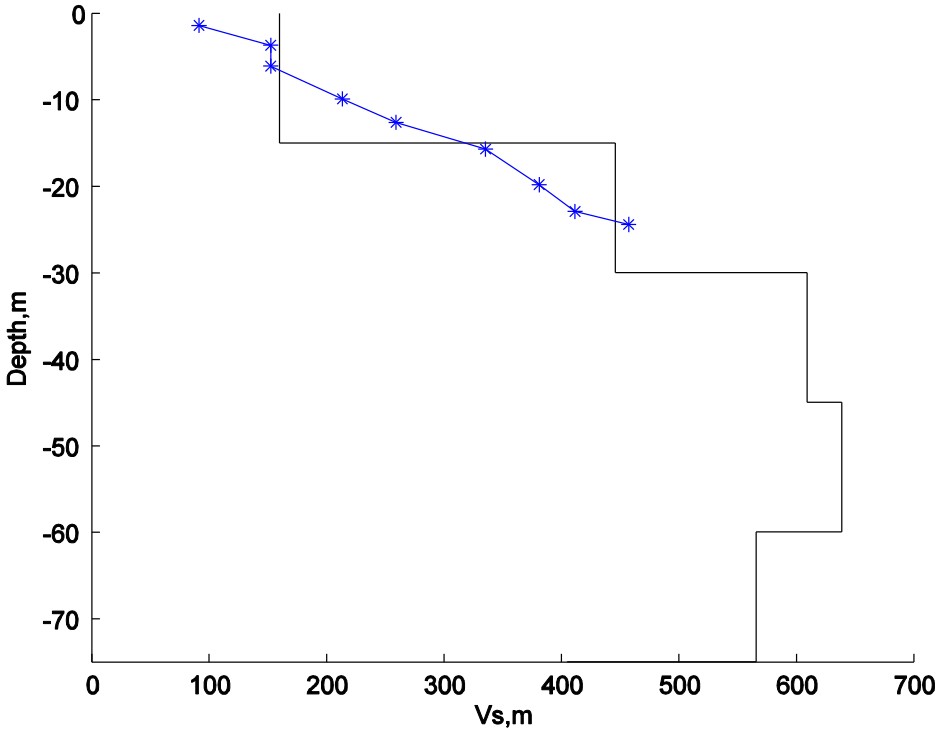

Figure 4.23: WFP site. Black line: Inverted Vs with maximum depth 75m. Blue star: borehole SCPT data.

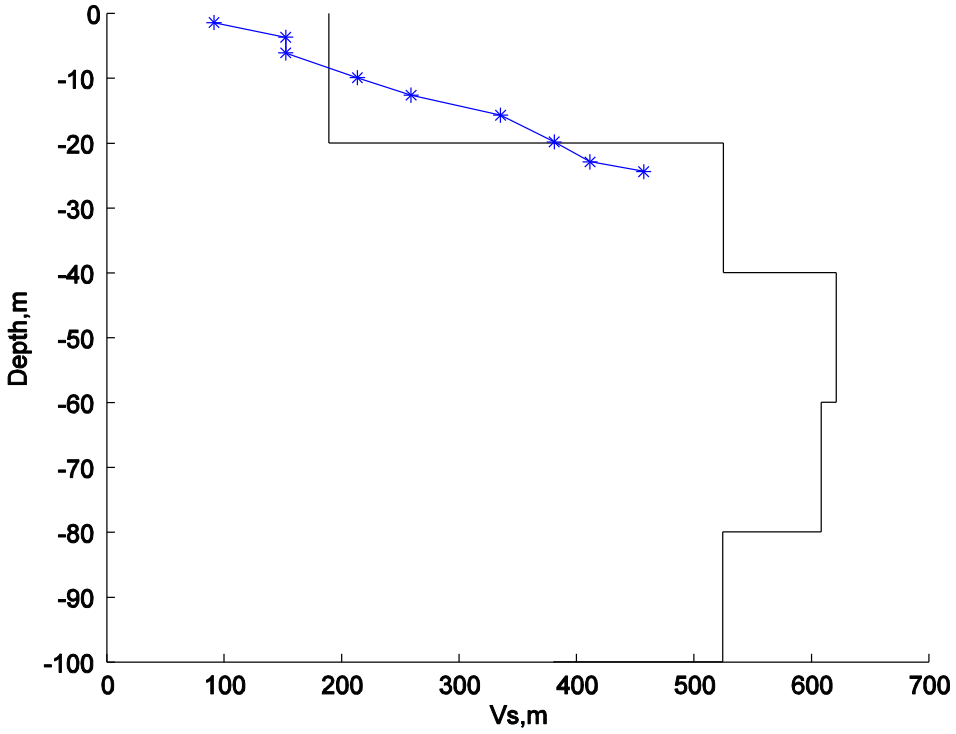

Figure 4.24: WFP site. Black line: Inverted Vs with maximum depth 100m. Blue star: borehole SCPT data.

[Constrained/Joint inversion]

All inverse problems I discussed above actually fall into a general topic of optimization problem in the context of applied mathematics. We defined some forms of cost function, either data misfit, or a combination of the model size (regularization), and then tried to find models that could minimize the cost function.

The models we have solved are purely based on the observed data and the physical model, without any other information. In other cases, we might have some information related to the model, or some prior information that we know before doing the inversion. For the

seismic velocity inversion problem, we might have some knowledge of the geology of the area, and therefore, we have either some rough guesses about the velocity we want to derive, or a general knowledge of possible range that the velocity could possibly falls into. Further, we might have some previous investigation results in the same area. In such cases, we want to incorporate all prior knowledge about the model into the inversion process. Compared with the inversion without any prior information, the types of knowledge we have had put constrains on the model, which could in turn improve the accuracy of the inversion result significantly. This is called **constrained inversion** or **joint inversion**, opposite to the unconstrained inversion.

For the SPAC inversion of shear wave velocity that I discussed above, I have some previous shear wave velocity estimation obtained either through borehole measurements or by other seismic methods like ReMi. I thus could use the information as constrains when doing the inversion.

Mathematically, recall that for unconstrained inversion, the cost function we want to minimize is a measure of the data misfit

Min $\|\boldsymbol{d} - \boldsymbol{Gm}\|$

Suppose we have certain information about the model **m**, we denote it by

$v = \{v_j\}$, j=1,2,..n.

where **v** is the same length as model vector **m**. For SPAC inversion, v could be the prior borehole or the ReMi shear wave velocity estimation.

For the inversion, we not only want to minimize the data misfit, but also want our estimated model as close to the prior information v as possible, since this prior information v provides some knowledge about the model.

Mathematically, the cost function we want to minimize now becomes,

$$\text{Min } \|d - Gm\|^2 + \sum_{j=1}^{N} \alpha_j (m_j - v_j)^2 \quad (4.3.22)$$

Where α_j (j=1,…,N) denote weights for individual model parameters with respect to the constrain **v**.

Define weight matrix **W**, such that

$$diag(W) = \alpha = \begin{bmatrix} \alpha_1 & & \\ & \ddots & \\ & & \alpha_N \end{bmatrix}_{N \times N}.$$

We get the solution by taking the first derivative of equation (4.3.22) with respect to **m**, and setting it equal to zero,

$$\widetilde{m} = (G^T G + W)^{-1}(G^T d + Wv). \quad (4.3.23)$$

This is the solution to the constrained inversion (4.3.22) given the constrain **v**.

I used the smoothed SCPT data as constrain for Vs inversion. The inverted Vs model for WFP site is given in Figure 4.19. The constrain is obtained through 2-point averaging of

the SCPT data.

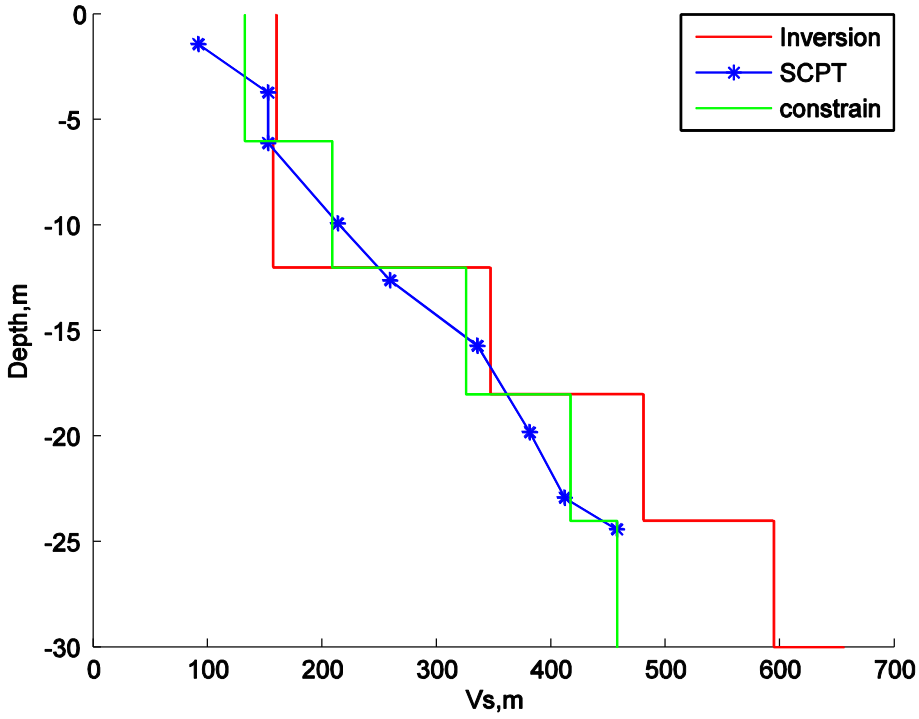

Figure 4.25: WFP site. Vs model from constrained inversion model (Red). Blue star: SCPT data. Green: smoothed SCPT as constrain.

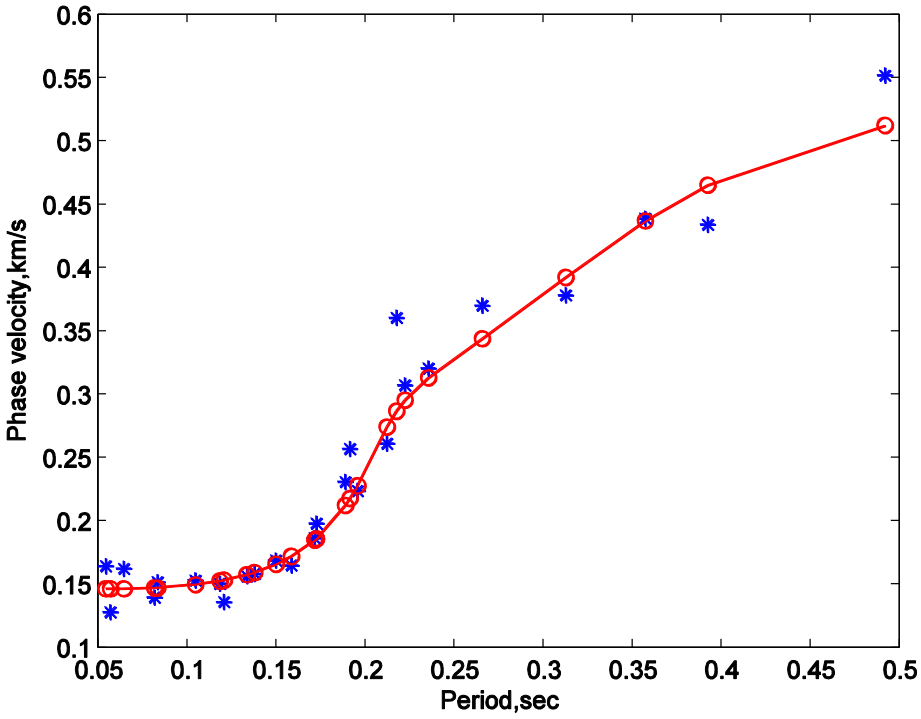

Figure 4.26: WFP site. Dispersion curve calculated from Vs model that is obtained from constrained inversion (Red circle), compared with observed dispersion data (blue star)

The inverted Vs model for MBB site is given in Figure 4.27. The constrain is obtained through 2-point averaging of the SCPT data.

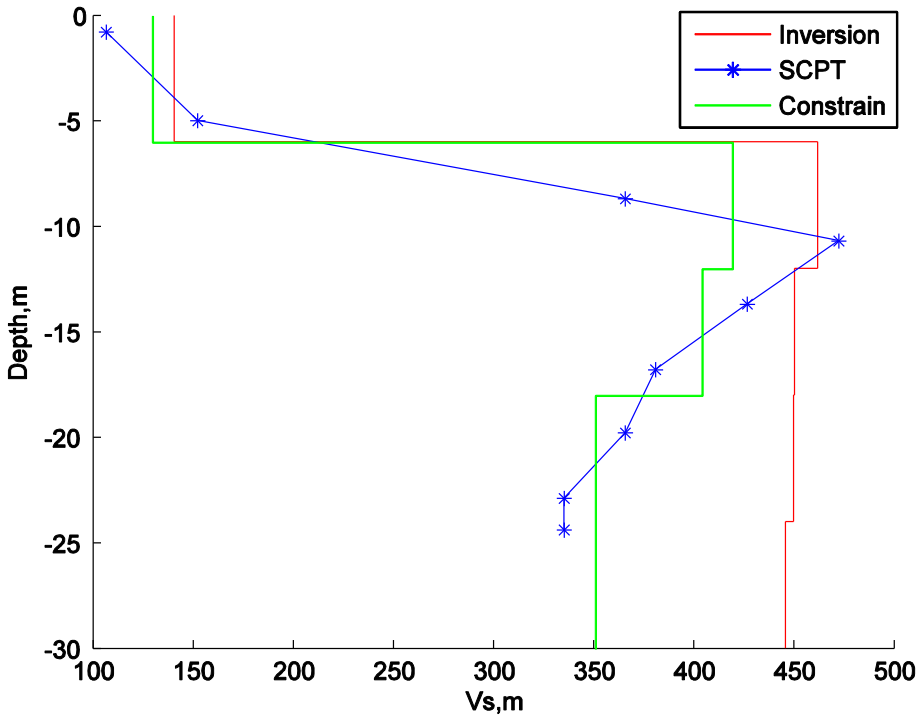

Figure 4.27: MBB site. Vs model from constrained inversion (Red). Blue star: SCPT data. Green line: smoothed SCPT as constrain.

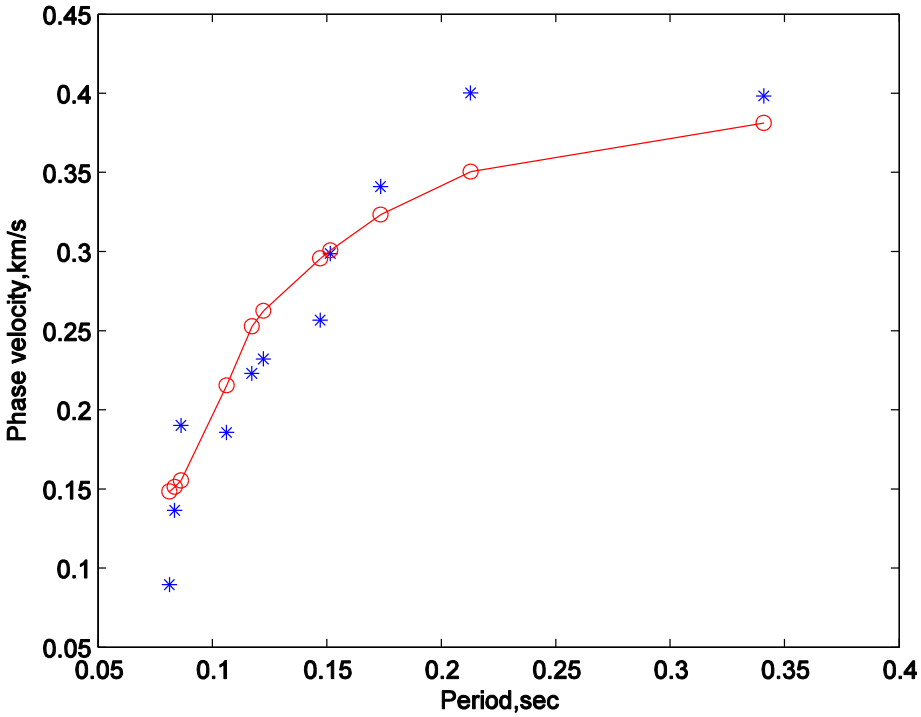

Figure 4.28: MBB site. Dispersion curve calculated from Vs model that is obtained from constrained inversion (Red circle), compared with observed dispersion data (blue star)

By using the smoothed SCPT as constrain, the inverted Vs model shows a sharp velocity jump at the second layer at around depth 6m for MBB site (Figure 4.27), which is consistent with the pattern of SCPT data.

For TRC site, I used 3-point averaging to smooth the SCPT data as constrain. The SCPT for TRC site is measured to depth 26m. So the inverted Vs model is constrained for upper 30m.

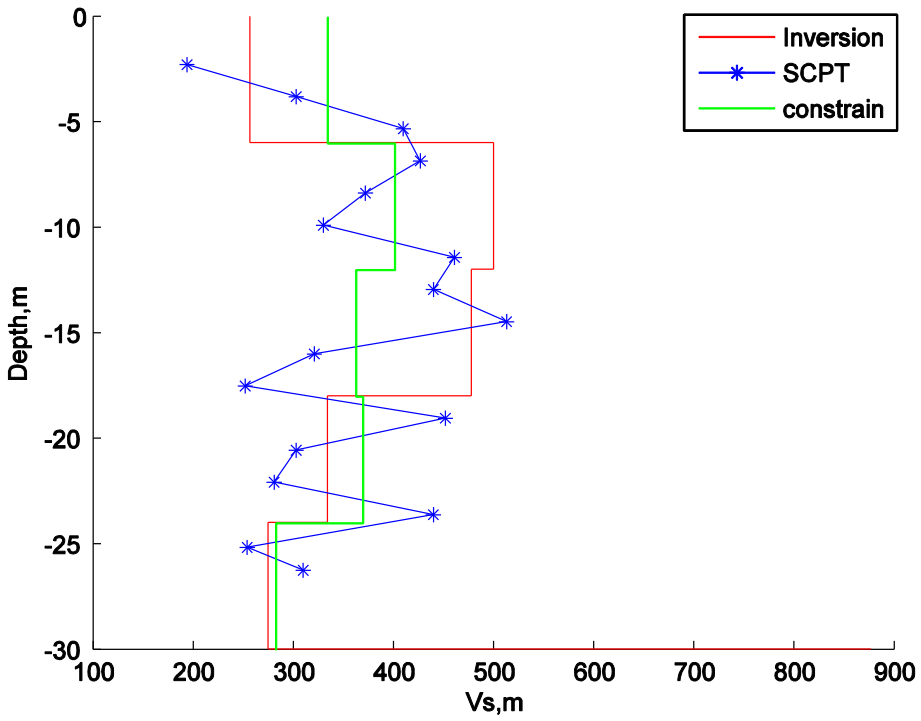

Figure 4.29: TRC site. Vs model from constrained inversion (Red). Blue star: SCPT data. Green line: smoothed SCPT as constrain.

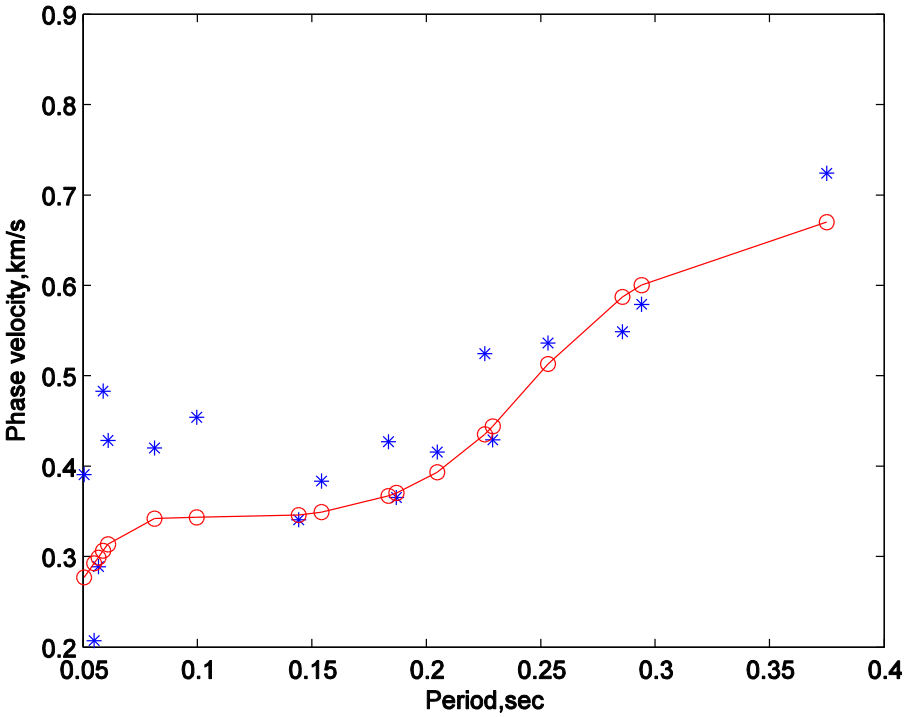

Figure 4.30 TRC site. Dispersion curve calculated from Vs model that is obtained from constrained inversion (Red circle), compared with observed dispersion data (blue star)

By adding the SCPT data as the constrain, the inverted Vs will not deviate far away from the prior SCPT estimation, because the sum of the misfit dispersion data and the estimated Vs model's distance from SCPT constrain are minimized. Compared with the unconstrained inversion, the prior Vs information, SCPT in this case, is integrated into the inversion and it will control the iterative process so that the estimated model would not move away from SCPT constrain too much. Features in SCPT including the sharp velocity boundary as in MBB site, and the low velocity zone as in TRC site are well characterized through the constrained inversion.

4.4 Non-linear Inversion

4.4.1 Overview.

In section 4.3, I discussed the techniques of solving discrete linear inversion, Gm=d. Solving nonlinear inversion problem is important, since most geophysical problems are nonlinear. For non-linear case, G(m)=d, we can linearize the problem and use iterative methods like Gauss-Newton or Levenberg-Marquardt algorithm.

However, there are certain problems associated with iterative methods for nonlinear problems. First, iterative methods very much depend on the starting model, meaning that they require an initial guess as the starting model. The problem is to find a minimum for the cost function. But the nonlinearity of the problem usually results in multiple local minimums to the cost function and if the starting model is too far from the “global minimum”, the final result may be trapped within one of the “local minimums” (Figure 4.25)

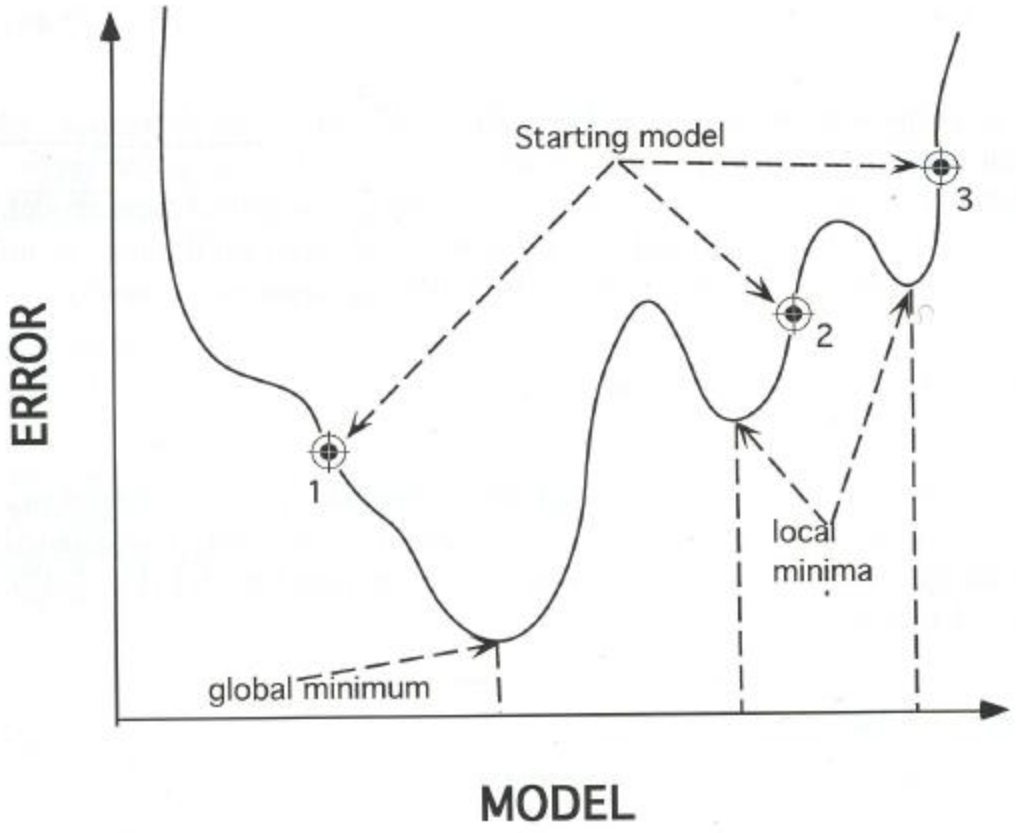

Figure 4.31: A hypothetical error function as a function of model (the model is assumed to have only one model parameter) showing several minima. The iterative method will find the global minimum only when starting around position 1. Others will end up in some other local minima of the error function. (Sen & Stoffa 1995)

Second, the iterative methods usually require the computation of partial derivative matrix, or Jacobian, when updating model during the iteration. For some complicated functions, there may not be analytical formula for the partial derivative. Numerical approximation, finite-difference method usually, is applied then. But the accuracy of numerical approximation is often a problem and when they accumulate at each step, the errors lead to a significant deviation of the estimated model from the true model.

Various global optimization methods of solving nonlinear optimization problems have been developed, aiming to find the global minimum of the nonlinear function, with little dependence on starting model and without the need to calculate the partial derivatives. Grid search method and Monte Carlo type random search techniques are two of the most popular ones.

The grid search method involves a full exploration of the model parameter space, and an evaluation of the function at each point to find the best fits. For geophysical problems, the model space is usually so large that the forward calculation at each model space point requires huge amount of computations. For example, for Rayleigh wave dispersion curve inversion, if we parameterize the Earth model as 10 layers, as in Figure 4.1 (Section 4.1), and fix layer thickness, each layer still has three parameters to be determined, i.e. Vp,Vs, and density. If we discretize the model parameter space and allow each for 10 possible values, which has already simplified the problem significantly, the model space still has 10^{30} data points in order to explore fully. In other words, the function needs to be evaluated 10^{30} times. The computation amount is so huge that it is usually impractical and inefficient to use grid search method for geophysical inversion.

4.4.2 Monte Carlo method

We have seen that the grid search method requires a thorough examination of the model space in that models are tested one by one against the data in order to find a best fit. In the case where model spaces are large, the amount of computation is huge. Compared

with the grid search, Monte Carlo methods are random search methods, meaning that models are randomly drawn from the model space. Monte Carlo methods, broadly speaking, are experiments that make use of random numbers to solve problems that are either probabilistic or deterministic in nature (Sambridge & Mosegaard 2002).

Press (1968) first applied Monte Carlo method in solving geophysical inverse problem to obtain Earth models. The data Press used included 97 eigenperiods, the travel time of compressional and shear waves, mass and moment of inertia of the earth. The model parameters to be determined are the compressional (α) and the shear wave velocity (β) and the density (ρ) in the Earth. Press pre-defined the upper and lower bounds, which were different for different model parameters and selected randomly for each model parameter that fell within the bounds. Only six out of a total of five million models passed all tests. Of the six models, three were finally selected.

The flow diagram of Monte Carlo methods used by Press is shown as following,

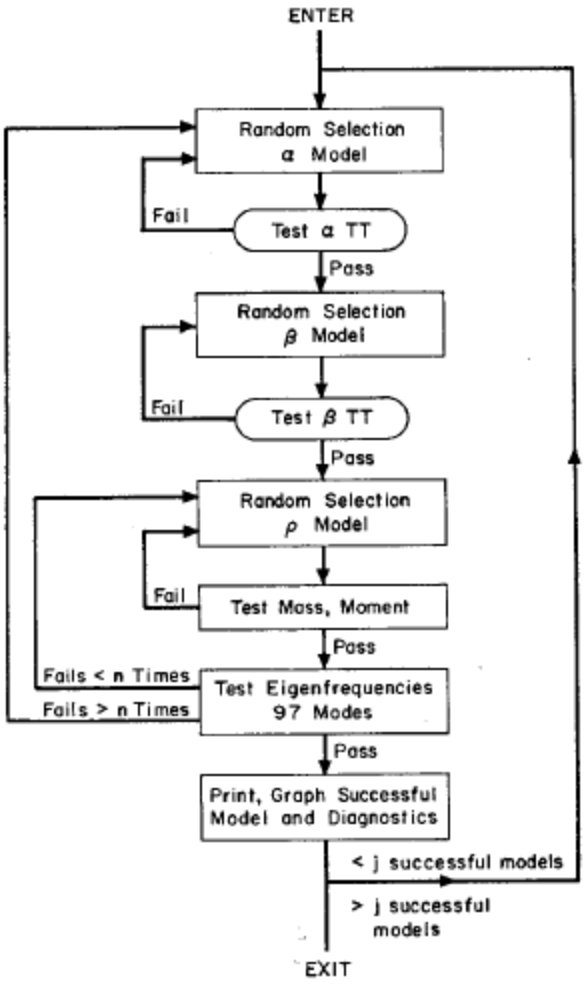

Figure 4.32: Flow diagram of Monte-Carlo inversion procedure. (Press 1968)

The results from Press are given in the figure below,

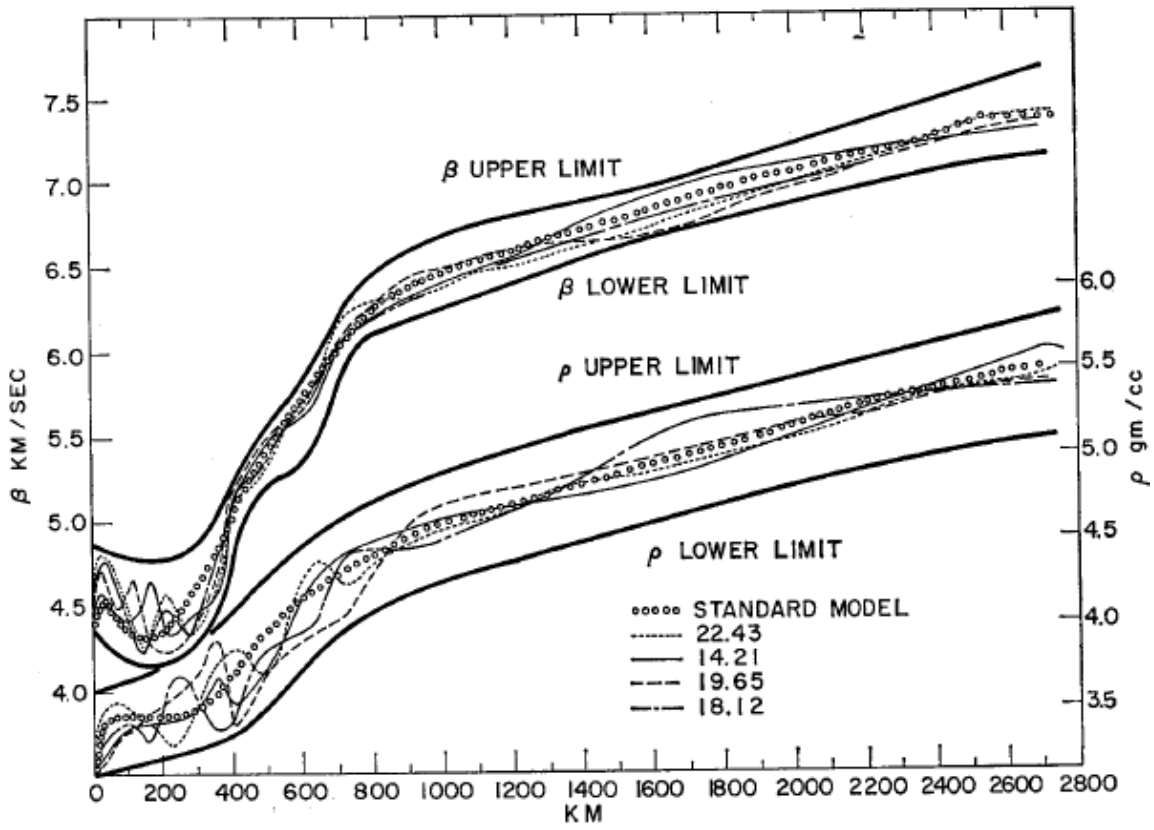

Figure 4.33: Results from the Monte Carlo inversion of Press (1968). shear wave velocity (β) and density (ρ)distributions for the mantle for the standard model and for three successful Monte Carlo models. Model number also gives increase in core radius. Permissible β, ρ region shown by heavy curves. Model 14.21 failed ${}_0S_2$ test but is of interest because of excellent fit of higher modes.

One of the main advantages of the Monte Carlo inversion is that it avoided the assumptions of linearity between the data and the model on which linear inversion techniques relies. Also, Press (1968) was the first to address the issues of the uniqueness of the geophysical inverse problem with the Monte Carlo methods by direct sampling from the model space.

There are some drawbacks associated with the Monte Carlo inversion. First, in order to sample the model space as complete as possible, a large number of samplings and forward calculations are required to test against the data. The speed and efficiency of the algorithm is a problem when computing power is limited. Second, even for a large of number of sample models, like 5 million generated by Press (1968), the Monte Carlo methods still cannot guarantee that it has fully explored the model space.

I used the Monte Carlo method to invert for the Vs structure from dispersion curve obtained through SPAC to test the capability of random search type algorithm in solving Vs inversion problem. Based on previous SCPT data, I chose the upper and lower boundaries of each parameter so that the SCPT data fell into the search range of Monte Carlo algorithm. During each simulation, a model is randomly drawn from the predefined searching area from the uniform distribution. Synthetic dispersion curve is obtained through forward calculation using the sampled model, and then is compared with observed dispersion data to evaluate the model's misfit. After many times of simulations, the model with the smallest misfit is chosen.

The inversion result of Vs for WFP site is given in the figure below.

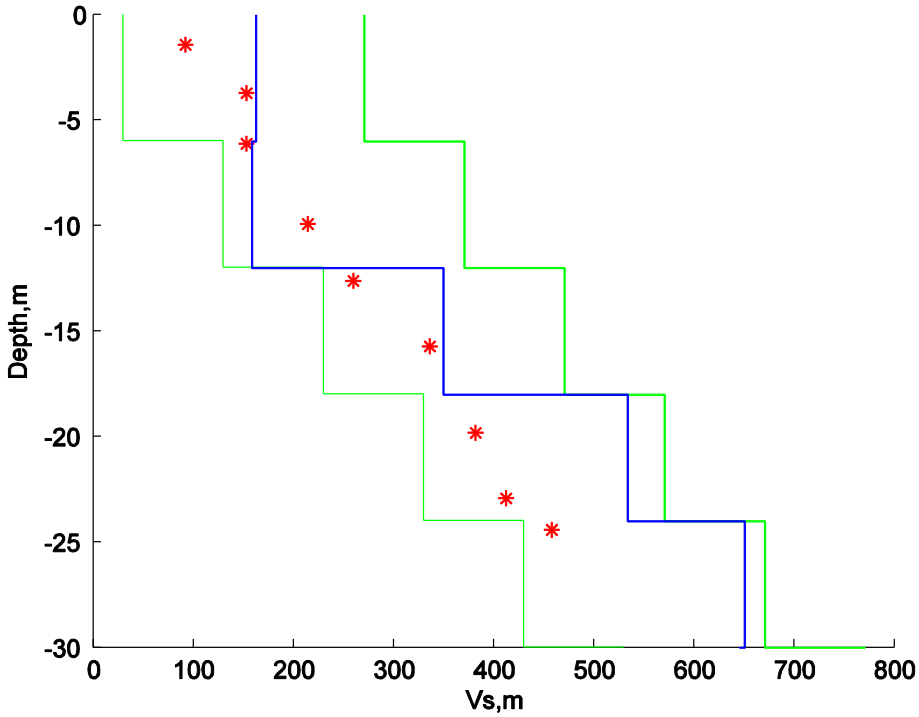

Figure 4.34: WFP site. Monte Carlo inversion result of Vs model (Blue line). Two green lines define the upper and lower boundary of the searching range. Red star indicate SCPT data.

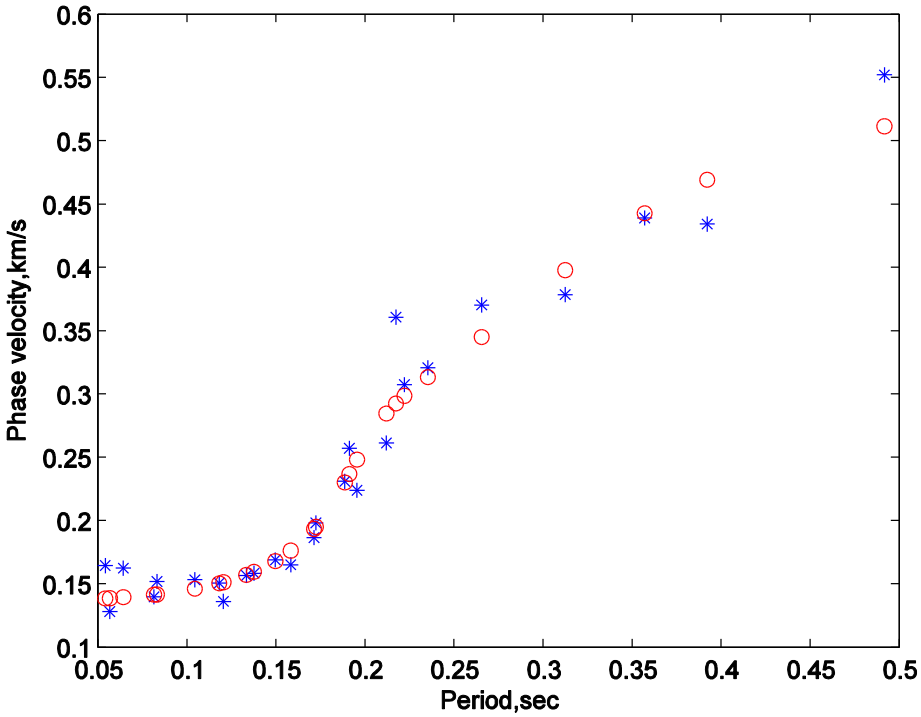

Figure 4.35: WFP site. Forward calculated dispersion curve from Monte Carlo inverted Vs model (Red circle) is compared with observed dispersion data (Blue star).

Figure 4.34 shows that the inverted Vs model using Monte Carlo fits the observed dispersion data well. The Monte Carlo algorithm finally selects the model that has the minimum misfit error after a proper selection of the search boundary and many times of simulations, 15000 times in this case.

In the early time when Monte Carlo methods were first introduced into geophysical inverse problems, as used by Press (1968), the sampling in the model space was uniform, meaning that discrete Earth models were generated from uniform distribution defined by the pre-selected upper and lower bounds. This uniform sampling sometimes leads to a

waste of computation in that later sampling models would probably be the same or closed to the previous rejected ones. Thus more advanced and sophisticated searching techniques are developed and applied into geophysical inverse problems. Simulated Annealing is one of the most appealing algorithms for the nonlinear global optimization problems.

4.4.3 Simulated Annealing

The Simulated Annealing (SA) method was first proposed by Kirkpatrick et al. (1983) to solve nonlinear global optimization problems. It is a Monte Carlo method based on Metropolis' algorithm (1953). The idea of SA is borrowed from statistical mechanics. In the physical annealing process, a solid material is heated up by increasing temperature so that it becomes melted, resulting in all particles distributing randomly. This is followed by a slow cooling when particles arrange themselves to reach a lower energy state, or energy ground state. When energy ground state is reached, all particles are stable and crystallization occurs. In the optimization problem, the objective function to be minimized is analogous to the crystalline materials. By appropriately choosing a "cooling schedule", the function "cools" slowly and reaches the minimum energy state.

The Metropolis et al. algorithm (1953) was the first method to simulate the behavior of the physical system in thermal equilibrium. Denote model as **m**, the energy function as E(**m**), for each model parameter m_i, a random perturbation Δm_i is made and the model is updated to $m_i + \Delta m_i$, and the new energy function is computed as $E(m_i + \Delta m_i)$, and

the change in energy is $\Delta E = E(m_i + \Delta m_i) - E(m_i)$. If $\Delta E \leq 0$, i.e. energy decreases, the new model $m_i + \Delta m_i$ is accepted, while if $\Delta E \geq 0$, the new model is accepted with probability,

$P(\Delta E) = e^{-\Delta E/T}$.

where T is the temperature parameter.

For a large number of times of repeated perturbations, it can be shown that the thermal equilibrium could be reached for each temperature.

Based on Metropolis' algorithm, the SA algorithm proposed by Kirkpatrick et al. (1983) lowers the temperature T slowly. If the equilibrium state is maintained and the system cools slowly, it will finally reach the ground energy, or minimum energy state.

One of the most appealing features of SA algorithm is that it can escape from the local minima without being trapped within the region and could reach the global minimum with a high degree of accuracy. SA thus becomes highly suitable for the nonlinear problems, where the objective function often have multiple local minimums.

Rothman (1985, 1986) first introduced SA into geophysics, when he successfully applied SA to solve large residual statics problems in exploration seismic. Realizing the power of SA to solve nonlinear geophysical inverse problem, SA becomes popular among

geophysicists and seismologists quickly. Applications include travel time inversion (Pullammanappallil & Louie, 1993, 1994), earthquake location (Billings, 1994), seismic ray tracing (Velis & Ulrych, 1996), etc.

I used Metropolis simulated annealing algorithm described as the following pseudo code to invert for the Vs from dispersion curve obtained from SPAC method.

Metropolis Simulated Annealing algorithm.

****

Start from a random model m_0 with energy $E(m_0)$

Loop over temperature (T)

- - Loop over certain number of iterations for each T,

- - Randomly generate a new model m_1 within the pre-defined model range.

- - Calculate $E(m_1)$ for the new model m_1

- - $\Delta E = E(m_1) - E(m_0)$

- - $P = \exp\left(-\frac{\Delta E}{T}\right)$

- - if $\Delta E \leq 0$, then

- - - $m_0 = m_1$

- - - $E(m_0) = E(m_1)$

- - end if

- - if $\Delta E > 0$, then

- - - draw a random number from uniform distribution, r=U[0,1]

- - - if $P > r$ then

- - - - $m_0 = m_1$

- - - - $E(m_0) = E(m_0)$

- - - end if

- - end if

- - End loop

End loop

****

I choose the cooling schedule as,

$T(k) = \frac{T_0}{k}$.

Where k denotes kth iteration of temperature, T_0 is the starting temperature.

I use the Root-Mean-Square (RMS) error as the misfit function, or energy function E for SA, RMS is defined as,

$RMS = \sqrt{\frac{1}{N}\sum_{i=1}^{N}(V_i^{obs} - V_i^{syn})^2}$.

Where N is the total number of phase velocity data. V_i^{obs} is the ith obverved phase velocity, V_i^{syn} is the ith forward calculated phase velocity from model. The objective is to find the model that could globally minimize the RMS.

The SA inverted result of Vs is given in Figure 4.36.

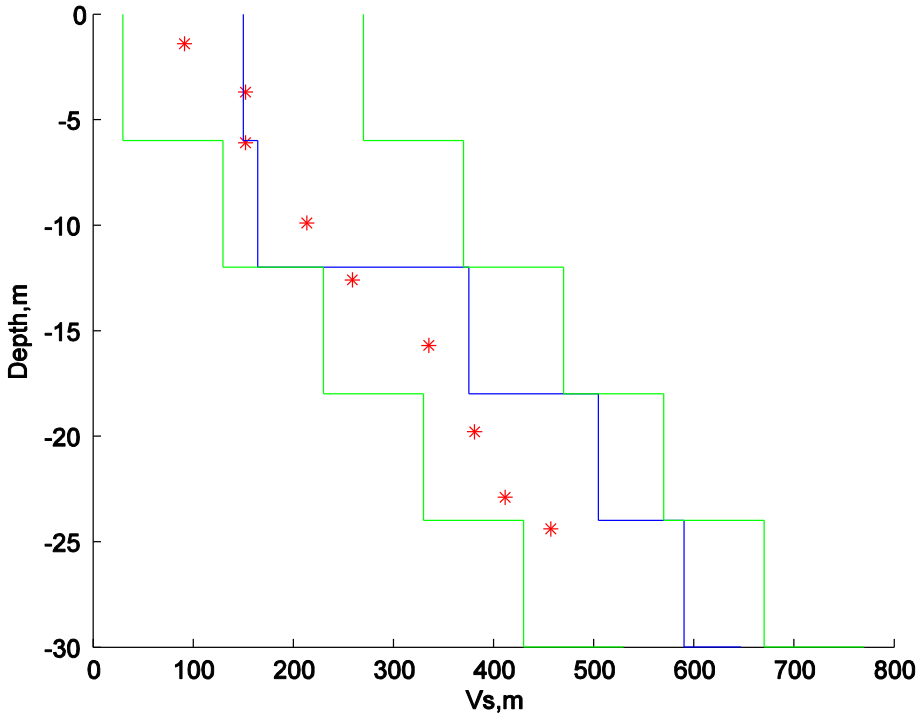

Figure 4.36: WFP site. SA inverted Vs model (Blue line). Two green lines denote upper and lower boundary for searching space. Red stars are SCPT data.

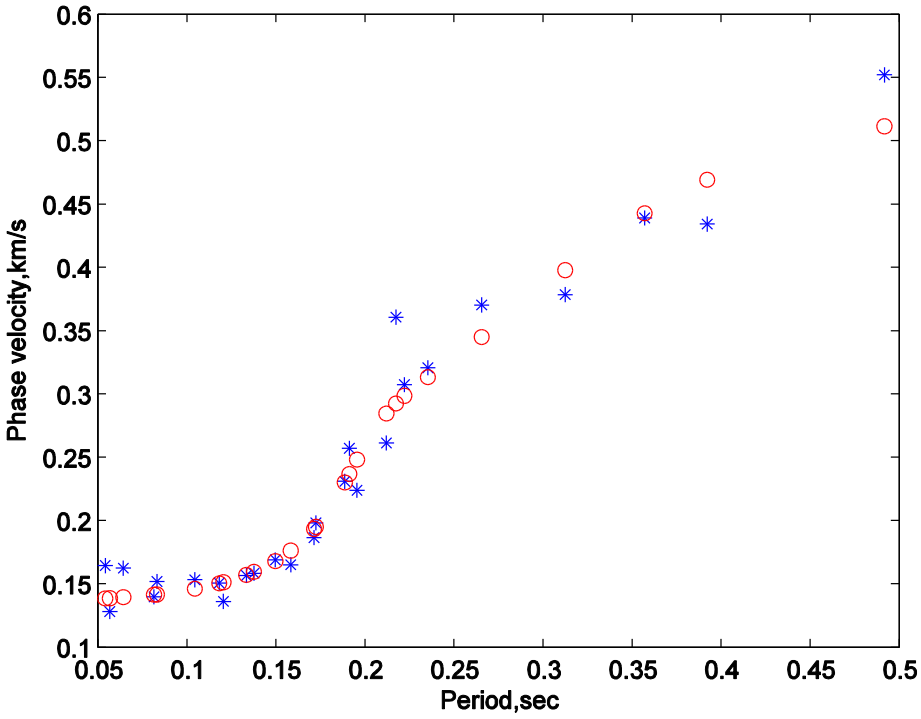

Figure 4.37: WFP site. Forward calculated dispersion curve using SA inverted Vs model (Red circle) compared with observed dispersion data (Blue star).

Figure 4.36 shows that the Simulated Annealing algorithm inverted model could fit the observation well. The RMS of all iterations of SA is provided in Figure 4.38, and Figure 4.39. The global minimum is finally reached at the lowest temperature.

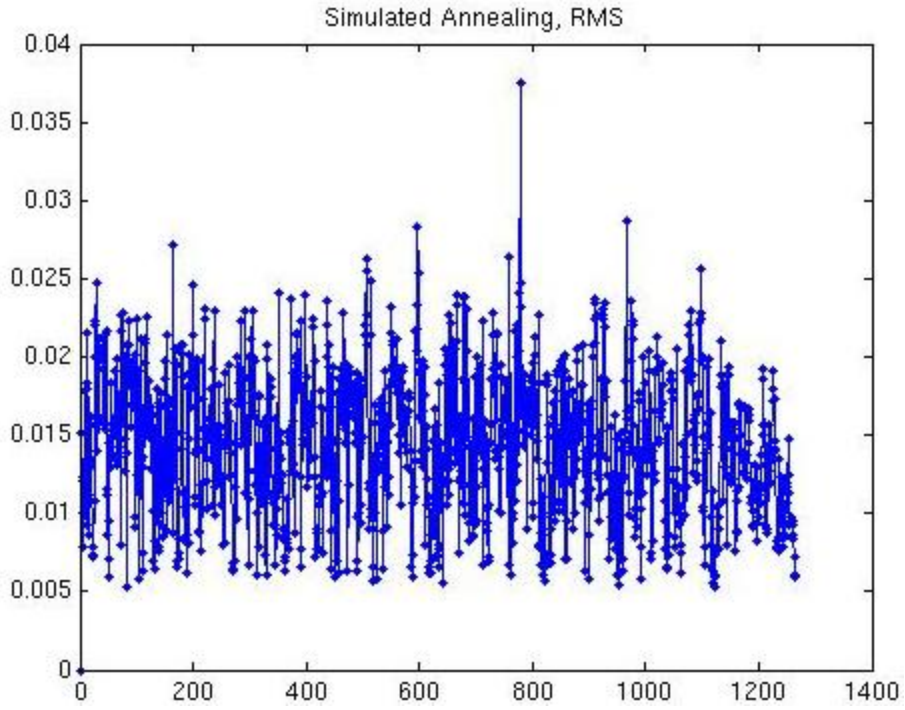

Figure 4.38: RMS for SA of all iterations of all temperatures.

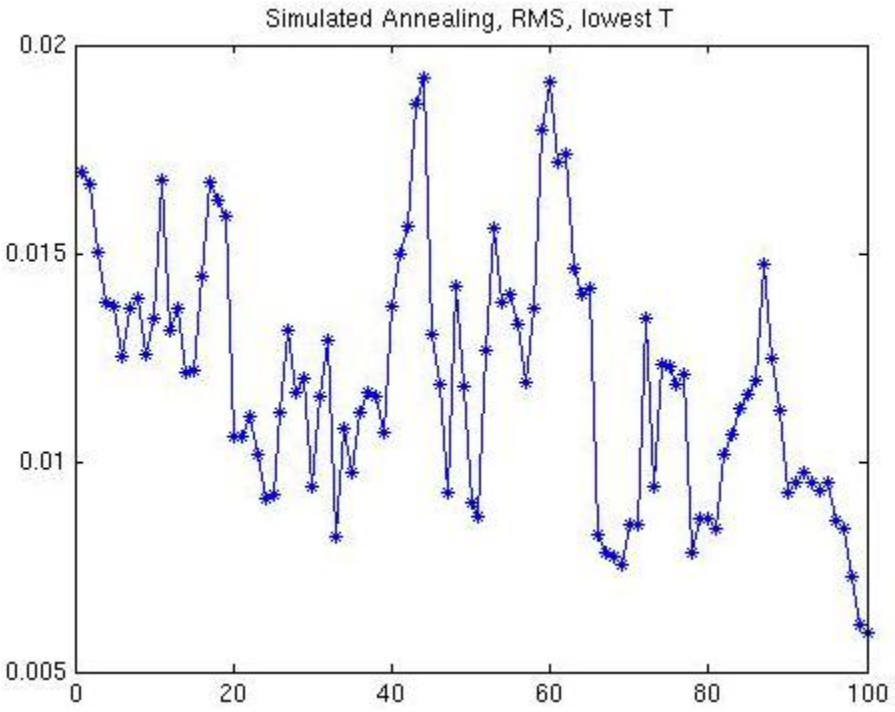

Figure 4.39: RMS for all iterations for the lowest temperature T.

Figure 4.39 shows the RMS for all iterations during the lowest temperature. After 100 iterations, the energy function, RMS, reach the lowest level, corresponding to the global minimum.

4.5 Stochastic Inversion & Ensemble inference.

All previous inversion techniques, from linear least square method, Monte Carlo, to Simulated Annealing algorithm, try to find the "best fit" models that could best explain the observation. As discussed in section 4.1, one common problem faced by inverse problem, especially when inverting for the Earth models, is that the solution may not be unique. There might be multiple models that could fit the data equally well, because the observed data often contain noises, and the model is usually nonlinear. The nonuniqueness leads to one question that geophysicists often ask when solving geophysical inverse problems, that is, is seeking the single "best fit" model the best way to tackle the problem? Or is this "best fit" model really the "true model"? Also, when using certain searching algorithm, including Monte Carlo and Simulated Annealing, to explore the model space, we try to find the global minimum of the function. While seeking the global minimum, the algorithm itself often discards all other samplings. However, are these samplings really useless? In other words, is there a way to utilize the collection of Earth models generated by the Monte Carlo?

All these questions lead to a new method for the inverse problem, ensemble inference, or stochastic inversion. Instead of looking for one "best fit" model, the method tries to find

the characteristics and properties shared by all plausible solutions of the inverse problems. By generating a suite of models, or "ensemble", that fit the data in some sense, the solution becomes the description of the common properties shared by the ensemble. Statistical treatment, in a stochastic manner, is usually applied to analyze the ensemble. The focus of the inversion changes from solving for a particular model to infer the common characteristics of the ensemble of acceptable models. (Vasco et al. 1993)

Ensemble inference, or stochastic inversion, is particular suitable for geophysical inversion when the problem is to solve Earth models. One single model could not capture the complexity of the Earth well as long as the subsurface of the Earth is heterogeneous. The shared properties of the ensemble of models, in turn, could provide a description of the structure of all acceptable models, without being too focus on the complexity of one single model.

Acceptable inference about the ensemble of models could be made when using Monte Carlo type algorithm, because a good understanding of the structure of the model space could be obtained through random sampling, and statistical treatment could be applied to those models with acceptable level of fitness to the data.

Statistical moments, especially the first two moments, mean and variance, are important quantities to characterize large data sets. If the mean and variance of the ensemble of models could be estimated, it could provide useful information about the structure of the models ensemble.

I used the following procedures to make inference about the model ensemble:

(1) By properly selecting the range of each parameter based on prior information obtained by linear inversion, SCPT, and ReMi, I applied Monte Carlo methods as many times as possible to sample the model space of Vs.

(2) Forward calculating each sampled Vs model to obtain synthetic dispersion curve. By examining the misfit function, RMS, I selected certain level of RMS, which was acceptable in my view.

(3) I estimated the statistical mean, and variance of those models with acceptable RMS, and calculated the Vs model for 1-standardard deviation (1σ) and 2-standard deviation (2σ) from the mean.

(4) By forward calculating the dispersion curve from the mean, 1σ and 2σ Vs model, I examined whether they could effectively capture the observed dispersion data, as well as the borehole SCPT Vs measurements. [Menke. Personal communication for suggesting comparing SCPT with ensemble modeling, 2010]

(5) The mean, 1σ and 2σ of Vs give a good insight on the properties shared by the ensemble of all acceptable models.

Below is an example of RMS (Figure 4.40) and histogram (Figure 4.41) after 15000 Monte Carlo simulations,

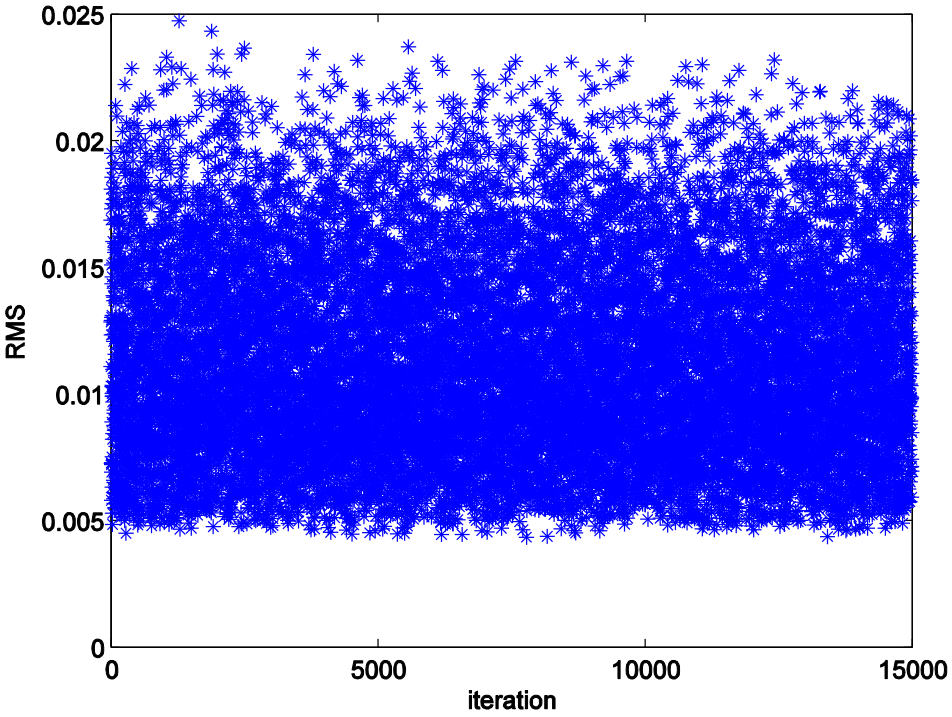

Figure 4.40: RMS of 15000 times Monte Carlo simulations

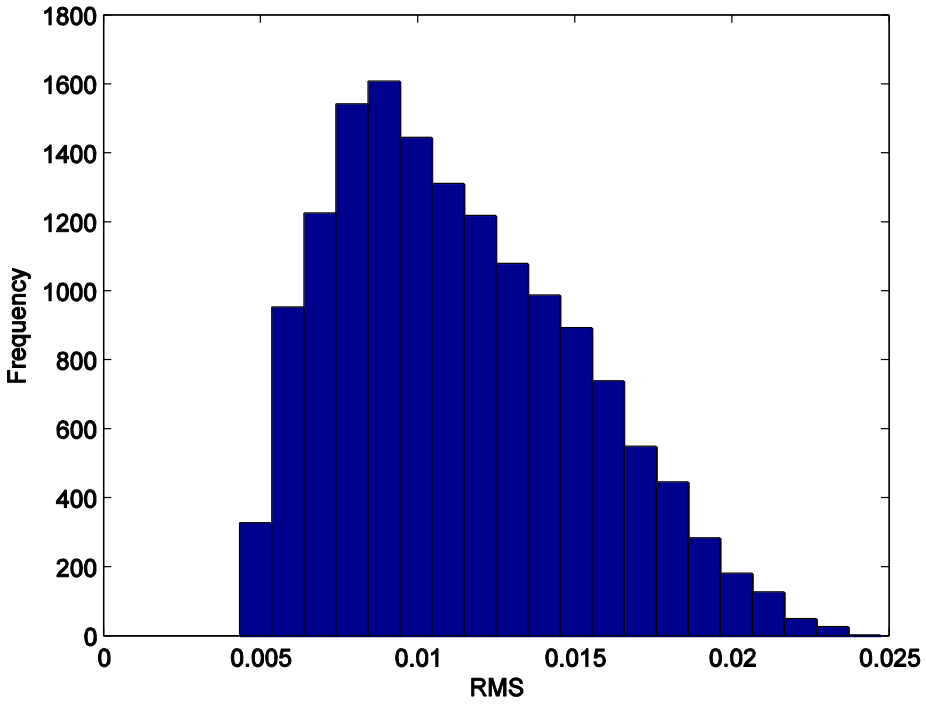

Figure 4.41: Histogram of RMS for 15000 times Monte Carlo simulations.

I chose the 2nd percentile of RMS, 0.005 in Figure 4.41, as the threshold, which I considered as an acceptable level of misfit. The ensemble of all acceptable models is plotted in the following figures, along with borehole SCPT data.

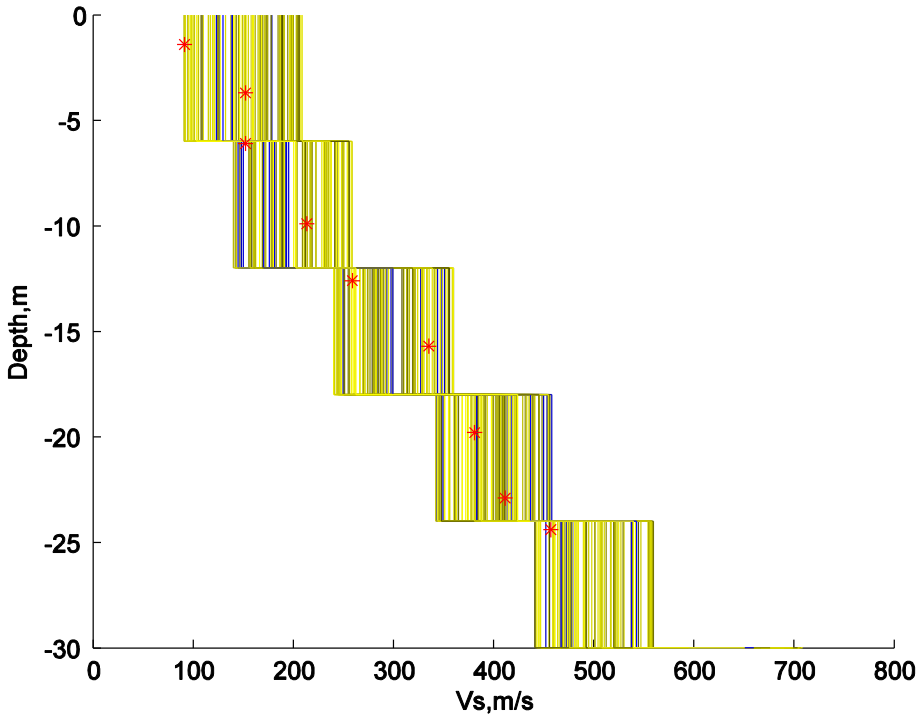

Figure 4.42: WFP site. Ensemble of all acceptable Vs models (RMS<0.005), line color from blue to yellow represent increasing RMS. Red stars are Borehole SCPT measurement of Vs.

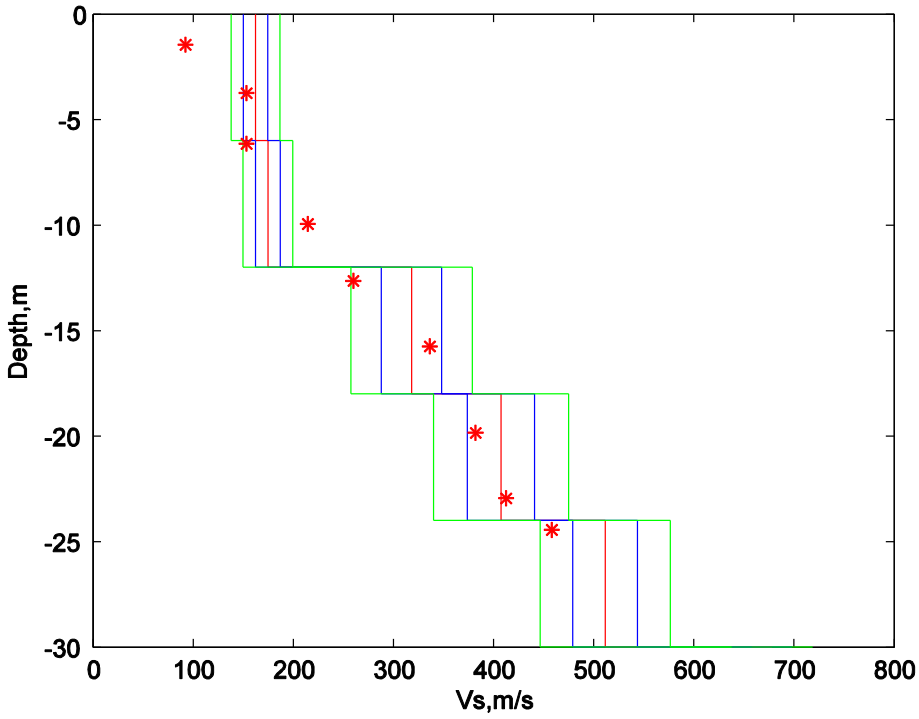

Figure 4.43: WFP site. Ensemble estimation of Vs model. Mean of the ensemble (red line), and 1-standard deviation from mean (blue line), 2-standard deviation from the mean (green line). Borehole SCPT measurements are Red star for comparison.

Mean Vs of the ensemble, along with 1-standard deviation, 2-standard deviation from the mean are calculated and plotted in Figure 4.43. Most of the SCPT fell within 2-standard deviation.

All forward calculated dispersions of the ensemble are given in the figure below, along with the observed dispersion data for comparison.

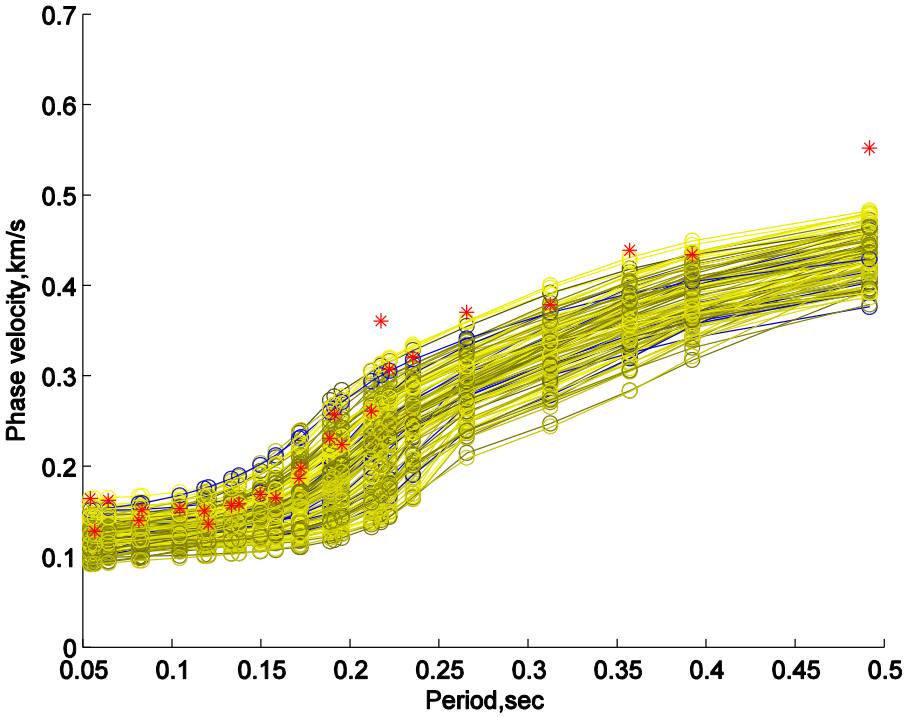

Figure 4.44: WFP site. Forward calculation of dispersion curves from the ensemble of all acceptable Vs models (RMS<0.005), line color from blue to yellow represent increasing RMS. Red stars: observed dispersion data from SPAC .

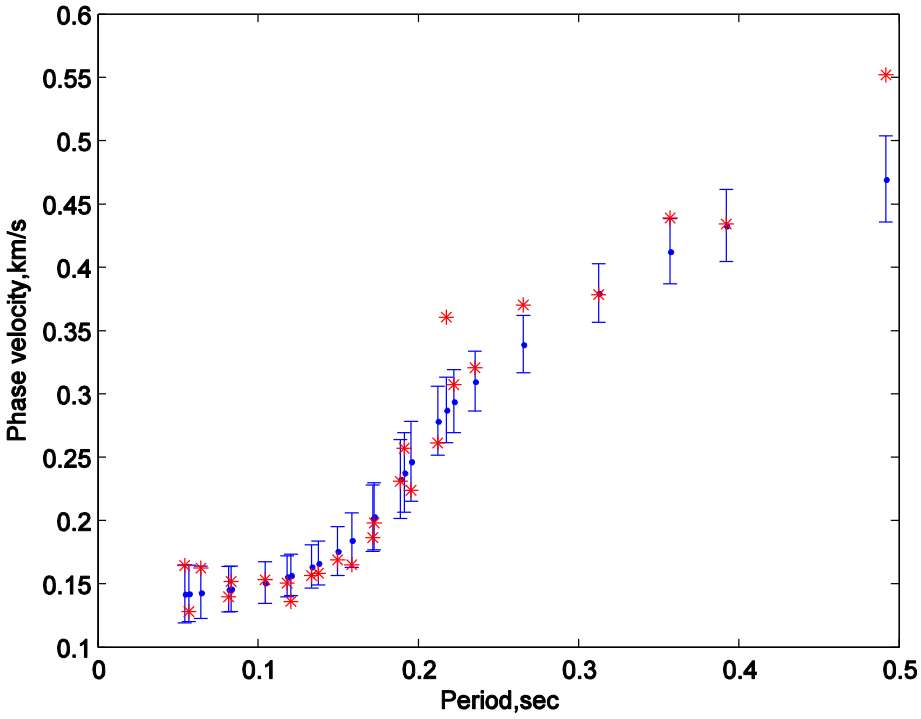

Figure 4.45: WFP site. Mean of the dispserion data (blue dot) from the ensemble, and error bar of 2-standard deviation (blue line), compared with observed dispersion from SPAC (red star).

The dispersion curves of the ensemble match the observed dispersion data quite well. 90% of the observed dispersion fall within 2-standard deviation range.

I forward calculated the dispersion curve using the mean, and 1, 2-standard deviation of the ensemble model (Figure 4.45 above), the results are show in Figure 4.46,

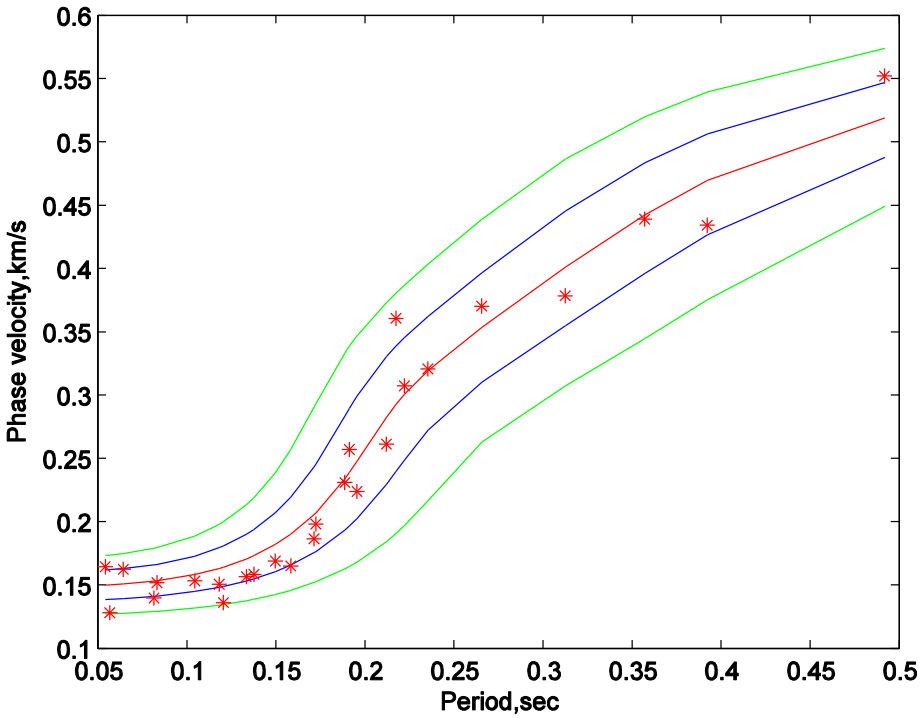

Figure 4.46: WFP site. Forward calculation of the dispersion from the mean (red line), 1-standard deviation (blue line) and 2-standard deviation (green line) based on estimation from the ensemble (models in figure 4.43 above). Red stars are observed dispersion.

Forward calculated dispersion curves using the mean, 1σ, 2σ of the ensemble fit into the observed dispersion data, and all observed data falls within 2σ, 93% fall into 1σ.

The statistical estimation of the ensemble of all acceptable models, i.e. mean, 1-standard deviation, 2-standard deviation, as show in figure 4.43, provides a reasonable description of the possible range of all plausible models, and they fit well with the observed dispersion data from SPAC, as well as the borehole SCPT measurements of Vs.

I applied the same methodology to two other sites, MBB and TRC. The ensemble estimates are given in figures below.

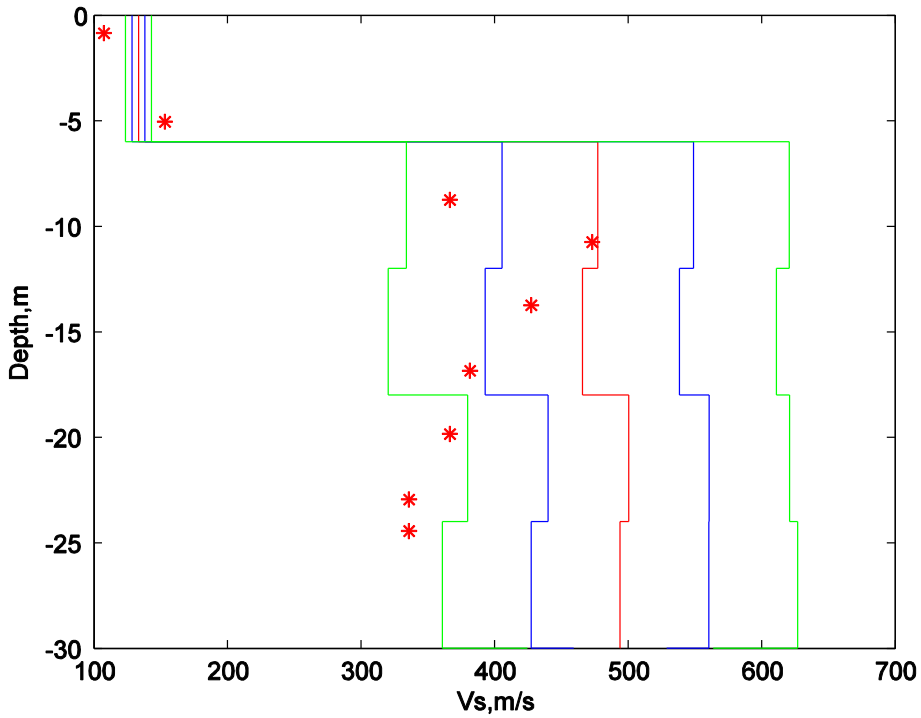

Figure 4.47: MBB site. Ensemble inference of the Vs model. Mean of the ensemble (red line), and 1-standard deviation from mean (blue line), 2-standard deviation from the mean (green line). Red star: Borehole SCPT measurements of Vs for comparison.

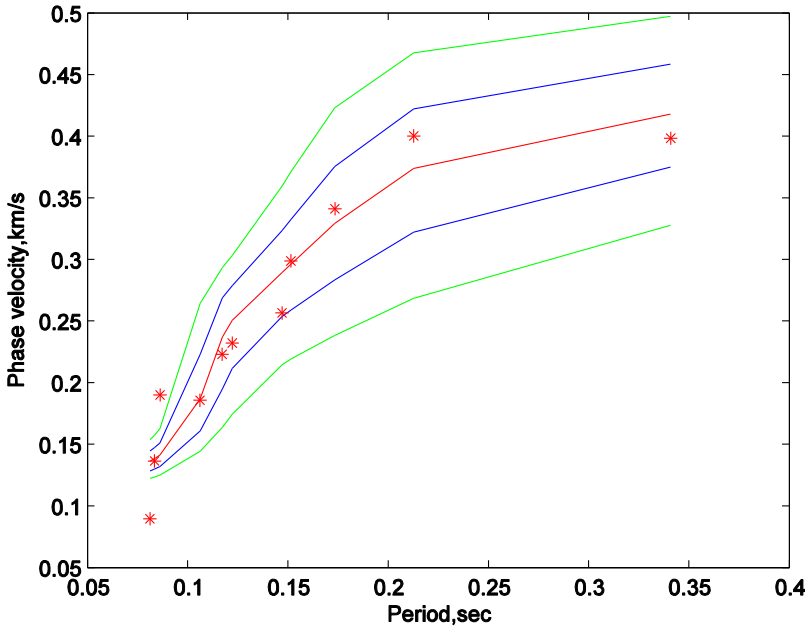

Figure 4.48: MBB site. Forward calculated dispersion from the mean (red line), 1-standard deviation (blue line) and 2-standard deviation (green line) based on estimation from the ensemble (models in figure 4.47). Red stars are observed dispersion data.

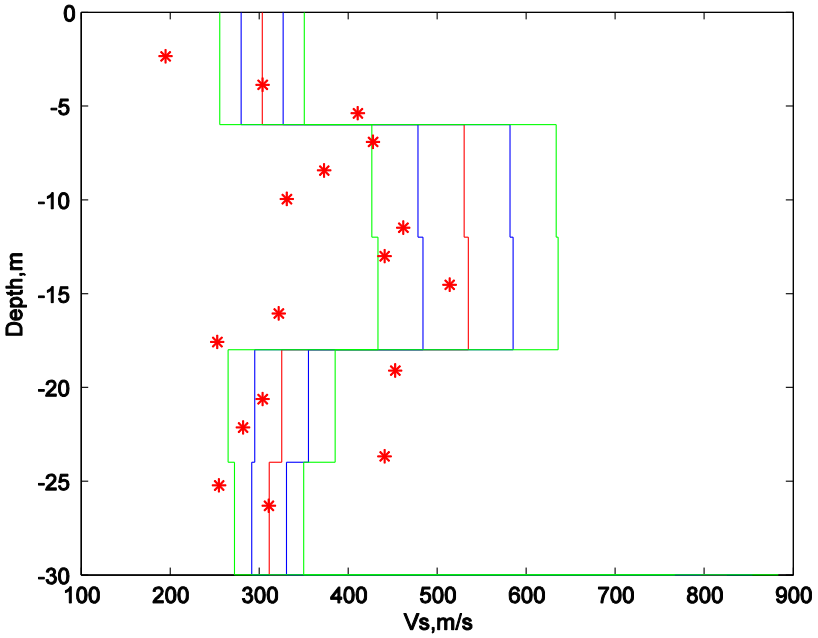

Figure 4.49: TRC site. Mean of the ensemble (red line), and 1-standard deviation from mean (blue line), 2-standard deviation from the mean (green line). Borehole SCPT measurements of Vs are Red star for comparison.

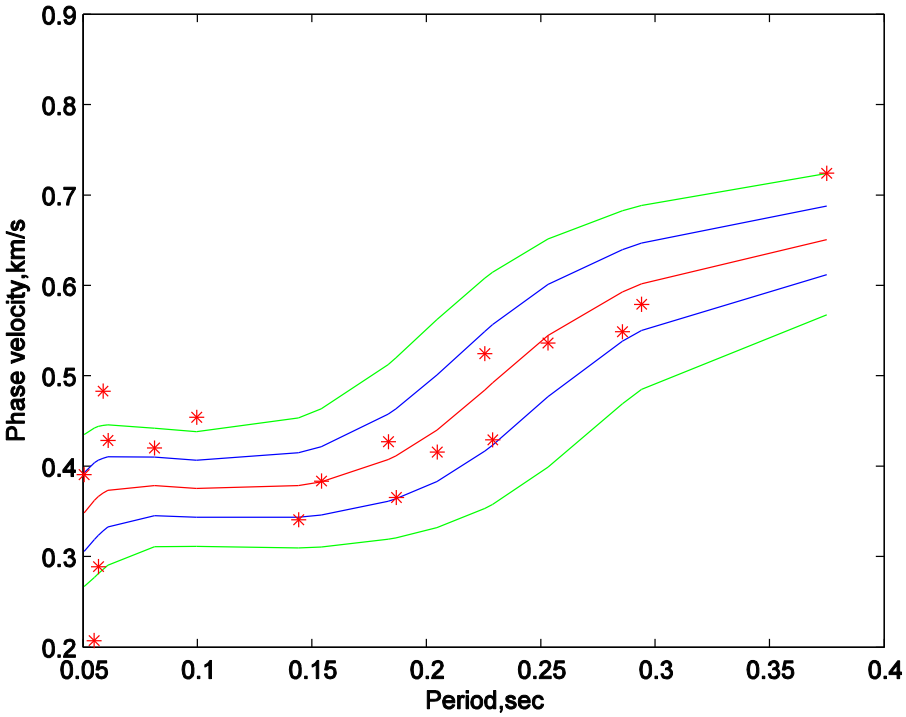

Figure 4.50 TRC site. Forward calculated dispersion curves from the mean (red line), 1-standard deviation (blue line) and 2-standard deviation (green line) from the based on estimation from the ensemble (model in figure 4.49 above). Red stars are observed dispersion.

Overall, the statistical estimate of the mean, 1σ, 2σ of the ensemble of all acceptable models characterizes the model space well. Both observed dispersion data and SCPT data are well described by the ensemble, especially for WFP and MBB site. For TRC site, both measured SCPT data and dispersion data are more scattered than WFP and MBB site. The scattering in SCPT is primarily due to the denser sampling of the borehole measurement. Since the SCPT measurement is discrete data points, denser sampling would inevitably cause more scattering in extremely heterogeneous crust, especially when abnormal velocity structures are presented like those in TRC site, including velocity jump at 5m and low velocity zone at around 20-30m depth (Figure 4.49). Instead

of smoothly increasing phase velocity with periods, the dispersion curve will also include trough (period 0.1 – 0.2 seconds) to account for the low velocity zone. Since the observed dispersion data are obtained from zeros of the measured coherency, information in certain periods might be missing (0.1-0.15 seconds) and the dispersion data would become more scattered as well (Figure 4.50).

4.6 Conclusion

In this chapter, I discussed the geophysical inverse problem, particularly shear wave velocity inversion from dispersion curve. I applied different techniques to invert for Vs structure. I first used the linear inversion technique to solve the problem. I linearized the shear wave inverse problem and applied the iterative linear inversion to invert for Vs using the dispersion data obtained from SPAC method in Charleston, South Carolina. Combining with prior SCPT data, the joint inversion adds further constrain during the inversion process, and characterizes some irregular structures, including sharp velocity jump, low velocity zone, etc. Considering that the problem is nonlinear in nature and the linear inversion depends on the initial guess and calculation of partial derivative matrix too much, I then developed two nonlinear inversion techniques, Monte Carlo and Simulated Annealing, and applied them to Vs inversion. Both techniques are random search algorithms, thus do not require particular initial guess or the computation of partial derivatives. The inversion results using Monte Carlo and Simulated Annealing algorithms are encouraging. The drawback of these two methods is that large amount of samplings of the model space is usually required and the simulation can be time consuming. The

nonuniqueness of the geophysical inverse problem leads to one problem, whether the "best fit" model obtained from both the linear and nonlinear techniques is the "true" Earth model we are seeking. Ensemble inference using stochastic inversion provides a better way to describe the solution of the inverse problem. Instead of trying to determine a single best fit model, I turned to look for the ensemble of all acceptable models and find the common properties shared by the ensemble. Through estimating the mean, variance of the ensemble, we could obtain a statistical description of the ensemble of all acceptable models. I applied the method to Charleston data to infer the characteristics of the ensemble. The results show that the mean, along with 1-standard, 2 standard deviation of the Vs estimation could describe the structure of model space well. Most of the observed dispersion data falls within forward calculated dispersion curve from the 2 standard deviation of the mean Vs estimation. The SCPT data also fit well into the ensemble. It shows that the ensemble inference method provides an innovative way to solve the geophysical inverse problem.

I compared all inversion techniques used in this chapter in the table below. It shows that the linear/constrained linear inversion depends on starting model and computation of partial derivative, but the amount of computation is small and the computation time is not long. For the random searching algorithms, Monte Carlo and Simulated Annealing could address the nonlinearity and nonuniqueness of the problem well. They have the advantage of not depending on starting model or computing the partial derivative. But the computation time can be long, because large amount of samplings are usually required. Constrained inversion is specially suitable for problems when there are prior information

regarding to the model and the estimation will not be deviated far from the constrain. Ensemble inference is the method that could give a statistical description of the model structure instead of a single model, which is particularly useful for nonunique problem when multiple models might fit the data well and the statistical properties of the ensemble are more appropriate to characterize the model space.

Technique / Property	Linear	Constrained Linear	Monte Carlo	Simulated Annealing	Ensemble inference
Starting model dependence	Yes	Yes	No	No	no
Computation of partial derivative	Yes	Yes	No	No	No
Amount of computation, number of iterations	Small	Small	Large	Large	Large
Prior information required	No	Yes	A Little	A Little	A Little
Able to address nonlinearity	Not good	Not good	Good	Good	Good
Able to address nonuniqueness	Not good	Not good	Good	Good	Good
Final result	Single best fit model	Single best fit model	Single best fit model	Single best fit model	Ensemble of acceptable models

Table 4.1: Comparison of different inversion strategies.

Reference

1. Aki and Richards, (2002), Quantitative Seismology (second ed.), University Science Books, Sausalito, CA
2. Aster, Richard, (2004). Parameter Estimation and Inverse Problems, Elsevier
3. Billings, S. D. (1994), Simulated annealing for earthquake location, Geophys. J. Int., **118**, 680–692.
4. Haskell, N. A., (1953), The dispersion of surface waves on multilayered media: Bulletin of the Seismological Society of America **43**, 17-34.
5. Kirkpatrick, S., C. D. Jr., and M. P., Vecchi, (1983), Optimization by simulated annealing, Science **220**, 671-680.
6. Levenberg, K., (1944), A method for the solution of certain nonlinear problems in least squares: Quarterly of Applied Mathematics **2**, 164-168.
7. Menke, W., (1989), Geophysical Data Analysis - Discrete Inverse Theory, Academic Press,New York.
8. Metropolis, N., A. Rosenbluth, M. Rosenbluth, A. Teller, and E. Teller, (1953), Equation of state calculations by fast computing machines: Journal of Chemical Physics **21**, 1087-1092.
9. Pullammanappallil, S. K., and J. N. Louie, (1993). Inversion of seismic reflection traveltimes using a nonlinear optimization scheme, Geophys., **58**(11), 1607–1620.
10. Pullammanappallil, S. K., and J. N. Louie, (1994). A generalized simulated-annealing optimization for inversion of first-arrival times, Bull. Seismol. Soc. Am., **84**(5), 1397–1409.
11. Press, F. (1968). Earth models obtained by Monte Carlo inversion, J. Geophys. Res. **73**, 5223-5234
12. Rothman, D. H., (1985). Nonlinear inversion statistical mechanics, and residual statics corrections, Geophysics, **50**, 2784–2796.
13. Rothman, D. H., (1986). Automatic estimation of large residual statics corrections, Geophysics, **51**, 332–346.
14. Sambridge, M., and K. Mosegaard, (2002). Monte Carlo Methods in Geophysical Inverse Problems, Rev. Geophys, **40**(3), 1009, doi:10.1029/2000RG00089.
15. Sen M. & Stoffa, P. L.,(1995). Global Optimization Methods in Geophysical Inversion, Advances in Exploration Geophysics Vol. 4, Elsevier, Amsterdam

16. Snieder, R., and J. Trampert, (1999). Inverse problems in geophysics, in Wavefield inversion, edited by A. Wirgin, pp. 119-190, Springer Verlag, New York,.
17. Thomson, W. T. (1950), Transmission of elastic waves through a stratified solid medium: Journal of applied Physics **21**, 89-93.
18. Tarantola, A., (2005), Inverse Problem Theory and Methods for Model Parameter estimation, Society of Industrial and Applied Mathematics, Philadelphia
19. Xia, J., R. D. Miller, and C. B. Park, (1999). Estimation of near-surface S-wave velocity by inversion of Rayleigh waves: Geophysics **64**, 691–700
20. Vasco, D. W., L. R. Johnson, and E. L. Majer, (1993). Ensemble inference in geophysical inverse problems, Geophys. J. Int.,**117**, 711–728.
21. Velis, D. R., and T. J. Ulrych, (1996). Simulated annealing two-point ray tracing, Geophys. Res. Lett., **32**(2), 201–204.

Chapter 5. Conclusion.

In this thesis, I used different advanced analysis techniques to process and analyze complicated seismic waveform in order to better characterize the Earth structure. Subduction structure in the Calabria Arc is well investigated using body wave signal. And the shallow structures in Charleston, South Carolina and Manhattan, New York City are studied by SPAC analysis of microtremor data. I also developed advanced inversion algorithms to invert for shear wave velocity structure from surface wave phase velocity dispersion curve.

In chapter 2, I first used natural earthquake generated seismic signals to study the complex subduction in the Calabria Arc, southern Italy. I analyzed the body wave signals that traversed the mantle under the Tyrrhenian Sea to investigate the slab effects on seismic waves. Dispersion analysis, scattering analysis, and attenuation analysis all indicated that the slab affects seismic wave in a consistent way. The low velocity slab causes P-waves to disperse when waves traveling through the slab. And the heterogeneous structure of the subducted lithosphere is the reason to explain the scattering of body wave traveling within it. Hot mantle materials above the slab results in the P-waves attenuate more than that go through the cold slab. I, therefore, separate ray-paths according to whether they went through the slab or not. The surface projection of the separating line indicates the location of the slab boundary in 2D. The combined analysis provided a better knowledge of the 3D structure of the subduction under the southern Tyrrhenian Sea. In order to gain deeper insight on the upper mantle structure of

the Calabria Arc, more data sets are needed for these types of analysis. Accurate ray tracing and waveform modeling, combined with tomography study, could also provide a more detailed 3D picture of the current slab morphology.

In Chapter 3, I analyzed microtremor data recorded by portable seismometers in Charleston, South Carolina and Manhattan, New York City to characterize the shallow subsurface structure. I used Aki's SPAC methodology to infer the shear wave velocity structure by analyzing microtremor signals. SPAC has the advantage of being easy to deploy in urban areas, not requiring active source and being a type of noninvasive experiment. Assuming the 2D wavefield recorded by an array of stations is stochastic and stationary ambient vibration, SPAC method calculates the fundamental mode Rayleigh wave phase velocity dispersion curve by spatially averaging the coherency of the microtremor recorded by the array. Three major steps for SPAC include, (1) Spatial coherency function between station pairs of fixed distance and different azimuth are computed. (2) Azimuthal average of the coherency is used to obtain phase velocity dispersion curve. (3) Phase velocity dispersion curve is inverted for Shear-wave velocity structure. The estimated Vs structures of Charleston correlate well with Vs from borehole and previous Refraction microtremor method. Also, the estimated depths of bedrock in Manhattan using SPAC are consistent with previous geological information. The SPAC method proves to be effective for subsurface Vs structure estimation in urban areas.

One critical step in SPAC for Vs estimation is inverting for the Vs from surface wave phase velocity dispersion curve. In chapter 4, I developed different inversion techniques to obtain the Vs from surface wave dispersion data. The inversion techniques I have used include iterative linear least square inversion, constrained inversion using borehole data as constrain, and Monte Carlo, Simulated Annealing algorithm. The inverted Vs well characterized the subsurface Vs structure with sharp velocity boundary and low velocity zone. The ensemble inference provides an innovative way to describe the model space. Instead of looking for the best fit model, I tried to infer the statistical properties shared by the ensemble of all acceptable models. The mean, along with the 1-standard deviation, 2-standard deviation of the ensemble prove to be useful in describing the structure of model ensembles. I compared advantages and the disadvantages of all inversion techniques used at the last of the chapter. Monte Carlo type random searching algorithms are suitable for nonlinear, nonunique problems, but they are usually computational intensive. Linear/constrained linear inversion do depend on initial guess of the starting model, and require the computation of partial derivative, but the amount of computation is less than Monte Carlo and Simulated Annealing method. Hybrid inversion strategy combining different methods that make best use of each method's merit could be a better way for solving complicated geophysical inverse problems.